A Molecular Dynamics Study of Diamond as a Plasma Facing Material for Fusion

Alastair Dunn

University College London

Department of Physics and Astronomy

A Thesis submitted for the degree of Doctor of Philosophy
in Theoretical Physics

Submitted November 2010
Accepted January 2011

I, Alastair Dunn confirm that the work presented in this thesis is my own. Where information has been derived from other sources, I confirm that this has been indicated in the thesis.

Alastair Dunn
January 24, 2011

Acknowledgements

I would like to thank my supervisors Dorothy Duffy and Marshall Stoneham. I am indebted to them for their guidance and support throughout the course of this PhD and during the writing of this thesis.

I am also grateful to Alex Rutherford and Sascha Khakshouri for their patient assistance, especially during the early stages of this research. There are many other colleagues and friends who have supported me over the last few years and who have made completing this PhD a memorable experience and a pleasure. I would especially like to thank Alex Grimwood, Maria del Mar Rodriguez Yebra, Matthew Shiers, Hemant Tailor and Matthew Wolf.

Finally I would like to thank my family for their constant support and encouragement. I especially owe my deepest gratitude to both my mother and brother, to whom I would like to jointly dedicate this thesis.

Abstract

Fusion power offers a promising source of clean energy for the future, however, one of the greatest challenges in tokamak reactor design is developing materials suitable to withstand the intense plasma-material interactions. Carbon, mostly in its graphitic form, is currently a favorite plasma facing material in many reactors. Diamond, however, offers many advantages over other materials but is not widely accepted. Although diamond exhibits excellent structural and thermal properties, tritium retention is a major concern for carbon. However, recent experimental evidence suggests that diamond might fare better than other carbon structures as a plasma facing material.

This thesis investigates the the cumulative effect of exposing diamond to high thermal shock and tritium bombardment using classical molecular dynamics simulations. Of interest is diamond's resistance to graphitisation and the mechanisms behind tritium retention.

Surfaces of different lattice orientation and level of hydrogen termination were incrementally heated to temperatures in excess of 2000 K. Generally, these diamond structures appeared to be stable up to temperatures of about 1000 K. Orientation did play a large part in determining the temperature of phase change, as did the level of hydrogen termination. Greater hydrogen coverages mimicked bulk continuation and increased resistance to graphitisation.

These diamond surfaces, as well as a graphite and a diamond grain-boundary surface, were bombarded at a range of temperatures (300-2100 K) with high fluxes (10^{29} $m^{-2}s^{-1}$) of 15 eV tritium atoms in studying relative tritium retention at and below the surface as well as sputtered hydrocarbon yields. Below temperatures of graphitisation the diamond structure confined tritium, and thus further structural damage, to the upper surface. The graphitic surface allowed for deeper tritium penetration and retention. The presence of a grain boundary in the diamond slab allowed small amounts of tritium to penetrate deep into the bulk.

Diamond surfaces were also bombarded at 300 K whilst independently varying incident ion energy (7.5-30 eV) and incident interval time (0.3-1.2 ps). Greater ion energies caused proportionally greater damage as well as reducing the ability of the structure to disperse incident thermal energy. At these extremely high fluxes sputter yield appeared to not vary with flux but was found to be proportional to fluence.

Contents

1 Introduction **3**

2 Reactor Design **7**
2.1 ITER . . . 7
2.2 Candidate Plasma-Facing Materials . . . 11

3 Carbon as a Plasma Facing Material **13**
3.1 Crystalline Structure . . . 13
3.2 Graphitisation . . . 14
3.2.1 Surface Graphitisation . . . 15
3.2.2 Bulk Graphitisation . . . 16
3.3 Sputtering . . . 18
3.3.1 Chemical Sputtering . . . 19
3.3.2 Physical Sputtering . . . 23
3.4 Tritium Retention . . . 25
3.4.1 Hydrogen Trapping and Release . . . 25
3.4.2 Co-deposition . . . 26
3.5 Diamond Exposed to Plasmas . . . 26

4 Modelling **29**
4.1 Molecular Dynamics Setup . . . 30
4.1.1 Integration Algorithm . . . 31
4.1.2 Thermostat . . . 31
4.1.3 Periodic Boundary Conditions . . . 35
4.1.4 Potential . . . 36
4.2 The AIREBO Potential . . . 38
4.3 DL_POLY run with AIREBO potential . . . 44
4.3.1 Subroutine Pseudo Code . . . 53

5 Thermally Induced Graphitisation **58**
5.1 Method . . . 58
5.2 Surface Structure . . . 60
5.3 Heating . . . 64
5.4 Chapter Summary . . . 79

6 Diamond Tritium Bombardment **83**
6.1 Method . . . 83
6.2 Structural Damage . . . 86
6.3 Tritium Retention . . . 94
6.4 Sputtering . . . 99
6.5 Diamond Etching Mechanism . . . 103
6.6 Chapter Summary . . . 104

7 Graphite Tritium Bombardment **106**
7.1 Method . . . 106
7.2 Carbon Sputter and Tritium Retention . . . 107
7.3 Chapter Summary . . . 111

8 Flux & Ion Energy Dependence **113**
8.1 Method . . . 113
8.2 Incident Flux . . . 115
8.3 Incident Ion Energy . . . 121
8.4 Loss of Thermal Conduction with Damage . . . 128
8.5 Chapter Summary . . . 129

9 Diamond Grain Boundary Tritium Bombardment **131**
9.1 Method . . . 131
9.2 Tritium Retention . . . 133
9.3 Chapter Summary . . . 137

10 Summary **139**

11 Appendix **143**

1 Introduction

One of today's most pressing scientific, political and social issues is that of 'clean energy'. That is, the generation of energy whilst having minimal effect on our environment. Power derived from fossil fuels, such as coal, oil and natural gas, generate as a by-product copious amounts of greenhouse gases which have been linked to irreparable and accelerating global climate change. Access to these fuels is also limited by their finite natural distribution and by political and economical factors. There exists the challenge to find ethical and cost-effective power sources to meet our ever growing energy needs. One proposal is nuclear power.

Globally, nuclear power has been extensively harnessed via the process of nuclear fission since its commercial advent in the early 1950's. With sufficient regulatory controls and safe waste-disposal fission poses little negative impact on the environment. However, the potential of nuclear fusion promises even more. Not only is the energy yield considerably higher when considering volume of fuel input, but the raw materials for the fuel are naturally abundant or easily derived, there is comparatively very little radioactive waste produced and no greenhouse gas production.

Soon after Einstein presented what is probably now the most widely and popularly known equation, $E = mc^2$, in his Special Theory of Relativity, the idea of manipulating matter into energy has played a prominent part in the worlds of science and politics.

Although it was to be nuclear fission that would later take centre-stage, the secrets to nuclear fusion were sought-after first - a process so promisingly powerful it was theorised to be what drove the stars. For example, recognising this potential, Russian Soviet authorities offered the Physicist and Cosmologist George Gamow the nightly use of Leningrads electrical power grid to setup a fusion research laboratory [1], although with the advent of nuclear fission in 1939 the development of fusion power took a back seat. However, with sufficient developments in plasma physics and growing energy requirements, interest in the field has again grown.

Nuclear fusion in a power plant would take advantage of the energy released due to the net mass difference between the products and ingredients in a deuterium/tritium reaction, with the majority of the released energy being carried off kinetically by a produced neutron as detailed in Equation (1). Deuterium is a naturally occurring hydrogen isotope found in sea water (about one part in 6000), and tritium may be bred via nuclear decay, for example within the reactor itself through

neutron bombardment and the subsequent decay of lithium.

$$ {}^{2}_{1}\mathrm{D} + {}^{3}_{1}\mathrm{T} \longrightarrow {}^{4}_{2}\mathrm{He}(3.5\mathrm{MeV}) + {}^{1}_{0}\mathrm{n}(14.1\mathrm{MeV}) \quad (1) $$

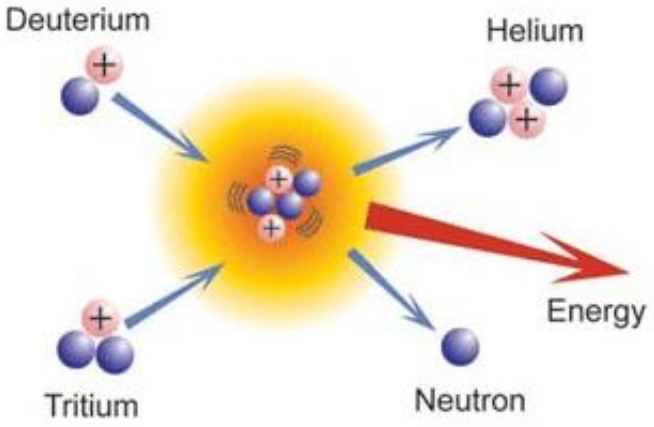

Figure 1: Deuterium-tritium fusion reaction [2].

In order to induce two nuclei to overcome their Coulombic repulsion to each other, high-temperature plasmas are required, a state of matter where the pressure and temperature is so high that atoms are completely ionised. Two dominant promising design proposals to recreate this extreme environment have developed. Inertial-confinement fusion (ICF) involves the bombardment of small, solid deuterium-tritium (DT) pellets with high intensity infra-red lasers causing the pellet surface to rapidly expand and increase pressure at the pellet core. This rapid implosion increases internal density and for about one-billionth of a second temperatures rise above ten million Kelvin where fusion occurs. The second approach is to magnetically confine the fuel. Current reactors favour the Russian tokamak design which magnetically compresses the fuel within a toroidal configuration of magnets.

In both designs the high-energy neutrons carry away most of the energy released in the process. This energy is then transfered to a coolant which in turn drives conventional turbines generating electrical power.

Insulating this high-temperature stellar process from the surrounding terrestrial environment (a temperature difference of order of magnitude 10^6 K) is achieved though a combination of vacuums, electro-magnetic containment, limited plasma-surface interaction and effective plasma-facing shielding. Intense fluxes of high-energy neutrons pose serious engineering problems since they will not be magnetically deflected and will irradiate and potentially damage the confining torus. In

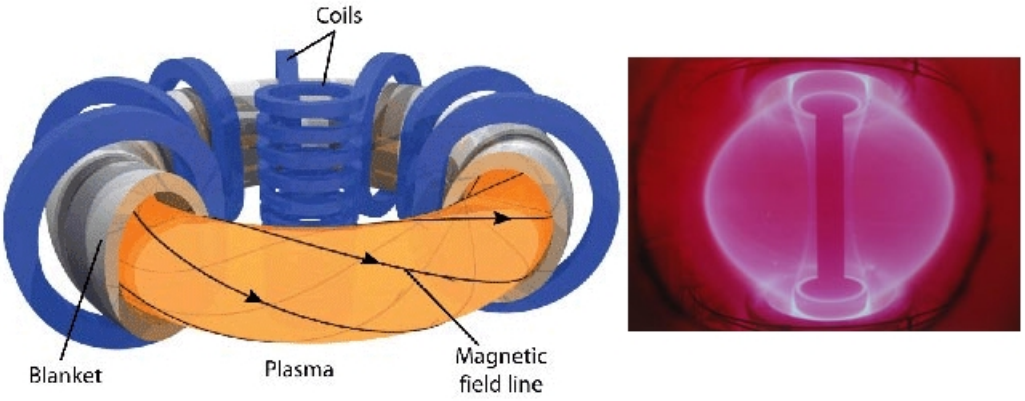

Figure 2: Left: A tokamak - General layout of super-conducting magnetic containment chamber and magnetic field confining the plasma [2] . Right: View of the plasma inside the MAST tokamak in the United Kingdom during operation. Culham http://fusion.org.uk/ .

addition to radiation damage, plasma-material interactions will result in chemical and physical sputtering as well as large thermal shocks. In the 'next-step fusion device', it is expected that plasma-facing material (PFM) could endure up to a centimetre of erosion [3]. The plasma-facing materials challenge of future fusion power plants centres on surviving ion-bombardment and thermal damage without contaminating the confined plasma.

This thesis is loosely structured into three parts: introduction, method and results. Chapters 2 and 3 introduce the tokamak reactor design and diamond as a plasma facing material. Chapter 4 then outlines the modifications made to the package DL_POLY_3 and how molecular dynamics simulations were employed in this study. Chapters 5 and onward present the results of this work investigating different, yet connected, phenomena. These results chapters are further broken down into specific methods and results subsections.

Chapter 5 looks at the graphitisation of diamond and the effects surface topography has on it. The following chapters all centre on the cumulative bombardment of surfaces with tritium (varying either substrate temperature, bombarding ion energy or incident flux) and focus on the resulting structural damage and tritium retention levels.

In Chapters 6 and 7 diamond and graphite surfaces are bombarded with 15 eV tritium at a fixed flux and over a range of substrate temperatures (300-2100 K).

In Chapter 8 diamond is again bombarded but the substrate temperature is kept fixed at 300 K whilst independently varying incident ion energy (7.5-30 eV) and flux (bombarding interval times 0.3-1.2 ps).

In Chapter 9 a diamond grain boundary is bombarded at a fixed flux and incident energy over a range of substrate temperatures.

2 Reactor Design

The 'next step' towards a fully functioning and economically viable commercial fusion reactor is ITER, originally the *International Thermonuclear Experimental Reactor*, Figure 2 (the acronym also appropriately means journey or way in Latin). The principal aim of this project is to demonstrate the scientific and technological viability of fusion energy and it is projected to be operational before 2020. Located in Cadarache, France, it is expected to cost its participants approximately US$10 billion. Those parties involved are the European Union (represented by EURATOM), Japan, the People's Republic of China, India, the Republic of Korea, the Russian Federation and the USA. Whereas previous fusion reactors TFTR (tokamak Fusion Test Reactor) and JET (Joint European Torus) have sustained power outputs of 10.7 MW and 16 MW respectively for less than a second, ITER is expected to produce 500 MW for 1000 seconds by heating 0.5 g of Deuterium/Tritium to a temperature of 100 million K[1]. Later commercial reactors, functioning as power plants, will have to generate about 1 GW of power for prolonged periods. It is also hoped that with ITER, the heat produced by the fusion reaction will self-sustain a continued reaction thus economising on input energy requirements.

The enterprise is also intended to pool international research and development in the fusion energy field and to give a platform to further experimental research, one field of which is the development of protective plasma-facing materials. There are many demands and restrictions on a plasma facing material. For example, if the surface is ablated or fragmented to spall and create dust, contamination of the plasma itself might occur whilst leaving the PFM damaged and mechanically inadequate. Exposure to intense temperatures demands materials with high thermal conductivity.

2.1 ITER

Within the tokamak design, plasma-facing materials form the protective tiling on the inside of a blanket around the main chamber and around the divertor plates. This blanket around the reactor core has three main functions; to generate (or breed) fuel tritium, to absorb and transfer energy from the high-energy neutron radiation and to shield the rest of the structure from damage. The reference design for armour at the divertor region for ITER currently uses a combination of carbon-based materials and tungsten, while the reference PFM of the main chamber is beryllium. However,

[1] http://www.iter.org/a/index_nav_4.htm

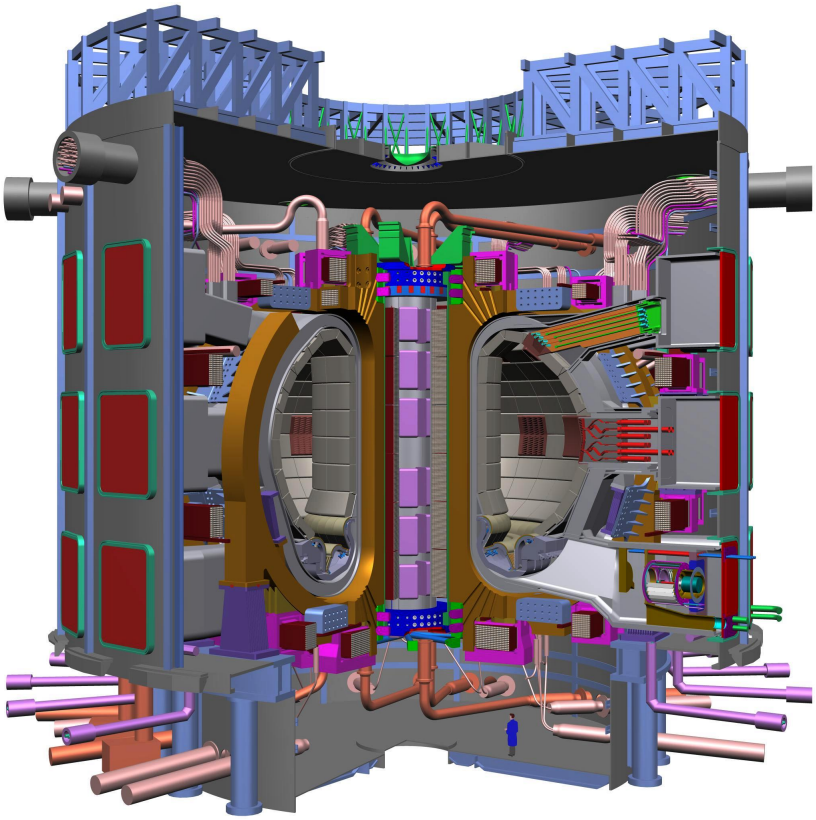

Figure 3: The ITER tokamak cutaway showing reactor relative in size to the average person (standing beneath righthand opening of main chamber) [4]

for a possible follow-up reactor (DEMO), which will aim at replicating something closer to a commercial power station's energy output (about 1 GW), the possibility of using only carbon PFMs has been suggested [5].

Figure 4 shows the location of the main chamber components in the ITER reference design in relation to the open magnetic flux surfaces, which manipulate the plasma. Not shown in Figure 4 are the surfaces which confine the plasma ions and close back on themselves forming 'closed-loops'. This region is called the plasma core and is where nearly all nuclear energy is generated. The outer surface of the core is referred to as the edge region, and is immediately inside the last closed flux surface - the separatrix. The edge region contains not fully ionised impurities which can radiate energy to the chamber wall (and are thus visible - see image of plasma within MAST shown Figure **??**), and undesirably cool the plasma. The separatrix is the first flux surface depicted in Figures 4 and 5, and is uniquely characterised by an intersection in the poloidal magnetic field known as the X-point. Beyond this, the outer region consists of flux-surfaces that intersect wall material in the divertor area. This outer region is known as the scrape-off layer (SOL), because power is rapidly

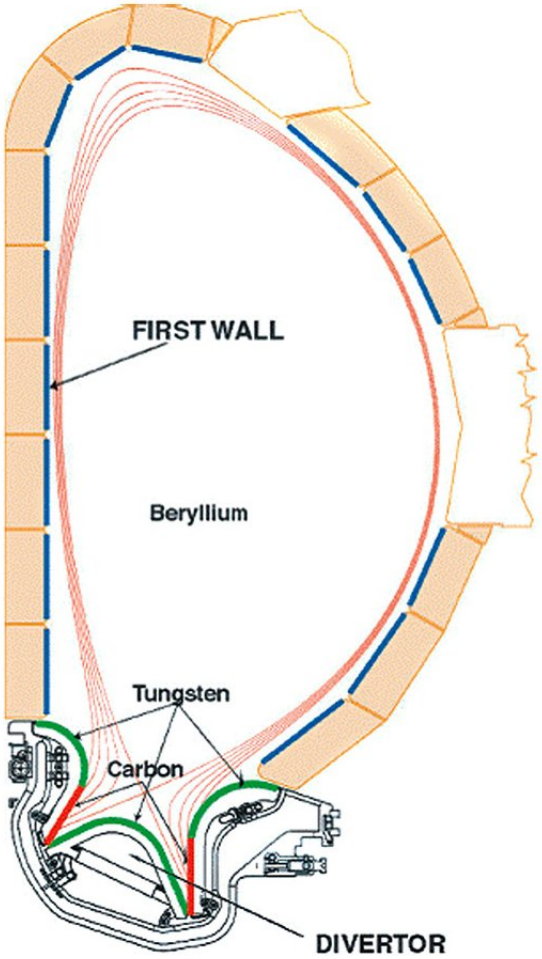

Figure 4: Cross-section of plasma-facing materials in the ITER reference design. The divertor plates are shown in red and will initially be made of carbon. The upper baffles and the dome will be made of tungsten (shown in green) and the first wall will be made of beryllium (shown in Blue). Cross-sections of the open magnetic flux surfaces are show as light red lines (closed surfaces at the centre of the chamber are not shown) [6].

scraped-off, and it is thinnest at the midplane in the main chamber and thickest near the X-point. In the vicinity of the divertor plasma the SOL expands by a factor of approximately four. This reduction in density, coupled with intentionally injected impurities, results in a highly radiative (favourably cooling) plasma in the divertor region.

The function of the divertor is to pump away waste helium, to control and contain plasma impurities and generally to take the brunt of the necessary plasma-material interactions (PMIs). This last requirement is obviously preferable in an area away

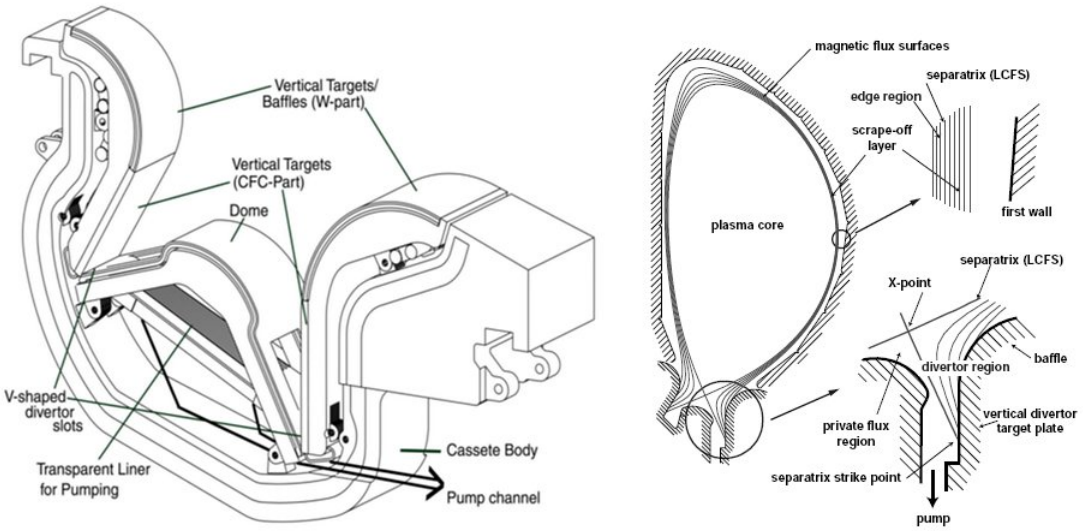

Figure 5: Left: Divertor cassette showing the large openings in the dome support [7]. Right: Poloidal cross-section of a tokamak plasma labeling the different plasma regions [3].

from the core-plasma, thus reducing the chances of contamination. However, near divertor plates, plasma temperature is comparatively low and often incident ions are below the physical sputtering threshold of higher Z materials. The vertical target plates will intercept the magnetic field lines of the SOL and form a 'V' shape with neutral particle reflector plates which confine neutral hydrogenic particles to the divertor channels.

Plasma facing materials will be selected for a range of desired properties. Different areas within the tokamak will emphasise specific requirements and so compromises will have to be made in catering for all. For example, PMIs will vary drastically at different areas of the reactor with ion energies of 500 eV at the midplane and upper baffle and 15 eV in the vicinity of a detached divertor [3], where 15 eV is below the physical sputtering threshold of many materials. Because of this, exploiting various strengths in the use of composite structures is an attractive option [5]. Generally, a lower Z material reduces the radiative effects of plasma contamination at the plasma/wall interface, but a higher Z material is more resilient to sputtering.

2.2 Candidate Plasma-Facing Materials

Beryllium (Z=4)

Being a low Z metal, beryllium is readily ionised when an impurity within the plasma-core and thus does not radiate large amounts of energy. This said, it does suffer from high physical sputtering levels and has a relatively low melting temperature of about 1560 K and high thermal expansion factor of 11.3 μm.m^{-1}K^{-1}. Thermal conductivity at 300 K is reported to be 200 W/(m.K). However, since it is not very reactive with hydrogenic isotopes it causes little concern regarding tritium retention and is resistant to high thermal shock loads. The use of small surface-area tiles would reduce the effects of low-temperature embrittlement due to exposure to neutron radiation and incident radiation may be utilised in generating tritium through transmutation via lithium. This nuclear decay is referred to as 'breeding' and makes beryllium useful as a first wall material of the main chamber.

Tungsten (Z=74)

Tungsten has been proposed for the divertor baffle areas where there will be a high flux of neutral particles and charge exchange atoms of energies ranging from 100 eV to several keV. This bombardment can cause physical sputtering and for this reason the high Z of tungsten is a significant advantage over other materials. Due to its lower ionisation potential, sputtered material will accelerate away at lower velocities and may be quickly redeposited back on the divertor surface. Because of this it has a lower erosion rate than Be and C. Although tungsten suffers low tritium retention, experiment has shown tungsten surfaces above 1000 K to develop a surface 'fuzz' on exposure to plasmas [8, 9], which could then be a source of high-Z dust and contaminate the plasma. Being a high Z material, tungsten would have a greater cooling effect on the plasma as a contaminant than carbon for beryllium. Tungsten has a melting temperature of 3695 K with a thermal conductivity of about 173 W/(m.K) and thermal expansion of 4.5 μm.m^{-1}K^{-1} at 300 K.

Carbon (Z=6)

Carbon is currently the dominant material in the world's tokamaks and it is the historical choice for plasma facing materials [3] due to its excellent thermal properties and the fact that carbon impurities lead to minimal radiation within the plasma.

Of all candidates for PFM, carbon-based materials, although they do have serious drawbacks, are generally the superior choice. This is specifically due to the

properties associated with diamond and diamond-like structures. Even graphite, which is already widely used, in the basal plane shares diamond's characteristics of low thermal expansion coefficients and high thermal conductivity. As mentioned, tritium retention is a major drawback for all carbon materials. Due to the high reactivity of carbon with hydrogen and its isotopes, incident ions may bond with the surface creating a tritium rich surface layer. In addition to this, sputtered hydrocarbon material may recombine with the wall. Not only does this enhance the tritium count at the wall directly, it can encourage the development of a 'soft' amorphous hydro-carbon layer which may be prone to enhanced tritium retention.

Although graphite does not readily melt, rather undergoing surface sublimation, it does suffer from dust production when fatigued which leads to carbon and hydrocarbons re-depositing on the surface (potentially increasing the tritium inventory) or condensing within the plasma and thus contaminating it.

3 Carbon as a Plasma Facing Material

Although diamond and graphite are strong candidate materials, carbon-fibre composites (CFCs), amorphous hydrocarbons (a-C:H) or 'diamond-like' carbon (DLC) surfaces offer a spectrum of tailored properties exploiting strength and flexibility, which may be suitable for use throughout a tokamak chamber. CFCs are the reference material in ITER at the lower part of the divertor region due to their superior thermal properties over Be or W. In this area they are expected to experience neutron damage at a maximum of 0.1 dpa [10]. They are also resilient to excessive heat loads in the event of sudden loss of plasma confinement or when energetic particles rapidly escape from the edge region into the scrape-off layer - edge-localised modes. Current CFCs have been manufactured as carbon-armoured components that can endure a heat flux of over 20 MWm^{-2} [7]. By controlling the level of hydrogen saturation and the $\mathrm{sp}^2/\mathrm{sp}^3$ bond ratio when manufactured, these films can be tailored with varying visco-elastic properties and thus, to some extent, may be potentially self-healing under stress and irradiation.

The processes involved with incident ionic bombardment and subsequent erosions dominate PMIs. The release of wall material as a consequence is referred to as sputtering and leads to issues related to plasma contamination and redeposition back upon the plasma-facing material. Material can also evaporate due to electrical arcing.

By any mechanism, the contamination of the plasma can lead to dilution and unwanted radiation (cooling) due to impurities not being completely ionised. Impurities of low Z materials, such as carbon, are preferable since they are stripped of their electrons a lot easier and thus radiate less when within the plasma core.

Redeposition of sputtered material on the wall leads to difficulties in controlling fueling efficiency and limits PFM lifetimes. Redeposition of eroded material which has chemically combined with hydrogenic isotopes can lead to tritium retention and is a major concern since it increases the tritium inventory, which is limited due to safety concerns.

3.1 Crystalline Structure

The irradiation of realistic surfaces will mean considering variations on an ideal atomistically flat surface. Surface steps and large scale ripples as well as a varying degree of hydrogen-termination at the surface will affect tritium retention, sputtering yield and sputtered species produced. Various molecular dynamics (MD) investigations into the effects of atomistic surface steps on sputtering yield have

been performed. For example, a preference for sputtered material to originate from the periphery of a step was observed by Karolewski [11] for 3 keV Ar ions incident on a stepped Cu (100) surface. Naturally, yield is hugely dependent on the angle of ion incidence and interplays closely with surface step effects.

Irradiating a material will not only have direct consequences on that material's mechanical properties but can consequently alter the surface topography which might leave the material susceptible to further radiation damage. Specifically, surface vacancies and clusters can form steps and where bombarded atoms have not been imparted with quite enough energy to be completely ejected, comparatively loosely bonded adatoms can form on the surface, also altering surface topography.

Chemical vapor deposition techniques are used to 'grow' poly-crystalline diamond films. Crystal size may be varied depending on requirements. As the topography of a crystal surface will affect its performance, so will the presence of grain boundaries. For example erosion of material from carbon-fibre composite surfaces was found to mostly originate from in-between fibres [12] and at the edges of plane for graphitic samples [13]. Experiment has also shown nano-crystalline diamond surfaces to sputter more than micro-crystalline [14], suggesting that grain boundaries might also be a source of enhanced sputter.

3.2 Graphitisation

The thermodynamically driven transition of a carbon structure from a diamond (sp^3-bonded) matrix to that of a graphite (sp^2-bonded) configuration has been studied for many years. Nath [15] first proposed the mechanism of diamond's 'puckered' (111) planes separating from each other and flattening to form the hexagonal planes of a graphene sheet. Although graphite is the more energetically favourable of the two structures, there exists a large potential barrier separating their configuration energies. For this reason diamond is referred to as a metastable state. Overcoming this barrier by sample heating for micro-sized diamond powder was experimentally achieved by Seal in 1960 [16] at a transition temperature range of between 1900 K and 2300 K. Within this range a mixture of sp^2 and sp^3 bonding was observed. An apparently disordered mix of sp^2/sp^3 hybridisation is loosely known as amorphous carbon (a-C).

3.2.1 Surface Graphitisation

Variations in surface topographies will facilitate the graphitisation of diamond with varying readiness. Such features include 'steps', grain boundaries, dangling bonds and levels of hydrogen saturation. Understanding these mechanisms at the surface can lead to a deeper knowledge of those within the sample bulk.

De Vita *et al.* [17] performed first principles MD simulations on a diamond slab of 192 atoms, with one of the six (111) planes exposed as a (2x1) reconstructed surface. When heated to about 2500 K from initially close to 0 K, bonds between the first and second (111) diamond bilayers began to break and as a knock-on effect atoms in adjacent layers energetically favouring pi-bonds propagate the process of graphitisation. Once this occurred, fast graphitisation of the whole slab followed resulting in all the diamond (111) bilayers forming graphene sheets by 3000 K.

The sequence of sp^3 bond breaking and sp^2 bond formation within adjacent (111) bilayers has been studied by Los and Fasolino [18] using their own long range bond order potential for carbon (LCBOP - which involves both short-range and long-range components) in Monte Carlo simulations. The focus of their study was on the dependence of graphitisation on the surface topography (non-reconstructed and (2x1)-Pandey-reconstructed) of the (111) slabs and on the slab thickness. Simulations were performed using two different cutoff ranges; 2.2 Å and 2.3 Å. The effect of such a small difference in cutoff range had an observable effect on the reaction path of graphitisation. Full graphitisation of a non-reconstructed slab of 384 atoms and six bilayers took place over temperature ranges of 1300-1400 K and 1100-1200 K for the two cutoffs respectively. Here, as observed by De Vita [17] and Saada [19], the process of graphitisation was initiated at the surface by a few bonds breaking between the top two bilayers. Figure 6b shows how from this sp^2 nucleus, graphitisation propagates in a direction perpendicular to the surface.

It was observed that for slabs thicker than about six bilayers, the mechanism of graphitisation changes from perpendicular propagation from a surface nucleus to that of a layer-by-layer peel-away process. This is illustrated in Figure 7 where a 'thick' slab of 12 layers is compared to a sample with a fixed substrate, replicating bulk diamond. The process of graphitisation is similar for each. The first graphite layer formed at a temperature of about 2000 K, about 600 K higher than for the 'thin' slab. This dependence on thickness is attributed to the relationship between the nature of bond forming-breaking behaviour and the local chemical environment, something modelled in empirical potentials as a dependence on variables such as bond angles and the local coordination of first and even second nearest neighbours.

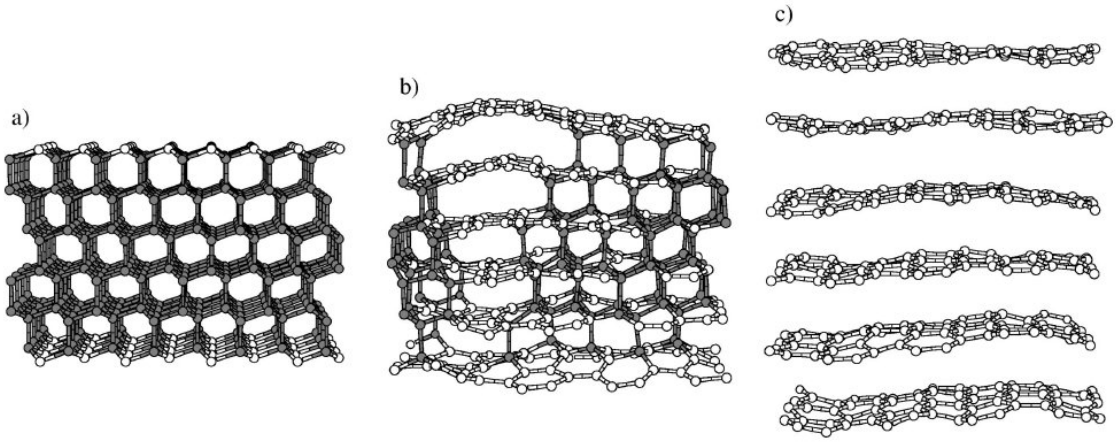

Figure 6: Snapshots during an (NPT) Monte Carlo annealing simulation of a 'thin' diamond (111)-slab containing 384 atoms from *a)* 0 K, initial configuration, to *b)* and *c)* at 1400 K. White and gray spheres are atoms with coordination three and four respectively [18].

For the (2x1)-Pandey-reconstructed slabs, graphitisation occurred at higher temeratures, highlighting the dependency on surface topography. For the first cut-off range of 2.2 Å, phase transition temperatures for thin and thick slabs were found to be ≈2500 K and ≈2750 K respectively.

3.2.2 Bulk Graphitisation

A surface, and thus a disruption to the regular crystal structure, will be less energetically favorable than a continuous bulk and so graphitisation will more readily occur on heating. However, given enough energy, the bulk itself may undergo graphitisation. Any defects to the crystal will inevitably alter its stability. For example, high energy fusion neutrons can impart kinetic energy creating a cascade and localized melting. Marks [20] reports that this rearrangement of atoms dominantly occurs while the temperature of the initial thermal spike (the initial 0.2 ps of the cascade) lies in the range of 3000 K to 5000 K. This region quickly quenches after the heat dissipates, and the result is a disordered region of defects and interstitials. Upon annealing, it is possible for this amorphisation to recrystallise into an ordered structure. The development of a graphitic structure over diamond will have effects on macroscopic properties such as thermal conductivity, as well as disrupting the integrity of the surrounding local structure.

Saada *et al.* [19] performed MD simulations of annealed radiation damage using the Tersoff potential [21]. An embedded damage-region within a diamond matrix

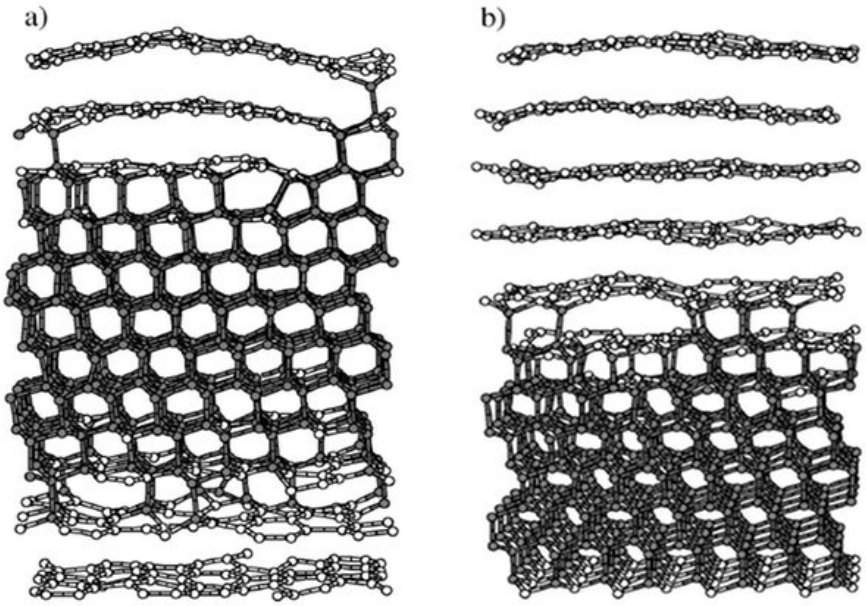

Figure 7: Snapshots during an (*npt*) Monte Carlo annealing simulation at 2250 K and 2500 K for respectively *a)* 'thick' diamond (111) slab containing 768 atoms and *b)* a diamond (111) surface with a fixed substrate, allowing no movement in the lowest two bilayers [18].

(5120 carbon atoms, 10×8×8 conventional unit cells) was first generated by imparting high momenta (416 eV = 8 × displacement energy of 52 eV) to 12 lattice atoms, all aimed at the same point. The subsequent local heating was then quenched back to 0 K within 2.5 ps. The result was a spherical volume of amorphous carbon of radius ≈1.4 nm. The extent of this 'heavy damage' proved to be large enough to be considered independent of the specifics of the 12 initially displaced atoms, such as the relative trajectories to lattice orientation.

Following preparation of this damaged region, the sample was gradually heated up to 3000 K and then annealed for 20 ps. The result was that the peripheral atoms around the core of the damaged region rearranged as threefold coordinated atoms (sp^2 bonded) in planar graphitic layers aligned with the diamond matrix (111) planes. The core of the damaged region, however, reformed a cluster of fourfold coordinated (sp^3 bonded) atoms. The segregation is attributed to the fact that core atoms are able to move comparatively larger distances of several lattice sites, as opposed to the limited movement at the damage/bulk-diamond interface. This was the outcome for a heavily damaged region only. The conclusion was that there is a critical density of defects of about 10^{22} vacancies/cm^3 above which the damaged region resolves into graphite (Figure 8). For densities below this a diamond-like

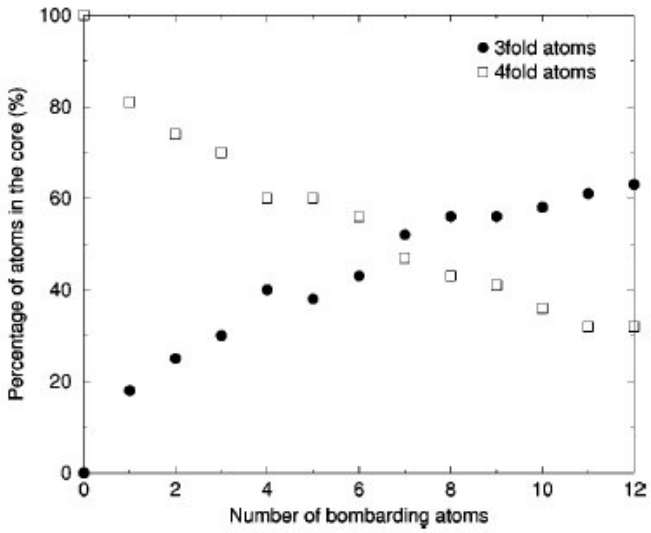

Figure 8: The proportion of threefold and fourfold atoms in the damaged core depends drastically on the number of bombarding atoms [19].

structure of sp^3 bonded atoms regrows.

3.3 Sputtering

The phenomenon of sputtering is generally referred to as being either physical (ballistic and energetic in nature) or chemical (low energy bond-breaking). Although a clean distinction between the two is not always clear, they do tend to dominate opposite ends of the incident particle energy spectrum, with a threshold between the two processes being somewhere around 20-40 eV (although this range can vary wildly). With regards to chemical sputtering, the interaction of hydrogen isotopes is only weakly dependent on isotope mass where activation energies are similar. Mass is much more important when studying physical sputtering.

The erosion of carbon by hydrogen ions is a thermally activated process and does not require energetic ions. In a fusion environment, plasma-facing components will be exposed to hydrogen and hydrogen isotope bombardment (0-200 eV ions [22]). On contact with the carbon surface, hydrogen can chemically form strong C-H bonds and further bombardment can induce chemical sputtering. Hydrocarbon molecules produced, C_xH_y, may be of varying size, x, and saturation, y. These sputtered products could then contaminate the plasma [23]. When Balooch and Olander [24] targeted graphite with atomic hydrogen they observed that, below about 800 K, CH_4 was the dominant reaction product and above 1200 K, it was C_2H_2. It is

believed that the type of hydrocarbon sputtered is dependent on the incident ion penetration depth, with CH_y and C_2H_y being the dominant products at low energies (<15 eV). There also exists a dependence on the incident angle of bombardment, since a glancing impact may not penetrate as deep as one that is normal to the surface. Molecular dynamics studies have reported an angular dependence that decreases with lower incident energies (to within the chemical sputtering regime). In a study where a-C:H targets were bombarded with tritium [22] it was found that ions over a range of incident angles showed yield differences of the order ten-fold for energies of 150 eV depending on angle of incidence, but with no discernible difference in yield for ions at about 50 eV, regardless of angle.

3.3.1 Chemical Sputtering

From experimental observations Güntherschulz first highlighted the importance of chemical interactions to the erosion of bombarded material [25]. A definition of chemical sputtering has been offered as "a process whereby ion bombardment causes or allows a chemical reaction to occur which produces a particle that is weakly bound to the surface and hence easily desorbed into the gas phase" [26]. Generally, when incident ions chemically interact with plasma-facing surface atoms, the subsequent release of atoms and molecules from the surface is referred to as chemical sputtering. The incident reactive ions can form compounds with the surface of the target material. Depending on the bonding properties of this surface layer, this can increase or decrease sputter yield [27]. This process typically dominates erosion processes at low ionic energies (<100 eV) and high surface temperatures. This is an especially important problem for carbon based materials and is susceptible to a complex mixture of parameters including surface temperature, incident ionic species and energy as well as intensity. With carbon, incident hydrogen ions may form loosely bound hydrocarbon molecules saturating surface carbon atoms which reduces the ionic threshold energy for sputtering. For example, at room temperature this can be to about 2 eV for graphite. Where the surface temperature is above 400 K, the thermal release of hydrocarbons occurs. However, this increase in chemical erosion is capped and then decreases for temperatures above 600 K where hydrogen molecular recombination can occur before the complete hydrogenation of the surface. This trend is depicted in Figure 9 showing a maximum yield for when surface temperature is 600-800 K.

There have been many studies into understanding the individual steps behind the process of chemical erosion of carbon by incident hydrogen. Figure 11 is taken from [28] and emphasises thermal activation barriers and the formation of hybrid carbon

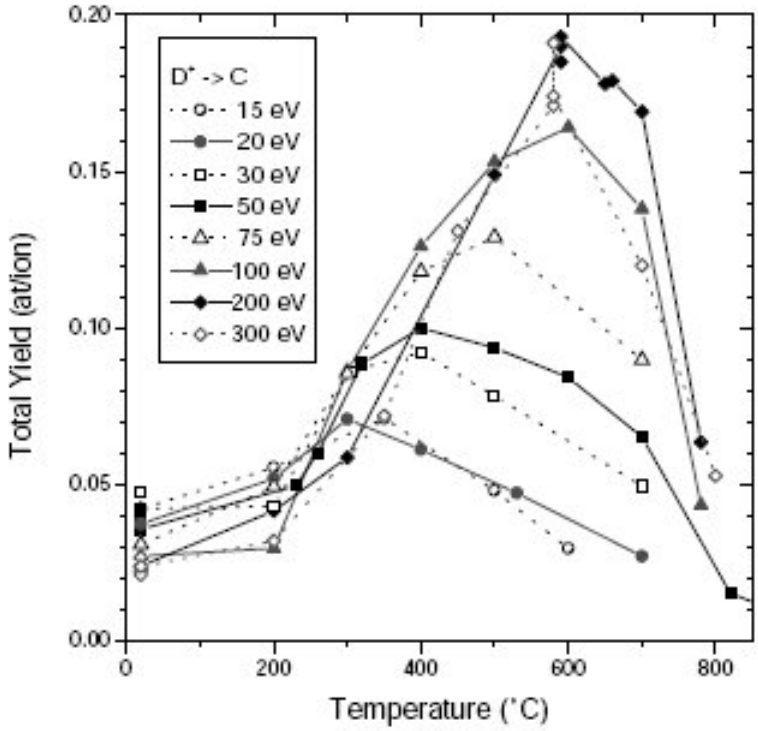

Figure 9: Temperature dependence of the erosion yield of pyrolytic graphite by deuterium ion bombardment at different ion energies as measured by weight loss [3].

sp^x radicals in between sp^2 and sp^3 as the crucial step to forming sputter products. This work centred on the bombardment of graphite but is assumed to hold for other carbon structures. Figure 11 shows four individual processes. There is the hydrogenation of carbons, not thermally activated, but proportional to the cross section k_H. Irradiation of this leads to hydrogen desorption with cross section k_D. There is the thermally activated CH_3 chemical erosion above 400 K at rate k_X. Above 600 K the thermal decomposition of sp^x radicals and recombination of H_2 inhibits the reaction process and reduces the yield for higher temperatures. The combined effects of these two processes results in a peak yield over a range of substrate temperatures (see Figure 9). The conclusion was that sputter yield for an incident flux is not related to hydrogen concentration, but to the concentration of hydrogenated sp^x centres, which in turn is directly proportional to the sp^3 concentration.

The first experimental investigations into chemical sputtering demonstrated a temperature dependence of sputter yields for graphite [29, 30, 31, 32]. With increasing temperature the C-H reaction rate increases but then above 800 K the recombination of H_2 reduces the surface saturation and thus sputter yield. Incident

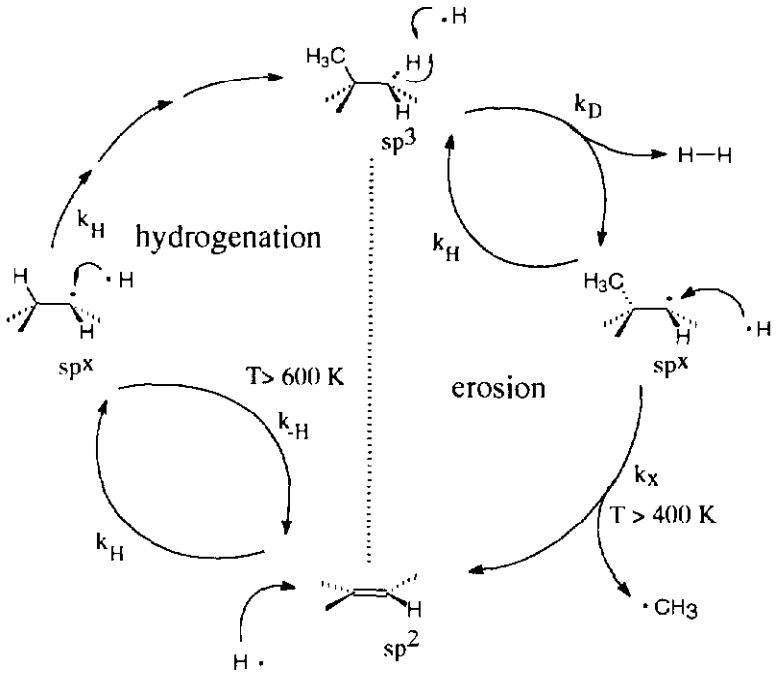

Figure 10: Schematic of chemical erosion cycle as presented by Horn *et al.* [28]. Thermally activated processes are indicated.

ion energy also influences maximum yield. For graphite, it was found that between 300 eV and 3000 eV ions on pyrolytic graphite had a yield peak at 800 K [33]. With lower bombarding energy (100 eV) the maximum peak broadens and shifts to a slightly lower temperature (600 K), but the methane production yield is higher. Yamada *et al.* [34] found that at a given temperature there is an incident energy which gives a maximum yield, typically about 1 keV. Roth *et al.* [29] found this energy dependent maximum to reduce with decreasing substrate temperature.

As well as a dependence of incident ion energy, the temperature of sputter yield maxima were found to increase with increasing ion flux [35, 36, 37]. Above fluxes of 10^{21} $\mathrm{m^{-2}s^{-1}}$ the temperature maximum reaches about 1000 K. It has been suggested that at this temperature the system shifts from CH_4 production to H_2 release [38] and yield decreases with further increasing flux. Normalizing the data to 30 eV bombardment Roth *et al.* [39] fitted using Bayesian probability theory [40] (Equation 2; low-flux yield $Y_{low}\,(E,T) = 0.08$; threshold flux $\phi_0 = 6 \times 10^{21}$ $\mathrm{m^{-2}s^{-1}}$; $z = 0.54$.)

$$Y\left(E,T,\phi\right) = Y_{low}\left(E,T\right)\frac{1}{1+\left(\phi/\phi_0\right)^z} \tag{2}$$

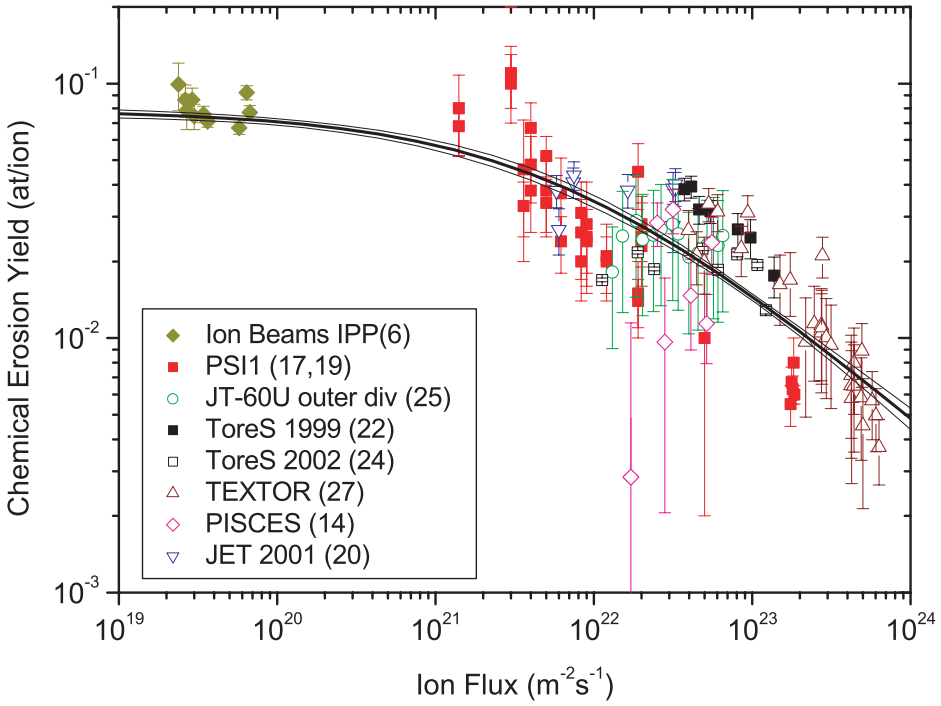

Figure 11: Dependence of chemical sputtering yield, Y, (at T_{max}) on incident flux, ϕ. Data normalised to incident ion energies of 30 eV. Plot following Equation 2. Taken from [39]

Swift Chemical Sputtering

In 2000 Salonen *et al.* identified the mechanism of 'swift chemical sputtering' [41] in which C-C surface bonds are broken by incident ions which do not have enough kinetic energy to physically sputter (see Figure 12). With swift chemical sputtering the impinging ions briefly find themselves between bonded carbon atoms thus repelling them and breaking the C-C bond. Different from conventional physical sputtering, this process has an upper ion energy limit as well as a lower one. The reason for this being that not only do the incident ions require enough energy to position themselves between two bonded carbon atoms, but too much energy will see that they spend too little time there to repel the carbons and will instead move on to penetrate deeper into the sample network. Since this interaction time depends

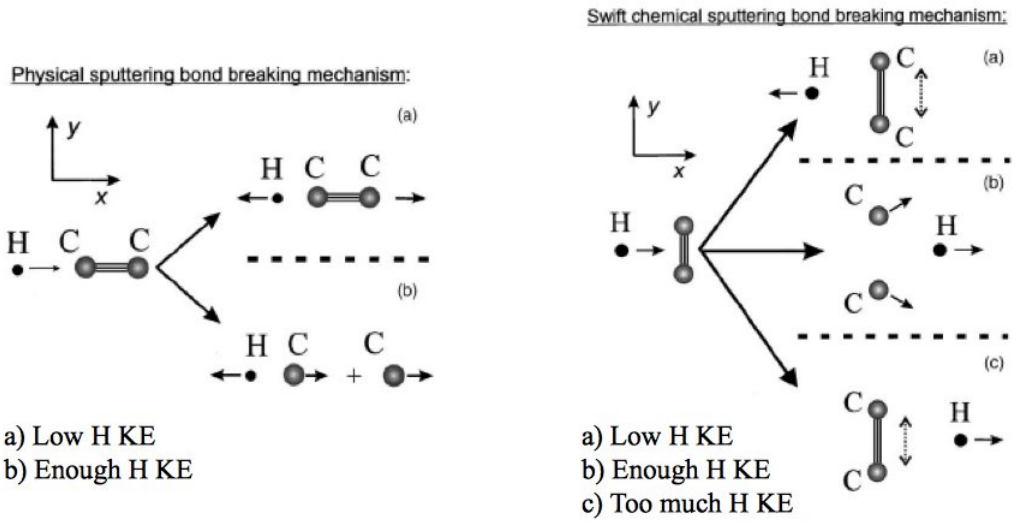

Figure 12: Mechanisms of physical and swift chemical sputtering of carbon in target sample for bombarding hydrogen ion kinetic energies above and below required threshold energies [41]

on ion velocities, it also depends on ion masses and therefore there is also a dependence on isotopic species, with heavier hydrogen isotopes having the larger 'energy windows'. This mechanism requires timescales of the order of 10 fs to simulate, and has also been extended to helium ions [42].

3.3.2 Physical Sputtering

When plasma ions impact on solid surfaces they elastically impart some kinetic energy to the wall atoms. If these target atoms are then energetic enough to overcome surface binding energy they can escape back out towards the plasma where they are then said to have physically sputtered. Incident ionic energies can range from ≈500 eV at the chamber midplane to about ≈15 eV around the divertor (with an upper limit at the divertor expected to be about 100 eV) where 15 eV is below the typical physical sputtering threshold for most materials [3]. The threshold energy of physically induced sputtering due to light ions bombarding heavy materials can be analytically approximated by the following equation[2] .

$$E_{th} = \frac{(M_1 + M_2)^4}{4M_1M_2(M_1 - M_2)^2} E_s \tag{3}$$

In Equation 3, M_1 and M_2 are incident and target particle masses respectively and E_s is the surface binding energy. This illustrates the dependence of the threshold

[2]Equation 4 of [3], which was taken from [43]

energy of a surface incident with light-ions on the surface atomic mass.

The sputtered yield is dependent on incident energy in the following way[3]:

$$Y = QS_n(E)\left(1 - \frac{E_{th}}{E}\right)^2\left(1 - \left(\frac{E_{th}}{E}\right)^{\frac{2}{3}}\right) \tag{4}$$

$S_n(E)$ describes the energy deposited in elastic collisions. Values for the parameters Q and E_{th} can be found in reference [45].

Hydrogen Enhanced Physical Sputtering

Although chemical sputtering may be the dominant process in the divertor region, the way in which carbon and hydrogen interact will play an important role. It is therefore interesting to observe the effect hydrogen has on physical sputtering. Maya *et al.* [46] used the Brenner potential [47] in MD studies, bombarding a-C:H films with 150 eV Ar ions in a background of low energy (0.5 eV) hydrogen, and found that the effects of what is essentially physical sputtering may be enhanced by the presence of hydrogen at the surface. Due to the ion bombardment, surface carbon bonds are broken (to a depth ≈8 Å) by conventional physical sputtering. If not ejected from the surface they would perhaps reform C-C bonds, however, the hydrogen atoms present passivate these open bonds resulting in linear hydrocarbon chains projecting out of the surface. A hydrocarbon group with one C-C bond connecting it to the bulk structure will erode easier than one that is multiply connected, and so it was found that this new surface arrangement was prone to releasing unsaturated hydrocarbon molecules upon further bombardment. Thus the presence of hydrogen resulted in a sputtering yield higher than that expected from the simple addition of reported chemical and physical levels. Maya *et al.* refer to this mechanism as 'hydrogen enhanced physical sputtering'.

In addition to the amplified effects of physical sputtering, the species of molecule ejected were in general seen to contain more carbon atoms. Specifically, hydrocarbon chains containing four to six carbons were released whereas in the absence of hydrogen, molecules of no more than three carbons were observed. The same study also reported that ion bombardment did not result in additional hydrogen diffusion into the bulk material at 300 K.

[3]Equation 5 of [3], originally [44]

3.4 Tritium Retention

The retention of hydrogen isotopes, especially tritium, is a major issue for reactor design and carbon in particular. Due to strong carbon/hydrogen bonding, carbon is a particularly problematic material as it can retain tritium at and just below the surface. The term hydrogen is used in this section to refer to hydrogenic ions in general.

In limiting hydrogen retention the diffusivity and solubility of the material needs to be understood. For tungsten and beryllium the hydrogen-solubility is known to be very low. This is not the case for the array of carbon structures, however, but an already hydrogen-saturated surface may reduce the solubility of the material and the use of a porous structure offers a solution to the problem of retention directly by allowing easier tritium transport (and thus escape) within the sample. This idea is behind the inclusion of nano-tubes or other fullerenes in building a matrix of channels in CFCs. In conjunction with research into low tritium retention materials is the development of techniques to remove deposited material. These include high temperature baking ($>$ 300 K) in an oxygen atmosphere and low-pressure plasma discharge cleaning [48].

3.4.1 Hydrogen Trapping and Release

Incident hydrogen isotopes will eventually saturate the surface with a layer of thickness dependent on ionic stopping range (*i.e.* incident ion energy) [49]. The hydrogen/carbon ratio at which saturation occurs will depend on the structure, but for graphite this can be ≈0.4-0.5 H/C at room temperature with graphite saturation occurring at coverages of about 10^{21} m^{-2} in tokamak conditions [3]. Generally this decreases with higher temperatures [50]. Further exposure will have little effect on the hydrogen concentration unless there is opportunity for surface diffusion along porous channels or grain boundaries [51, 52]. Where channels exist it may be possible for hydrogen to transport deeper and potentially become trapped, typically at defects in the crystal structure. Defects may be limited by careful manufacture, but they can easily evolve when the sample is exposed to radiation. Thus, although porosity may provide accelerated hydrogen release, it can also allow deeper penetration and access to defects.

Increasing the temperature of a saturated surface would encourage the thermal release of hydrogen. For hydrogen implanted graphite at temperatures above 800 K, molecular hydrogen release begins, gradually becoming atomistic at about 1300 K and above [53].

Although once a steady-state erosion is established the incident and reflected fluxes on a hydrogen saturated surface are similar, the incident ions compete with, and can replace, ions already present [54, 55, 56]. Thus there exists the possibility of exposing a tritium-rich surface to bombardment of another isotope by some plasma-operational mechanism in an effort to induce tritium release via isotope exchange and so reduce the wall tritium inventory.

3.4.2 Co-deposition

Eroded surface material can chemically combine with isotopic hydrogen, become ionised and accelerate towards the wall and redeposit. Carbon and hydrocarbon will continually erode from and gather on the sample surface. When this build up exceeds erosion there exists a net deposition. Unlike tritium retention by implantation via bombardment, co-deposition increases the thickness of the hydrogen retentive surface layer, and thus its tritium containing capacity. For low density polymer-like carbon films exposed to a low temperature plasma, with incident particle energies below 100 eV, co-deposition accumulates with a high H/C density ratio of ≈0.8-1 [57]. Such conditions would exist in the vicinity the divertor. It has been determined that co-deposition is the dominant process of long-term fuel retention with carbon plasma-facing materials and so the major drawback for carbon is its tendency to chemically trap tritium in co-deposited layers at a rate estimated to be 5 g (±50%) T/(400 second pulse) [7]. There is also the concern that carbon and hydrocarbons that have eroded from the vertical target plates can form thick, hydrogenated coatings on cool surfaces which may then also trap tritium. Studies have shown that the co-deposition of carbon-tritium molecules can vary from 10% to 40% of the amount of fuel introduced [58].

3.5 Diamond Exposed to Plasmas

Polycrystalline diamond films have excellent thermal properties with thermal conductivities roughly a third of that of crystalline diamond, which is one of the highest known at 900-2320 W/(m.K) (with an impressively low thermal expansion factor of 0.8 μm.m^{-1}K^{-1}). They also exhibit low sputtering levels and are practical to produce, costing around US$ 30,000 kg^{-1} [5]. Diamond is also relatively robust against irradiation (with a displacement energy at about 80 eV) and the high covalent bonding energy means good sputter resistance.

If diamond is to be considered as a PFM (poly-crystalline films, for example) then understanding its limitations is essential in optimising design. Although offering exceptional thermal conductivity and low thermal expansion, carbon-based materials are problematically prone to tritium retention. This encompasses surface damage via sputtering and redeposition. Specifically for diamond, though, is the issue of thermally induced graphitisation - the three-fold sp^2 bond hybridisation of carbon is energetically favorable over four-fold sp^3 bonding. Such a phase change may also be enhanced by the effects of radiation damage. The understanding and suppression of this process would be greatly beneficial.

At this level, the only mechanical property expected to drastically change is the thermal conductivity. A three-dimensional diamond-like carbon structure with high graphitisation energy will limit any volume change. For a temperature range 600-1500 K, dimensional change due to irradiation would be less than 0.1-0.2% [59, 60]. At high temperatures (1100-1300 K), defects could even be partially annealed, limiting reductions in thermal conductivities to between 100 and 150 W/(m.K) [10], which is at the lower end of desirable performance criteria.

Recently there have been some promising experimental results which suggest that diamond may be a suitable candidate for a divertor region plasma-facing material.

De Temmerman *et al.* [61] exposed micro-crystalline (MCD) and nano-crysatlline (NCD) diamond coated molybdenum substrates and graphite samples side-by-side to high density (3-8$\times 10^{19}$ m^{-3}), low temperature (0.3-2.0 eV) plasmas (Figure 13). The sample temperature of the graphite sample was measured to be 800-1000 °C during exposure (they were unable to directly measure the diamond sample temperatures either because temperatures were below the detection limit of 500 °C or because of the unknown emissivity of diamond). Their MCD and NCD crystalline grain sizes were 0.5-2.0 μm and 50 nm respectively. They observed that the NCD and the MCD samples showed a reduced chemical erosion compared with the graphite by a factor of 2. This ratio was also observed in earlier experiments for much higher ion energies of 200-800 eV [62]. Between the diamond samples, De Temmerman *et al.* found the NCD coating showed the largest emission of CH, possibly linked to the increased amount of sp^2-like bonding present at the surface due to a higher density of grain boundaries [63]. Boron doping of the diamond showed further reduction in sputter yield [64, 65] as well as reducing arcing by increasing the electrical conductivity of the sample.

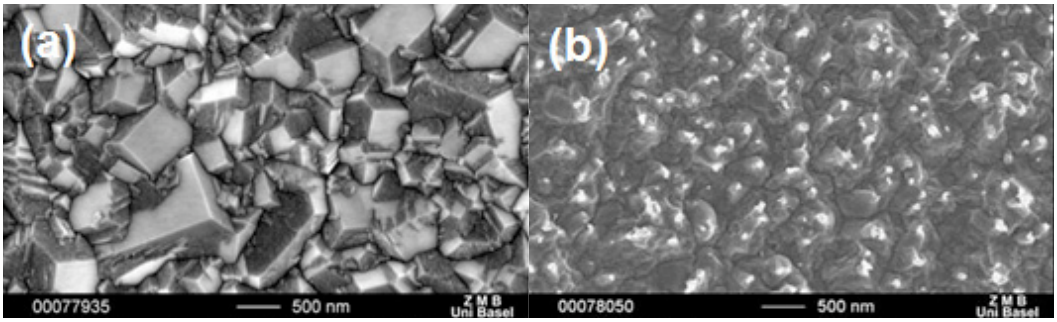

Figure 13: The 10 μm thick MCD film of grain sizes 0.5-1.0 μm a) pre-exposure to the plasma and b) after exposure to a fluence of 7×10^{24} ions m^{-2}. Reproduced from [61]

After exposure to tokamak plasmas (in MAST) Porro *et al.* [14] detected the partial amorphisation of diamond surfaces within the penetration depth of the incident particles. This conclusion was based on the observation of increased sp^2 bonded carbon at the surface following bombardment using Raman spectroscopy. They also concluded that the MCD surfaces showed better resistance to the plasma impact than did the NCD. All incident deuterium was detected in the first 250 nm of the surface, with the MCD retaining almost a third the amount of fuel as did the NCD, something again attributed to the relative surface densities of grain boundaries.

In the same study, Porro *et al.* exposed MCD, NCD and graphite samples to a linear plasma device (Pilot-PSI) and found that the temperature of the graphite sample (1000 °C) was systematically much higher than for the diamond samples (300 °C). This, they attributed to the high thermal conductivity of diamond in comparison to graphite. It was also concluded that the behavior of diamond did not tend to that of graphite with increasing fluence (total bombardment per unit area for a given period of time).

To summarise, carbon materials have high thermal conductivity and low thermal expansion which make them suitable as a PFM where they will experience intense heat loads. Of all of carbon's structures, these desirable features are most pronounced in diamond. If material is sputtered from the surface and contaminates the plasma, a low Z number material, such as carbon, is preferable. Diamond has shown promise in this respect with sputter yields reported to be half that of graphite. However, due to its reactivity with hydrogen, high levels of tritium retention is a potential disadvantage faced by all carbon based materials. The structure of the material is expected to play an important role here.

4 Modelling

There are various techniques for calculating the properties and structural configurations of simulated materials. Monte Carlo (MC) methods take a sample and randomly vary some aspect marginally (such as individual atomic positions or number of atoms present) whilst evaluating the total configuration energy before and after the alteration, and subject to some probabilistic selection criteria, it may be accepted. One variation attempt represents one MC step, which is repeated many times over and so the simulation evolves.

Whereas MC randomly samples energy profiles, molecular dynamics (MD) simulations attempt to represent the physical process by which particles interact. Rather than imposing random perturbations in the system, MD directly evaluates inter-atomic forces and allows the system to respond accordingly. Newton's equations of motion are solved at regular time-steps in order to update atomic accelerations, velocities and thus positions for the next time step.

First principles MD evaluates inter-atomic forces directly from fundamental quantum-mechanical theory, whereas traditional MD is computationally cheaper and uses an empirically parametrised potential to describe bond strength as a function of the atomic local environments (for example, nearest neighbour separation, bond angles and local coordination numbers of neighbours). The analytic potential of classical MD is differentiated with respect to position in order to obtain forces and thus accelerations.

Both MC and MD modelling techniques have been employed in studying a range of properties, such as phase transitions and surface reconstructions. However, these two methods are not necessarily comparable. Dynamical information, such as atom velocity and trajectory, is lost with MC, although it is able to sample probabilistically less likely structural changes, an advantage over MD which may be constrained to regions of phase-space isolated by large potential barriers. Timescales also differ. Although MC does not necessarily simulate a duration of time, if atomic movements are considered to occur on a pico to nanosecond scale, an MC simulation of 100,000 moves per atom would correspond to 10^{-7} to 10^{-4} seconds. This is substantially longer than MD simulated times which are of the order of nanoseconds. In both cases the principal constraints on total simulated time scale are computational processing speed and code efficiency.

If an understanding of the dynamics of a system is desired, rather than solving

mountains of complex first principles calculations, classical MD offers a compromise in that, although relying on what is essentially only a coarse approximation to atomistic interactions (the empirical potential), depending on the the success of that approximation, it allows a range of useful dynamical properties to be observed in detail inaccessible to experiment. The whole sequence of events in projectile-surface interactions and phase-transitions are recorded whilst the nanoscopic topography of the structure is easily observed and manipulated, and all this whilst recording dynamical properties of the system. An accurate empirical potential contains all the necessary assumptions relating to system properties, such as binding energies, and melting temperatures. Overwhelmingly, it is the accuracy of this empirical potential which influences the reliability of molecular dynamics simulations. Although the time-scale and sample-size of the simulation is drastically limited by computational capability, this approach (over, for example, Monte Carlo methods) also offers interesting graphical representations of the detailed processes observed.

4.1 Molecular Dynamics Setup

In this study the MD code DL_POLY_3 [66] was used employing the AIREBO potential [67] to evaluate carbon and hydrogen/tritium interactions. As with any other MD package, DL_POLY requires an input list of the atomic names and positions: the CONFIG file. As well as coordinates, atomic velocities and accelerations are optional if this is a continuation from a previous simulation (in which case a REVIVE file is also normally required). The inter-atomic potential desired is named and defined in the FIELD file, where all necessary user variable parameters required for that potential are listed. Finally a CONTROL file is used to state the nature of the simulation by operational variables (such as time step size, temperature, thermostat required, *etc*...) and output requirements (in addition to the standard OUTPUT file other files such as trajectory history, radial distribution and defect analysis may be required).

On starting the simulation, input files are read in and system parameters and settings are initialised as required. Once this is done, the main MD loop is iterated for the required number of time steps, at each of which atomic forces are evaluated (here by the *airebo_forces* subroutine) and positions updated using an integration algorithm solving Newton's equations of motion. The thermostat is used to regularly check and maintain physical properties of the sample, such as temperature, by scaling velocities appropriately.

4.1.1 Integration Algorithm

Particle interactions within the simulated system are described by a potential which is dependent on, among other things, inter-atomic separation. The gradient of this potential gives us the strength of those forces due to attraction and repulsion. Since time is discretised, Newton's equations of motion are solved at each time step and so values for individual particle acceleration, velocity and thus atomic positions are updated for the next time step. This introduces errors since we are dealing with variables which are not continuous in time, and which share an inter-dependency.

The specifics of this update depend on the algorithm of choice (*e.g.* Verlet, Velocity Verlet and Leap-Frog Verlet, Figure 14). In this study, the Velocity Verlet (VV) algorithm was employed, developed by Swope *et al.* [68] in 1982. In an effort to minimise rounding errors, it takes advantage of partial integration over half time steps.

From initial values for position, $\mathbf{r}(t)$, velocity, $\mathbf{v}(t)$, and acceleration, $\mathbf{a}(t)$, at time t, values at time $t+\delta t$ are arrived at by using Taylor expansions and half-time-steps by the following procedure.

$$\mathbf{r}(t+\delta t) = \mathbf{r}(t) + \delta t \mathbf{v}(t) + \frac{1}{2}\delta t^2 \mathbf{a}(t) \tag{5}$$

$$\mathbf{v}\left(t+\frac{1}{2}\delta t\right) = \mathbf{v}(t) + \frac{1}{2}\delta t \mathbf{a}(t) \tag{6}$$

Forces and thus accelerations at time $t+\delta t$ are then evaluated by the forces subroutine based on positions at time t and used to complete the velocity evaluation over the full time-step.

$$\mathbf{v}(t+\delta t) = \mathbf{v}\left(t+\frac{1}{2}\delta t\right) + \frac{1}{2}\delta t \mathbf{a}(t+\delta t) \tag{7}$$

4.1.2 Thermostat

Depending on the requirements of the simulation in hand, various macroscopic properties may be designated as varying or fixed. For example these may be total system volume, energy, temperature, pressure and number of particles present. In the course of this study the Nosé-Hoover (*nvt* and *npt*) and Langevin thermostats[4] were used. The Nosé-Hoover thermostats holds either volume or pressure constant while scal-

[4]See the DL_POLY_3 manual: `http://www.cse.scitech.ac.uk/ccg/software/DL_POLY/`

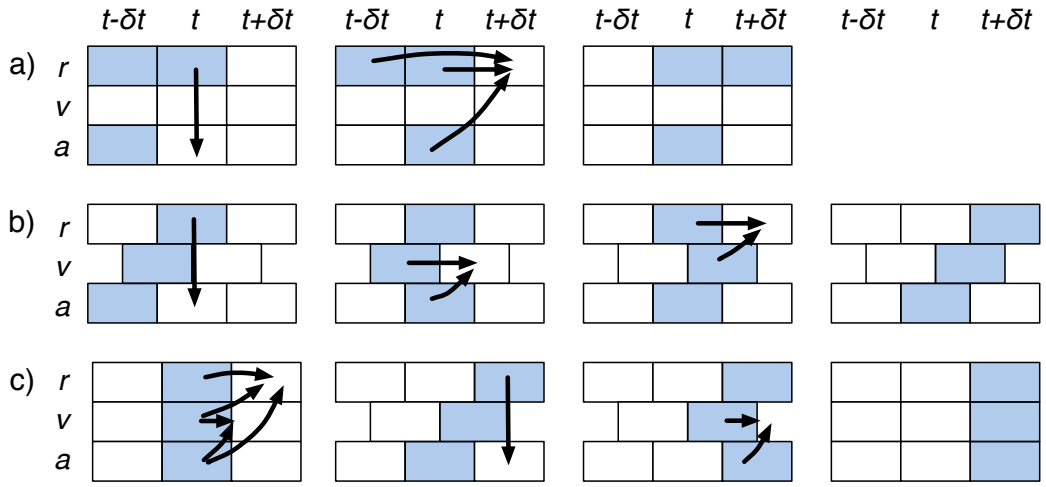

Figure 14: Schematic representation of the integration procedures where stored values are represented by shaded boxes. a) Original Verlet, b) Leap-Frog Verlet & c) Velocity Verlet

ing all velocities based on how much total thermal energy of the system is off the target temperature by. The Langevin thermostat stochastically scales velocities of selected atoms to a desired temperature, effectively coupling the system to a heat-sink. Atoms are typically chosen to be only those at a given distance from the edges of the simulation cell.

These macroscopic attributes are related to individual atomic kinetics by way of the classical equipartition of energy over all degrees of freedom. Thus temperature and velocity are considered as related in the following way (assuming the system is in thermal equilibrium).

$$\langle v_\alpha^2 \rangle = \frac{k_B T}{m} \tag{8}$$

Where v_α is a particle's α component of velocity (e.g. a cartesian or polar dimension). This is extended as a sum over all particles, N, to define the instantaneous temperature, T, of the system at time t.

$$k_B T\,(t) \equiv \sum_{i=1}^{N} \frac{m v_{\alpha,i}^2\,(t)}{3N} \tag{9}$$

At the heart of molecular dynamics simulations are Newton's equations of motion (Equations 10 and 11). These are iteratively evaluated and particle trajectories due to inter-atomic interations are mapped.

$$\frac{d\mathbf{r}(t)}{dt} = \mathbf{v}(t) \tag{10}$$

$$\frac{d\mathbf{v}(t)}{dt} = \frac{\mathbf{f}(t)}{m} \tag{11}$$

By applying modifications to Newton's equations it is possible to control various macroscopic properties such as temperature, volume and pressure.

Nosé-Hoover (*nvt*) Thermostat

The *nvt* Nosé-Hoover thermostat holds MD cell dimensions and atom content fixed whilst allowing the control of system temperature by the introduction of an artificial thermostat mass, q_{mass}. This is defined by target system energy (from target temperature, T_{ext}, where f in Equation 16 is degrees of freedom), σ, and a time constant of temperature fluctuations, τ_t. Using these, a coefficient, $\chi(t)$, is introduced in addition to the forces evaluated using the inter-atomic potential (Equation 13). This modification to acceleration is proportional to velocity and acts as a friction term, scaling temperature.

$$\frac{d\mathbf{r}(t)}{dt} = \mathbf{v}(t) \tag{12}$$

$$\frac{d\mathbf{v}(t)}{dt} = \frac{\mathbf{f}(t)}{m} - \chi(t)\,\mathbf{v}(t) \tag{13}$$

$$\frac{d\chi(t)}{dt} = \frac{2E_{kin}(t) - 2\sigma}{q_{mass}} \tag{14}$$

$$q_{mass} = 2\sigma\tau_t^2 \tag{15}$$

$$\sigma = \frac{f}{2}k_B T_{ext} \tag{16}$$

Nosé-Hoover (*npt*) Barostat

The Nosé-Hoover Barostat acts much in the same way as the above described thermostat but allows for variations in cell dimensions. To do this, as well as the thermostat co-efficient, $\chi(t)$, Newton's equations of motion are also coupled to a barostat co-efficient of friction, $\eta(t)$, which maintains a desired system pressure.

$$\frac{d\mathbf{r}(t)}{dt} = \mathbf{v}(t) + \eta(t)\left(\mathbf{r}(t) - \mathbf{R}_0(t)\right) \tag{17}$$

$$\frac{d\mathbf{v}(t)}{dt} = \frac{\mathbf{f}(t)}{m} - \left[\chi(t) + \eta(t)\right]\mathbf{v}(t) \tag{18}$$

$$\frac{d\chi(t)}{dt} = \frac{2E_{kin}(t) - 2\sigma - k_B T_{ext}}{q_{mass}} \tag{19}$$

As for the (nvt) thermostat, σ represents the target thermostat energy, and q_{mass} is the artificial mass of the thermostat. Also included here is a correction for the system centre of mass, $\mathbf{R}_0$.

In a similar way to how the differential of $\chi(t)$ is related to the difference between system energy and desired energy, so the differential of $\eta(t)$ is to the difference between instantaneous pressure, $P(t)$ (evaluated from kinetic energy and virial terms), and the desired average pressure, P_{ext}. The added artificial barostat mass is p_{mass}, and τ_P is the user defined time constant of pressure fluctuations.

$$\frac{d\eta(t)}{dt} = 3V(t)\frac{P(t) - P_{ext}}{p_{mass}} - \chi(t)\eta(t) \tag{20}$$

$$p_{mass} = (f+3)\,k_B T_{ext}\tau_P^2 \tag{21}$$

To accommodate a constant pressure, the MD cell volume is allowed to change, keeping the shape of the cell constant, according to the following relationship.

$$\frac{dV(t)}{dt} = 3\eta(t)V(t) \tag{22}$$

Langevin Thermostat

Within fluids, particles randomly interact with others in their vicinity stochastically as described by Brownian Mechanics. It is from this principle that a Langevin thermostat controls the temperature of a system, in effect implicitly representing this interaction as atoms vibrate about lattice sites in a solid. Developed by Paul Langevin, every particle considered is coupled to a viscous background and a stochastic heat bath. This serves to reduce the velocity of 'hot' particles and stochastically increase the velocity of 'cold' particles towards the desired temperature.

$$\frac{d\mathbf{r}(t)}{dt} = \mathbf{v}(t) \tag{23}$$

$$\frac{d\mathbf{v}(t)}{dt} = \frac{\mathbf{f}(t) + \mathbf{R}(t)}{m} - \chi\mathbf{v}(t) \tag{24}$$

In Equation 24, particle accelerations are obtained from forces evaluated using the inter-atomic potential which are then modified by a stochastic force, $\mathbf{R}(t)$. Accelerations are then further moderated by a friction term proportionate to velocity.

As it is implemented in DL_POLY_3, the Langevin thermostat enables the user to temperature scale the outer perimeter of the MD cell to a designated depth.

4.1.3 Periodic Boundary Conditions

Simply modelling the interactions between a list of particles in effect treats the simulation as a sample isolated within a void. What is more often desirable is the study of a region that is otherwise surrounded by a continuation of matter. For example, particles suspended in a solution or the continuation of a crystal lattice. Simulating ever larger samples would reduce the influence of edge effects, but this is computationally costly. A commonly used method of removing these surfaces all together is the use of periodic boundaries. This simply means that the simulated cell is replicated across boundaries in each Cartesian direction. For example, if a particle leaves the cell boundary in the negative x-direction, it reappears from the positive x-direction.

Although this may be considered as creating an infinitely large cell in that there are no boundaries, the actual simulated size is still important. Larger samples reduce consequences due to self-interations. For example, if particles experience long-range forces to a distance of 10 Å, then it would make sense to have a cell size at least twice a large as this to avoid self-interaction or two particles interacting twice in opposite directions.

Generating periodic boundaries is normally done in simulation codes by temporarily creating additional atoms just beyond the edge of their MD cells. In Figure 15 a Cartesian two dimensional MD cell has been copied eight times in creating this buffer of image-atoms. A more efficient method in practice is to only copy those image-atoms which are adjacent to the MD cell perimeter. DL_POLY_3 does this by constructing a 'halo' around the MD cell (Figure 16). This technique is also used in distributing a simulation across multiple processing units (see Section 4.3 on halo construction and parallelisation).

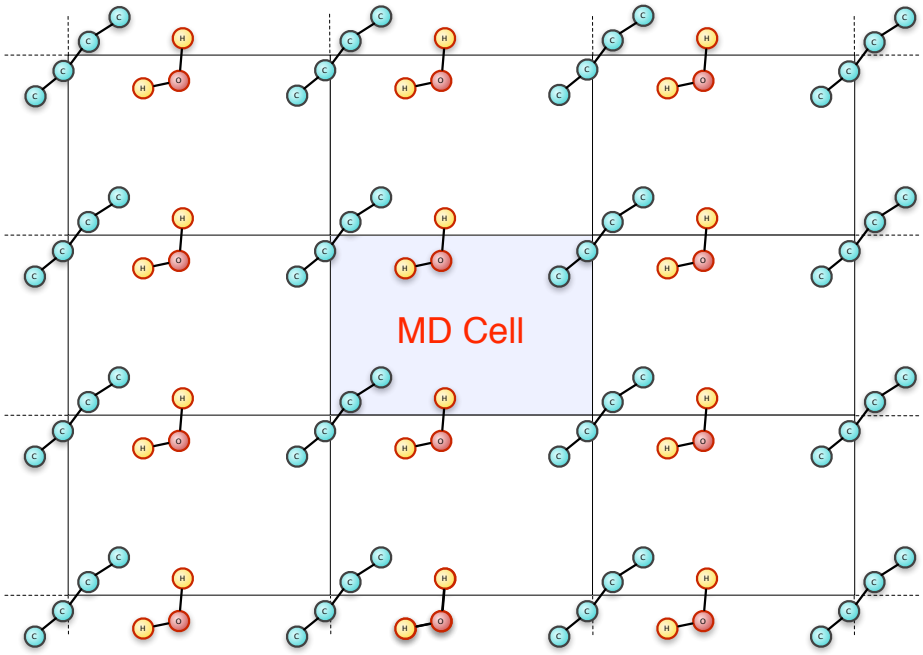

Figure 15: Two dimensional schematic of periodic boundaries. The two molecules in the MD cell both leave the cell and re-enter on the respective opposite sides.

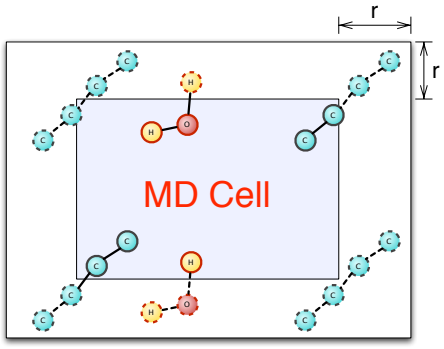

Figure 16: Two dimensional schematic of periodic boundaries created using 'halo' atoms. There are only seven real atoms (solid outlined atoms) in the MD cell, but these may be replicated more than once as halo atoms (dashed outlined atoms). In this example the water molecule is only copied once, but the carbon chain is copied three times. The thickness of the halo, r, is determined by the range of the inter-atomic potential.

4.1.4 Potential

The method by which atomic positions are re-evaluated over periodic time-steps mapping trajectories in time is described above in Section 4.1.1. The dynamical properties of the system are derived from three-dimensional lists of three properties of each particle: position, velocity and acceleration. Using basic classical mechanics,

at each time-step atomic positions, $\mathbf{r}_i$, are updated using atomic velocities. Velocities, $\mathbf{v}_i$, also relate to kinetic energy and so the temperature of the system. Similarly, these velocities are updated using the acceleration of each particle. Acceleration, $\mathbf{a}_i$, is derived from inter-atomic forces using Newton's second law, and inter-atomic forces, $\mathbf{f}_i$, are obtained from the first differential in space of the inter-atomic potential, $\mathbf{U}_i$.

$$\mathbf{f}_i = m\mathbf{a}_i \tag{25}$$

$$\mathbf{f}_i = -\frac{\partial U_i}{\partial \mathbf{r}} \tag{26}$$

It is therefore clear that the accuracy with which a simulation represents real processes depends on the accuracy of the inter-atomic potential. In molecular dynamics using an empirical potential, that interaction typically takes an analytic form which has been parameterised to mimic experimentally observed properties.

At each time-step the MD code will loop over all atoms, i, and evaluate the strength of its bonding to neighbour atoms, j. The simplest evaluation is a two-body potential: one that only considers atoms i and j and vector separation $\mathbf{r}_{ij}$. An example of this is the Lennard-Jones potential (Equation 28).

$$r_{ij} = |\mathbf{r}_j - \mathbf{r}_i| \tag{27}$$

$$U_{ij}\left(r_{ij}\right) = 4\epsilon\left[\left(\frac{\sigma}{r_{ij}}\right)^{12} - \left(\frac{\sigma}{r_{ij}}\right)^{6}\right] \tag{28}$$

Although this is a computationally cheap potential and good in the simple case of soft-spheres in a fluid state, it does not consider the detail of the chemical environment, for example, bond rotations, lattice structure or number of bonded neighbours. Additional considerations such as these are important when simulating covalently bound lattice structures such as diamond and graphite. To include factors such as this *bond-order* potentials were developed that were able to adapt the bond environment.

Early simulations of the sputtering of organic molecules centred on course-grain methods which fundamentally did not allow for molecule fragmentation - a process which plays a vital role in the development of a carbon-based surface topography. One of the first empirical bond-order potentials employed in the simulation of carbon was the the Tersoff potential (Equation 29) in 1989 [21]. Although a two-body

potential, in evaluating the *i*-*j* bond it also considers *iatom's* other neighbours, *k*, though the bond-order term $\mathbf{b}_{ij}$. In doing this a preference for three nearest-neighbours (sp^2 bonding) and lattice structure (bond angles, θ_{jik}) are incorporated.

$$U_{ij}\left(r_{ij}\right) = U_{ij}^{repulsive} + b_{ij}U_{ij}^{attractive} \tag{29}$$

The Tersoff potential is still used today due to its successful treatment of regular graphite (or rather graphene) and diamond crystals. However, intermediate lattice configurations, involving amorphous carbon (mixed sp^2/sp^3 bonding), hydrocarbon molecules and long-range effects, require an even greater consideration of the structural environment when evaluating covalent bond strengths. This need to include chemical reaction processes has led to the the development of many potentials. Marks *et al.* [69] have implemented an Environment Dependent Interaction Potential (EDIP) in the study and formation of amorphous carbon. In a similar effort to include long-range and reactive effects in studying the process of grapitisation Los and Fasolino [18] have developed a Long-Range Bond Order Potential for Carbon (LCBOP). There have also been extensions to Tersoff's original work leading to detailed hydrocarbon bond-order potentials such a Brenner's Reactive Empirical Bond Order (REBO) potential [47], and its most recent incarnation, Stuart's Adaptive Intermolecular REBO (AIREBO) potential [67].

Each of these potentials were developed by their respective authors in studying different, yet related, aspects of carbon and hydro-carbon behavior, all of which would make them suitable for employment in this project. For example, Marks used the EDIP to simulate the growth of amorphous structures which suggests it would be well equipped to mimic the complex bond hybridisation important to the diamond to graphite phase change. Los and Fasolino used their LCBOP in the study of diamond surface reconstructions, something which is especially important in studying surface effects, relevant to graphitisation and bombardment. However, the AIREBO potential has a much wider use within the scientific community. This is jointly due to its historical linage and known ability to describe bond-hybridisation because of its specific parameterisation to small hydrocarbon molecules. Because of this it was decided to use the AIREBO potential in this study.

4.2 The AIREBO Potential

The AIREBO potential [67] is essentially the REBO potential but with two additional terms: a long-range (> 2 Å) Lennard-Jones term and dihedral term (Equation 30). It has been decided to use the AIREBO potential in in the present study. To

successfully model chemical sputtering and structural damage, a sophisticated potential is needed that takes into consideration the chemical processes involved. For carbon and hydrogen this means adequate treatment of bond rotations and carbon sp^2 and sp^3 bonding with a considered intermediate reaction process rather than, for example, simply a weighted average of the two bond strengths.

$$E_{total}^{AIREBO} = \frac{1}{2}\sum_{i}\sum_{j\neq i}\left[E_{ij}^{REBO} + E_{ij}^{LJ} + \sum_{k.\neq i,j}\sum_{l\neq i,j,k} E_{kijl}^{tors}\right] \tag{30}$$

The main component of the AIREBO potential, however, is still the REBO[5] potential, which itself is fundamentally modelled on the original Tersoff potential by taking the following form.

$$E_{ij}^{REBO} = V_{ij}^{R}\left(r_{ij}\right) + b_{ij}V_{ij}^{A}\left(r_{ij}\right) \tag{31}$$

In Equation 31, the total covalent bond energy between two atoms, i and j, is evaluated as the superposition of repulsive, $V_{ij}^{R}\left(r_{ij}\right)$, and attractive, $V_{ij}^{A}\left(r_{ij}\right)$, pair terms with the latter being modulated by the many-body bond-order term, b_{ij}. This bond-order term reflects the chemical environment of the i-j bond and has been the focus of progressive modifications in extending the original Tersoff potential's reactive sensitivity.

$$V_{ij}^{R}\left(r_{ij}\right) = w_{ij}\left(r_{ij}\right)\left(1 + \frac{Q_{ij}}{r_{ij}}\right)A_{ij}e^{-\alpha_{ij}r_{ij}} \tag{32}$$

$$V_{ij}^{A}\left(r_{ij}\right) = -w_{ij}\left(r_{ij}\right)\sum_{n=1}^{3} B_{ij}^{(n)}e^{-\beta_{ij}^{(n)}r_{ij}} \tag{33}$$

In Equations 32 and 33, $w_{ij}\left(r_{ij}\right)$ is a bond-weighting factor that smoothly switches off the potential as inter-atomic separations approach the short-range cut-off (≈ 2 Å). The bond-order term itself is dependent on not only inter-atomic separation, r_{ij}, but also the coordination numbers (of principal and secondary atoms - i, j, k & l), bond angles (including dihedral) and conjugation effects. It is broken down into three parts: the principal contribution is from the covalent π- and σ-bond component, then there is a radical and conjugation term (π_{ij}^{rc}) and a weak dihedral term (π_{ij}^{dh}).

$$b_{ij} = \frac{1}{2}\left[p_{ij}^{\sigma\pi} + p_{ji}^{\sigma\pi}\right] + \pi_{ij}^{rc} + \pi_{ij}^{dh} \tag{34}$$

[5]The following detail of the REBO potential is given here as that described by Stuart *et al.* as the main component of the AIREBO potential [67].

These last two terms are largely derived from tricubic splines dependent on the local coordination numbers of atoms i and j, N_{ij} and N_{ji} respectively, and the local measure of conjugation of the i-j bond, N_{ij}^{conj}.

$$N_{ij} = N_{ij}^{C} + N_{ij}^{H} \tag{35}$$

$$N_{ij}^{C} = \left(\sum_{k \neq i} \delta_{kC} w_{ik} \left(r_{ik} \right) \right) - \delta_{jC} w_{ij} \left(r_{ij} \right) \tag{36}$$

$$\begin{aligned} N_{ij}^{conj} &= 1 + \left[\textstyle\sum_{k \neq i,j} \delta_{kC} w_{ik} \left(r_{ik} \right) S' \left(t_{conj} \left(N_{ki} \right) \right) \right]^2 \\ &\quad + \left[\textstyle\sum_{l \neq i,j} \delta_{lC} w_{jl} \left(r_{jl} \right) S' \left(t_{conj} \left(N_{lj} \right) \right) \right]^2 \end{aligned} \tag{37}$$

The two elements summed over in Equation 37 (over atoms k and l) essentially count the level of bonding surrounding either end of the i-j bond as far as second nearest neighbours (*i.e.* N_{lj} will count all *l-atom*'s nearest neighbours - *n-atoms*).

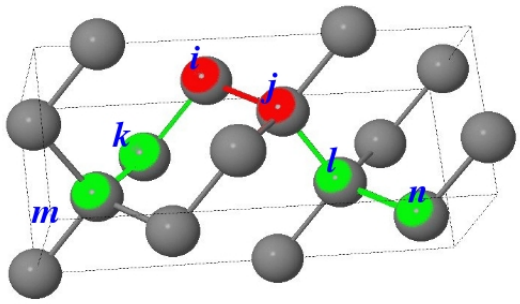

Figure 17: The local environment of the i-j bond is considered to first and second nearest neighbours for the AIREBO potential, whereas only atom k is considered with the Tersoff potential. As atoms are looped over in the various summations all possible '*m-k-i-j-l-n* chains' contribute.

The covalent nature of the bond is described by the $p_{ij}^{\sigma\pi}$ and $p_{ji}^{\sigma\pi}$ terms which depend on bond angles, θ, a two-dimensional coordination number cubic spline term, P, and a hydrogen-sensitive factor, λ.

$$p_{ij}^{\sigma\pi} = \left[1 + \sum_{k \neq i,j} w_{ik} \left(r_{ik} \right) g_i \left(cos\theta_{jik} \right) e^{\lambda_{jik}} + P_{ij} \right]^{-\frac{1}{2}} \tag{38}$$

Equation 38 sums over the secondary atoms k and evaluates the environment of the i-j bond from the perspective of atom i. For $p_{ji}^{\sigma\pi}$, the summation is over atoms l, which correspondingly considers the environment about atom j. Further to this,

tertiary atoms m and n are involved in evaluating the degree of bond conjugation (Equation 37 *i.e.* the nearest neighbours of atoms k and l are also considered, atoms m and n). Figure 17 demonstrates such a possible *m-k-i-j-l-n* chain within a diamond lattice.

The two additional components in the AIREBO potential (Equation 30) are the long range Lennard-Jones term and the torsional term. This Lennard-Jones (LJ) term loops over atoms of a separation < 10 Å and is based around the standard 12-6 potential (Equation 39). This, in turn, is subject to a bond-order term, b^*_{ij}, and a switching function, C_{ij}, turning off inter-atomic forces between chemically connected atoms (i.e. atoms in the same molecule).

$$V^{LJ}_{ij}\left(r_{ij}\right) = 4\epsilon_{ij}\left[\left(\frac{\sigma_{ij}}{r_{ij}}\right)^{12} - \left(\frac{\sigma_{ij}}{r_{ij}}\right)^{6}\right] \tag{39}$$

$$E^{LJ}_{ij} = S\left(r_{ij}\right) S\left(b^*_{ij}\right) C_{ij} V^{LJ}_{ij}\left(r_{ij}\right) + \left[1 - S\left(r_{ij}\right)\right] C_{ij} V^{LJ}_{ij}\left(r_{ij}\right) \tag{40}$$

This LJ bond-order term, b^*_{ij}, is similar to the one shown above (Equation 34), except that if the inter-atomic separation exceeds the maximum parameterised for (about 2 Å), then this upper limit is used in evaluating b^*_{ij} rather than the actual distance of separation.

$$b^*_{ij} = b_{ij}|_{r_{ij}=r^{min}_{ij}} \tag{41}$$

The additional torsional term evaluates the angle between the *i-j-l* and *k-i-j* planes and is parameterised to limit bond rotation for complex hydrocarbons.

In their original 2000 publication, Stuart *et al.* compared their the performance of their AIREBO and the original REBO with experimental results in reproducing structural, mechanical and energetic properties of diamond and graphite (these results are reproduced in Tables 1 and 2). The Lennard-Jones term in the full AIREBO caused a slight contraction of the crystal lattice parameters, however the fit to experiment figures is still good. The diamond bond energy at 298 K is also within 1 kcal/mol of the experimental value and the addition of the Lennard-Jones term allows the AIREBO potential to correctly reproduce the inter-graphite layer separation.

In a 2007 paper Liu and Stuart [70] extended this original work to allow for the Lennard-Jones term to be more adaptive in an effort to better model under-

Property	REBO	AIREBO	Experiment
r_{CC} (Å)	1.544	1.540	1.5445
c_{11} (GPa)	1070	1120(30)	1079(5)
c_{12} (GPa)	120	130(20)	124(5)
c_{44} (GPa)	720	770(20)	578(2)
Bond Energy (kcal/mol)	169.0	171.1	170
Vacancy formation E (eV)	7.2	7.0	7.2

Table 1: Properties of diamond as evaluated by Stuart *et al.* [67]. Bond-length, r_{CC}; elastic constants, c (at 298 K).

Property	REBO	AIREBO	Experiment
r_{CC} (Å)	1.420	1.396	1.415
r_l (Å)	...	3.354	3.354
c_{11} (GPa)	1060	1150	1060(20)
c_{12} (GPa)	150	150	180(20)
c_{13} (GPa)	...	10	15(5)
c_{33} (GPa)	...	40	36.5(1.0)
Vacancy formation E (eV)	7.5	7.7	7.6

Table 2: Properties of graphite as evaluated by Stuart *et al.* [67]. Bond-length, r_{CC}; graphitic plane separation, r_l; elastic constants, c.

saturated hydrocarbons. Testing the sensitivity of the van der Waals interaction they examined the pair correlation function for various hydrocarbon fluids. Their results for liquid methane are reproduced in Figure 18. An extensive study of other species and their reproduced properties, including details of spline table calibrations, can be found in their 2007 paper [70].

Los *et al.* [71] compared the energy barriers of graphitisation for a few potentials in a study of *carbon-onion* formation from nano-diamond crystals. In comparison with DFT calculations they found the REBO potential to overestimate the barrier height which then delayed graphitisation, and underestimated the width of the barrier. Although the AIREBO also overestimated the height of the barrier, the additional long-range term replicated the barrier behavior above 2 Å separation. The Marks' EDIP and the LCBOPII potential of Los *et al.* were a close fit to the DFT results.

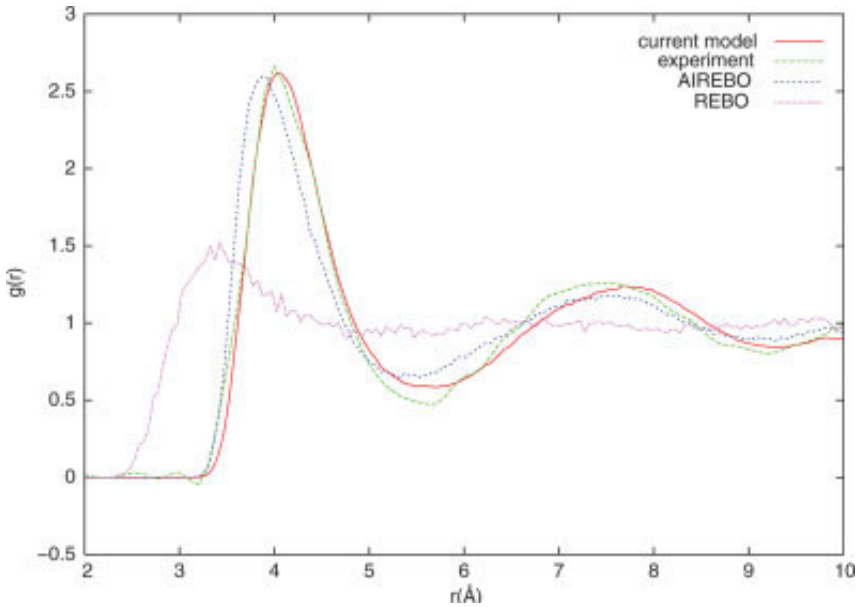

Figure 18: Carbon-carbon pair correlation function g_{CC} for liquid methane at 92 K as evaluated by Liu and Stuart in their 2007 AIREBO potential [70].

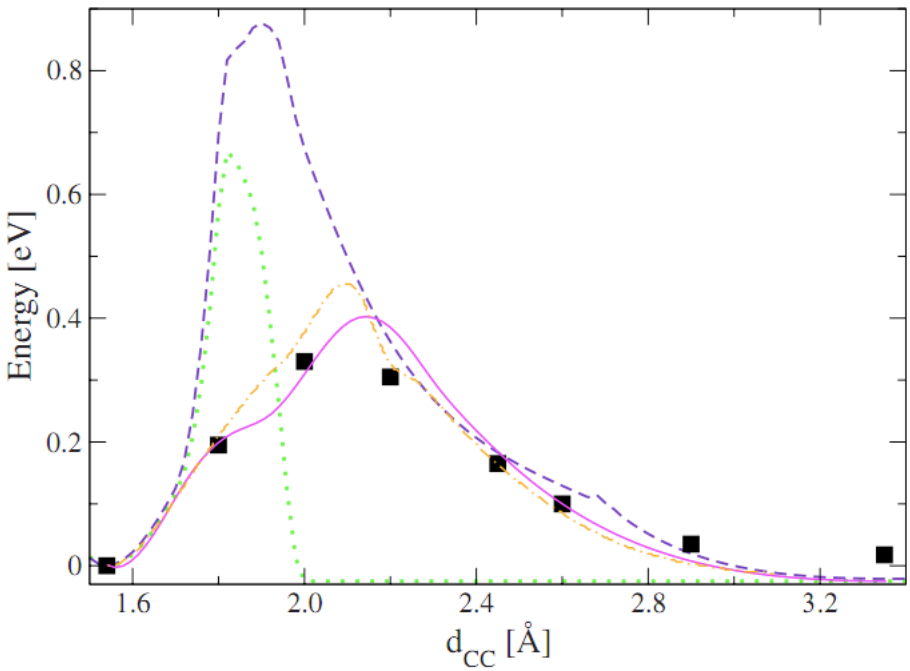

Figure 19: Energy barrier of graphitisation (within nano-diamonds in the formation of carbon-onions) as reproduced by Los *et al.* [71]. The symbols represent DFT results, the dotted line the REBO potential, the dashed line the AIREBO potential, the dashed-dotted line the EDIP potential and the full line the LCBOPII potential.

4.3 DL_POLY run with AIREBO potential

With continued advances in computer processing capabilities and efficient code parallelisation, more detailed and accommodating potentials may be employed with limited extra computational costs. It is hoped that, although the AIREBO potential employed in this study is hugely more complicated than its predecessors, a considered restructuring of the forces up-date algorithm in DL_POLY_3 and faster available processing resources will mean that the added accuracy in simulating carbon bond mixing is worthwhile.

The present version[6] of DL_PLOY_3 [66] does not include the AIREBO potential. It was therefore required to add this option. Due to inherited similarities, it was logical to take structural lead from the current Tersoff subroutines. However, whereas the Tersoff potential only considers secondary atoms j and k, the AIREBO potential sums over all possible i-j-k-l-m-n chains (see above section 4.1.4 detailing the AIREBO potential mathematical form and Figure 17) and has consequences for parallelisation efficiency.

In coding the AIREBO potential I have implemented a number of changes to the current structure that vastly reduce computational time. Specifically, these are an inclusion of a neighbour list construction, identification of regular structures (*i.e.* diamond and graphene lattices) and more than halving the amount of 'halo atoms' needed to simulate continuous boundary conditions. The following is a pseudo-code outline of a simulation run with *airebo_forces* in DL_POLY_3.

Sequence of DL_POLY_3 MD simulation run - AIREBO potential:

1. `System Initialise (read input files, set parameters)`
2. `Main MD loop - over all time steps`
   - `Particle Exchange*`
   - `Halo Construction*`
   - `Forces Evaluation (plus energy, virial and stress tensor)`
   - `Export Halo Forces`†`*`
   - `Position Update Using Forces`[7]

[6] Version 3.09.4, September 2008

[7] The specifics of this general step depend on the integration algorithm used (*i.e.* Velocity Verlet, Leap-Frog, *etc.*). For example, partial timestep integration could happen before and after the forces subroutine

3. `Print Stats and Output Files`

*message passing between parallelised domains

†a new subroutine that I have specifically added for use with AIREBO forces only

---

On initialising DL_POLY_3 in parallel, the workload is divided into domains and shared between each processor (node), this is referred to as domain decomposition (see Figure 20). From the point of initialisation, every node is equivalent (except that only one will print to the output files) and runs independently of the others during the course of the entire simulation. That is except for at regular intervals when the time comes to communicate particle information (via Message Passing Interface (MPI) subroutines). At this point, every node will pass information to its neighbour (say first to its neighbour in the positive x-direction) and then wait to receive from its neighbour in the opposite direction (in this example, the negative x-direction). By this mechanism, each node is therefore roughly in sync with every other throughout the whole simulation. Stages at which this message passing is done are marked with an * in the above simulation run layout and typically straddle either side of the forces evaluation. Running DL_POLY_3 in serial is very much like running in parallel, except that where inter-node communication would otherwise occur, the one node communicates with itself.

Particle Exchange Subroutine - *relocate_particles*

On domain decomposition, the MD cell (globally all the atomic positions) is divided spatially between the number of nodes involved. This is done by dividing the MD cell dimensions and thus its contents, not the other way around. That is to say that an atom's position during the simulation determines on which node it is listed. One important consequence of this is that the MD cell should preferably be of a roughly uniform density and regular shape in order to ensure efficient work-load sharing. However, because during the course of the simulation, unless fixed, atomic positions will change, it is necessary to constantly update relevant domain lists with departures and new arrivals. This is handled by the *relocate_particles* subroutine which calls on *deport_atomic_data* in each of the six cartesian directions. Since atomic positions were last updated, any particles which have thus left one domain's region have all of their associated information stored in a buffer which is then passed in the relevant direction. On receiving similar information from the adjacent domain in the opposite direction, the arriving atomic stats are unpacked and added to this

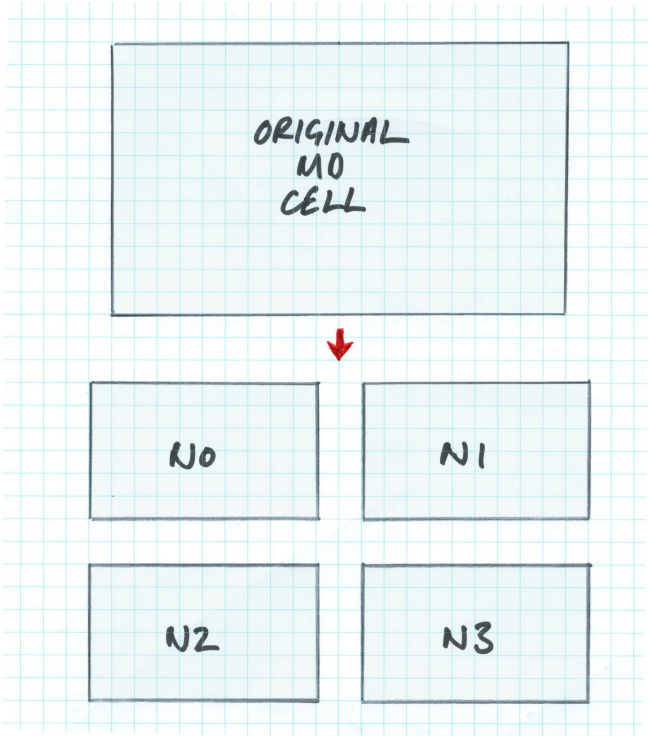

Figure 20: When a job is parallelised, the volume of the original MD cell is split into domains where any atoms within are handled by each node until they happen to move into the neighbouring domain.

domain's remaining atoms.

Halo Construction Subroutine - *set_halo_particles*

When defining atomic positions and overall MD cell dimensions in the initial CONFIG file, boundary conditions are also detailed. It is possible to identify a cell boundary (say the positive x-y plane) and the boundary in the opposite direction (in this case, the negative x-y plane) as being spatially simultaneous. This means that if a particle were to drift continuously in the positive z direction, it would leave the MD cell through the positive x-y plane and reappear by the negative x-y plane. This effectively simulates an infinitely continuous 'bulk'. To create this effect during forces evaluation, the domain edge in one direction is used as the blue-print for creating a list of completely new 'halo' atoms to be added onto the corresponding opposite surface. If continuous boundary conditions are used in all directions, this results in the real atoms on a domain being surrounded by a blanket of halo atoms.

Halo construction is also an important feature of parallelisation since where the initial MD cell is divided, halos are exported between adjacent nodes, replicating

a continuation of simulation space through cleaved surfaces (see Figure 21). Halo export is done in the same manner as detailed above in the *relocate_particles* subroutine, but here calling on the MPI subroutine *export_atomic_data* in each direction.

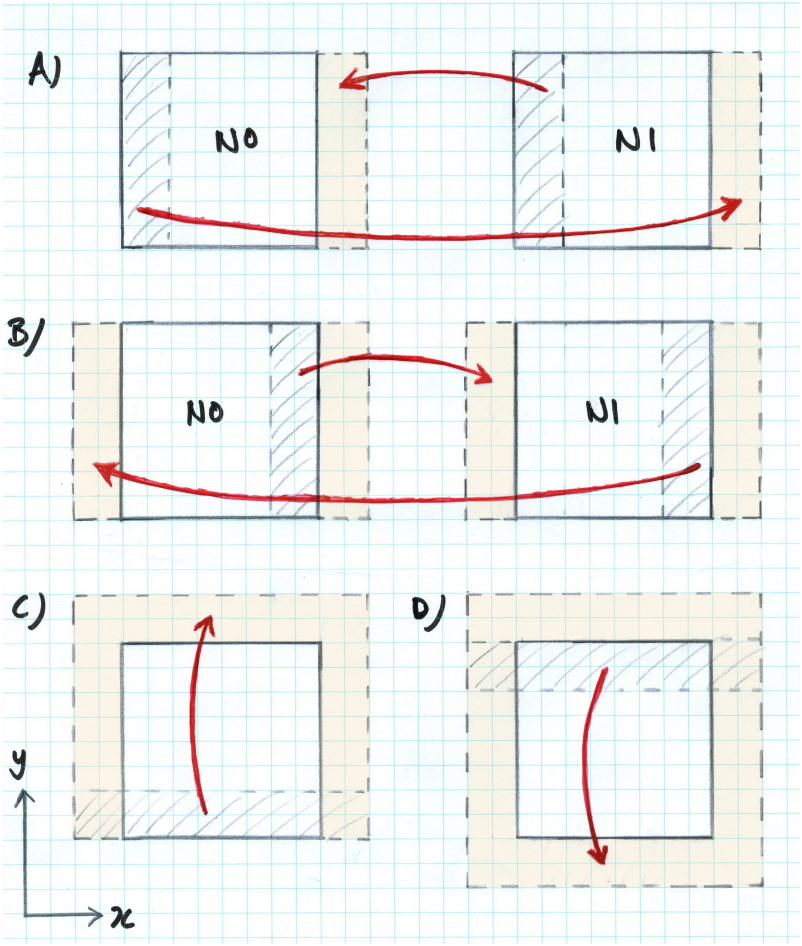

Figure 21: 2D schematic diagram of the halo construction of two parallel nodes (where the whole MD cell has been split in the x-direction between N0 & N1). A node will have a map indicating which neighbouring node to communicate with in each direction (even if that neighbour is itself, as in diagrams C and D). For example, in simulating continuous boundary conditions in all directions and a continuation between the two nodes, N0 will pass atomic information to N1 in the ±x-direction (diagrams A and B). In the y-direction the nodes would communicate with themselves since they both span the whole MD y-dimension (diagrams C and D).

In accommodating the new *airebo_forces* subroutine within DL_POLY_3, modifications were made to the existing MPI subroutines (*relocate_particles* and *set_halo_particles* calling on *deport_atomic_data* and *export_atomic_data* respectively) employed in com-

municating between domains, as well as the introduction of the new subroutine *merge_halo_particles*, which calls on *export_force_data*. The necessity for this is due to the fact that the AIREBO potential considers *m-k-i-j-k-n* chains of adjacent atoms in evaluating the energy of *i-atom*, where the Tersoff potential only required looping over the neighbours *j-i-k*, meaning that a thicker halo is required to simulate the continuous boundary.

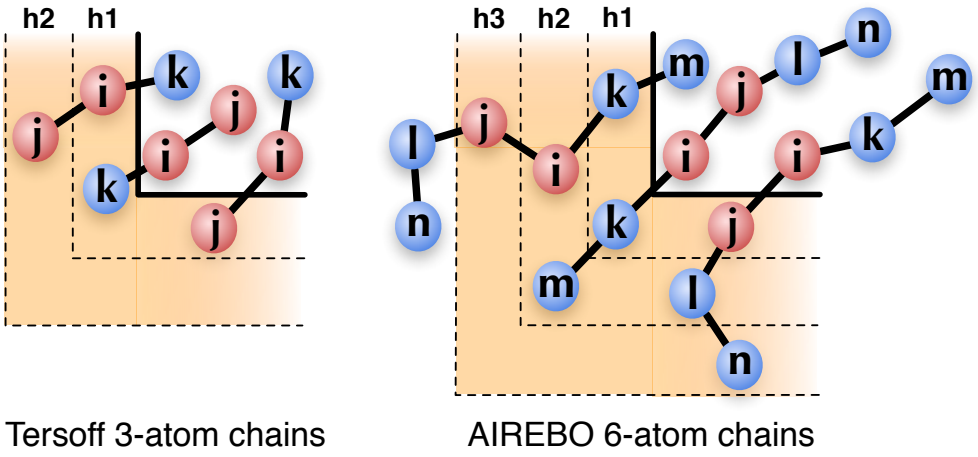

Figure 22: A) For every *i-atom* in the Tersoff potential, atoms j and k are two of its nearest neighbours. If *i-atoms* are confined to the core and inner halo layer (*h1*), then a total halo thickness of $\times 2$ maximum bond length is required. By imposing this constraint, all possible involvement of the core atoms in *j-i-k* chains is seen, and so force information need only kept for core atoms on each domain. B) For the AIREBO potential, if the *i-atom* is confined to the core (real, non-halo atoms), then a halo thickness of $\times 3$ maximum bond length is needed. However, since this does not mean that every involvement of a core atom in every possible chain is seen (*e.g.* where *m-atom* is the only core atom), force information due to its involvement would be lost. For this reason, *i-atoms* are confined to the core and *j-atoms* to the core and first halo layer, and force information is kept for halo atoms, as well as core, and then combined with that of their parent atoms on which ever domain they were copied from.

With the current *tersoff_forces* code a halo of thickness $\times 2$ the maximum bond length is required to simulate continuing boundaries. In this case the primary *i-atom* loop selects atoms only from the domain core and the inner of the two halo layers (see Figure 22). Configuration energy is only accumulated for *i-atoms* that lie within the core. This ensures that every possible *i-j* bond is seen once, even if it crosses a node boundary (into the halo). Similarly, forces are only kept for i, j and k atoms which are within the core. This means that for any atoms within the

halo, that form part of a chain that straddles the boundary, forces are accumulated on the neighbouring node where the same chain is seen by the original atoms that were used as a template for the mentioned halo.

In the *airebo_forces* subroutine, there is a similar primary loop over all *i-atoms* (although for core atoms only) and a secondary loop over *j-atoms* (potentially from first halo layer - *h1*) - *k*,*l*,*m* and *n* loops are nested within this were needed.

Energy is evaluated and accumulated for all *i-atoms*. In evaluating forces, every atom in the *m-k-i-j-k-n* chain experiences a force due to its involvement in the *i-j* bond environment. If forces are to only be kept for core atoms, as with *tersoff_forces*, then, in the extreme case, *i-atoms* would have to be taken from up to the third halo layer (*h3*) allowing for only the *l-n* segment to straddle the core/halo boundary. However, this would require a halo of thickness $\times 5$ the maximum bond length to ensure that all chains are considered. This becomes a problem since that as you increase halo thickness, the number of halo atoms increases proportionally to the radial extension to the power of three (an expanding surface), seriously increasing computational cost. In getting around this, forces are now kept for halo atoms too, and are then communicated back to the original atoms of which they are copied images of. If we also restrict *i-atoms* to the core of the domain, then the maximum halo required is only $\times 3$ the maximum bond length, and every *m-k-i-j-k-n* combination is seen once, either by this domain or the neighbouring one. This is far more acceptable, since in comparison the Tersoff requires a halo thickness of factor $\times 2$. See Figure 22 for examples of the 'straddling-chain' scenarios discussed above.

Export Halo Forces Subroutine - *merge_halo_particles*

This subroutine was added because force information is now being kept for halo atoms where atom chains are unique to this node since halo thickness is kept to a minimum of $\times 3$ the maximum bond length as discussed in the above section (see the chain where only the *m-atom* is within the core in Figure 22 for an example of such chains - in this case *m-atom* is a halo particle on the neighbouring domain, which would have to send back force information to this node obtained from its involvement in this chain). The function of this subroutine is to export this halo force data back to the domain from where the halo atoms were copied from. The halo forces are to be added to those of their corresponding parent core atoms and so all possible *m-k-i-j-k-n* atom chains are covered.

The structure of *merge_halo_particles* is closely modelled on *set_halo_particles*, the substantial differences being the reversal of the order of data export (now z, y then x) and the call on *export_force_data* (also new) rather than *export_atomic_data*. This ensures that every halo atom returns to its original domain core. For this to happen, when halo atoms are initially exported, the index of the original core atom is now also exported so that when the halo atom is returned following force evaluation, it can easily be identified with its parent atom.

AIREBO Forces Subroutine

As with the original *tersoff_forces* code, *i-j* bond properties are evaluated first, energy and virial terms are accumulated and then forces can be evaluated. A schematic sequential outline of the *airebo_forces* subroutine is given below (for a more detailed pseudo-code outline see below in section 4.3.1). The reason there are two secondary *j-atom* loops is that the whole bond-order term, b_{ij}, is required as well as its components in evaluating forces.

Sequence *airebo_forces* call:

1. `Link-Cell Decomposition`
2. `Neighbour List Construction (using Link-Cells)`
3. `i-atom Loop - primary loop (using Neighbour List)`
   - `j-atom Loop - secondary loop`
     - `Bond Order Term -` b_{ij}
     - `Evaluate` **Energy** (*i-j* `Bond`)
   - `j-atom Loop - secondary loop`
     - `Evaluate` *i-j-k-l-m-n* **Forces**, `Virial & Stress`

There are, however, differences in the structure of *airebo_forces* subroutine in comparison with *tersoff_forces*. Other than the need to keep halo force data (as detailed in the above two sections), these differences have to do with link-cell structure, neighbour list construction, allocated array sizes and double-counting. The aim of these improvements is to minimise the time taken in running though *airebo_forces*

at each time-step.

In both *tersoff_forces* and *airebo_forces* the whole node (halo and core) is cut up into a grid of cubic *link-cells* of dimensions marginally larger than the maximum bond cut-off. All atoms are looped over and depending on their positions they are added to the contents lists of these link-cells. Having link-cell dimensions of about the maximum bond cut-off ensures that for an *i-atom* in any given cell, any potential *j-atoms* are known to be either in the same link-cell or in the 26 cells surrounding it. The purpose of this procedure is clear when a loop over all *j-atoms* is needed for every *i-atom*. Without the link-cell allocation the loop would have to cover all other (n-1) atoms on the node. With the link-cells set up, a j-loop over only those 27 link-cells in the immediate vicinity is required.

However, since within the AIREBO potential the local coordination number of any particular atom (the number of nearest neighbours it has) is called upon many times throughout the code, it makes sense to have this information at hand from the beginning. Thus it is worth constructing nearest neighbour lists before bond-order properties are evaluated. Incidentally, this is also favorable when looping over *j-atoms* since with neighbour information the loop only need run over known neighbours rather than potential neighbours. For example, a diamond carbon atom will have only four nearest neighbours. However, since each link-cell may contain four or more atoms, this can easily lead to a j-loop over about 100 potential neighbours. It is obvious that this can unnecessarily become computationally costly. Hence link-cells are now only used in constructing neighbour lists, which are in-turn used in evaluating all other bond properties.

Whilst an atom is having the number of nearest neighbours counted at the start of the code, it also makes sense to evaluate values that depend on atomic separation (such as screening constants) as this is done. These may then be called upon later in the code when needed. A drawback to this would be the need for large and memory intensive multi-dimensional arrays to store all these data. In order to overcome this cost it is assumed that for the majority of the simulation time and volume, forces will be evaluated for near equilibrium regions. In assuming this, we can expect to come across atoms with coordination numbers no greater than four or five (say, $mxnab$=5). So arrays are allocated to this dimension at the start of *airebo_forces* and filled as neighbours are counted. If, however, a local coordination greater than $mxnab$ is encountered, then *airebo_forces* is immediately exited and

re-called for the same time step with *mxnab* re-set. Automatically, *mxnab* is set to one more than the largest number of neighbours encountered at the previous step anyway. This simple method accommodates those rare occasions where local order is rapidly disrupted, (such as a thermal spike during rapid displacement cascades) but also keeps memory costs and time in allocation to a minimum for the majority of the simulation.

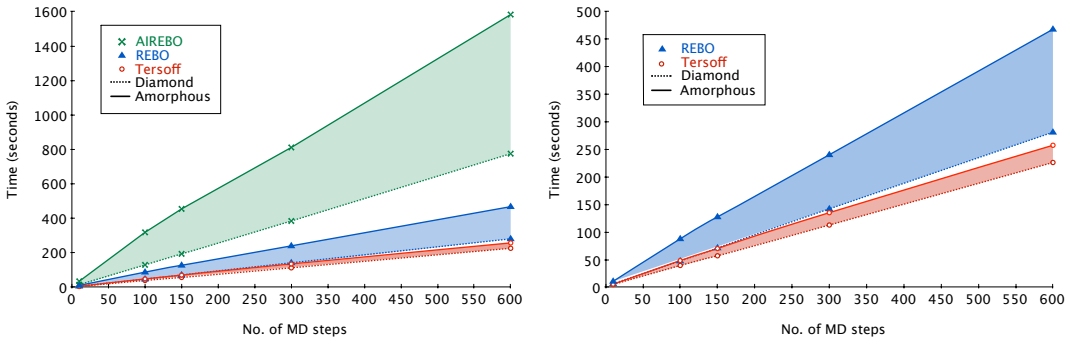

(a) (b)

Figure 23: CPU times for AIREBO, REBO and Tersoff potentials compared for a diamond slab and an amorphous slab. The difference between the AIREBO and the REBO times is dominantly due to the larger Lennard-Jones loops required in the full AIREBO potential. However, the difference between the two carbon structures for the AIREBO and REBO compared to the Tersoff demonstrate the effectiveness of the code optimisation measures for a regular lattice. Image b) is a close up on the REBO and Tersoff times only. The closeness of the REBO and Tersoff diamond runs is due to the use of adaptive array sizes, neighbour lists and lack of double counting, as detailed above, despite the REBO being a greatly more expensive potential.

One final difference between the old *tersoff_forces* subroutine and the new *airbeo_forces* is probably the simplest but most time-saving feature. Due to the symmetric mathematical form of the AIREBO potential, energy and forces for a bond *i*-*j* are identical in size and magnitude to those of the bond *j*-*i*. By removing the factor of one half in Equation 30 and ensuring bonds are looped over only once (by imposing that with respect to indices *i-atom* < *j-atom*), run time is reduced by half.

In direct comparison, dual-node, parallelised[8] DL_POLY_3 runs were performed for the AIREBO, REBO (this REBO, *i.e.* AIREBO less LJ and torsional terms) and the original Tersoff potentials for diamond and amorphous slabs (periodic in x and y directions) of 15552 carbon atoms of volume $(68.6 \times 70.3 \times 18.5)$ Å^3. CPU times

[8]Dual-core processing unit - 2 × GenuineIntel Intel(R) Xeon(R) CPU 5130 @ 2.00 GHz, 4096 KB cache

for a range of MD steps are compared in Figure 23. The advantages due to these optimisation features are clear for the different times of the AIREBO/REBO runs on the two surfaces. In other words, for the ideal diamond structure computational costs were vastly reduced. It is also worth noting that there is not a great deal of difference between the times for the REBO and Tersoff diamond runs. Despite the REBO bond-order term being greatly more complex and requiring many more nested neighbour loops, this is primarily attributed to the use of neighbour lists for the main atom loops and the opportunity to not double count bonds.

Final testing of this execution of the AIREBO potential in DL_POLY_3 was performed by evaluating bond energies for various structures, such as bulk C-C bonds in diamond, graphitic and amorphous structures as well as those of known C-C and C-H bonds within small hydrocarbon molecules such as methane, ethane and ethylene. During the coding of the AIREBO potential into DL_POLY_3 it was also important to test and benchmark the accuracy of the code itself (*i.e.* my coding) as well as the potential. This was done by evaluating configuration energies and atomic forces for various small bulk samples. In order to consider extreme cases, away from the regular lattices (for which much of the bond conjugation and torsional terms in the potential become zero), a cell of hydrogen and carbon atoms was rapidly super-heated and quenched in a random structure (even a physically accurate 'amorphous' structure would not truly be random since there will still be few over coordinated atoms or highly strained bonding). This allowed much of the spline subroutines and lattice-recognition code to be tested. These tests were compared with results using an alternate code for the AIREBO potential provided by the principal author of the potential, Steven J. Stuart. Input parameters for the potential were taken as those in Stuart's original paper [67]. However, some spline parameters used in this project differ very slightly from those quoted in [67]. These were instead taken from Stuart's source code, which had been updated since the publication of the initial paper.

4.3.1 Subroutine Pseudo Code

Pseudo code outlining the *md_vv.f90* call sequence is shown in Figure 24. This is as found in the original DL_POLY_3 source code, similar to that implemented for the Tersoff potential, but with an additional subroutine, *merge_halo_particles.f90*, limiting the need for excessively large halos as detailed above in section 4.3.

A pseudo code outline of AIREBO implimentation in *airebo_forces.f90*, a new

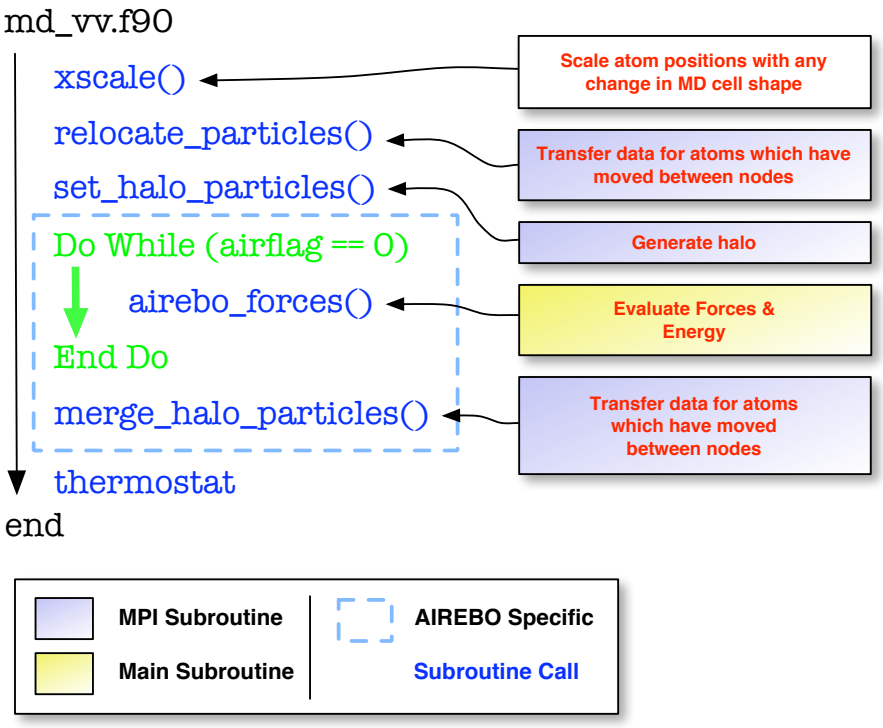

Figure 24: *md_vv.f90* pseudo code outline.

subroutine within DL_POLY_3, is given in Figures 25, 26, 27 and 28. Refer to the DL_POLY_3 user manual (`http://www.cse.scitech.ac.uk/ccg/software/DL_POLY/MANUALS/USRMAN3.09.pdf`) for further details on forces subroutine implimentation. Labels of relevant equations given in brackets correspond to Sutuart *et al.* original AIREBO paper [67].

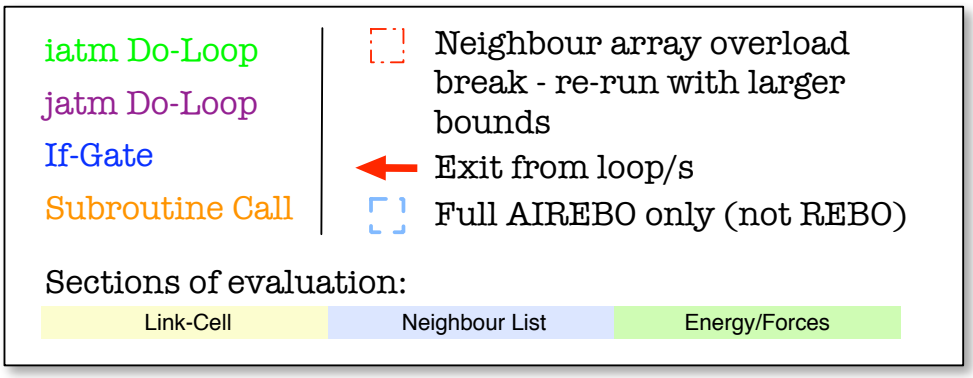

Figure 25: Legend for *airebo_forces.f90* pseudo code outline given in Figures 26, 27 and 28.

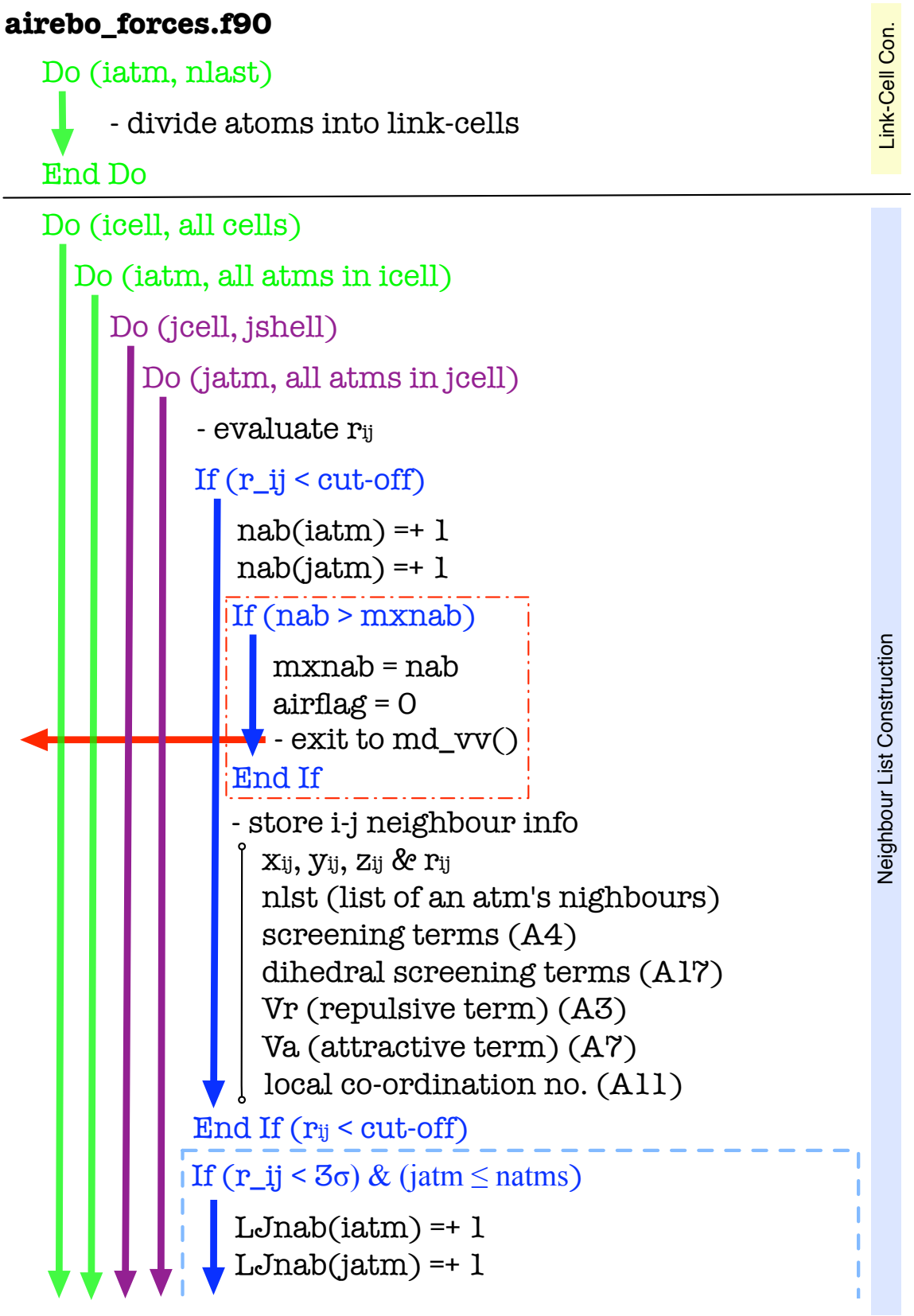

Figure 26: Image 1/3 - *airebo_forces.f90* subroutine pseudo code.

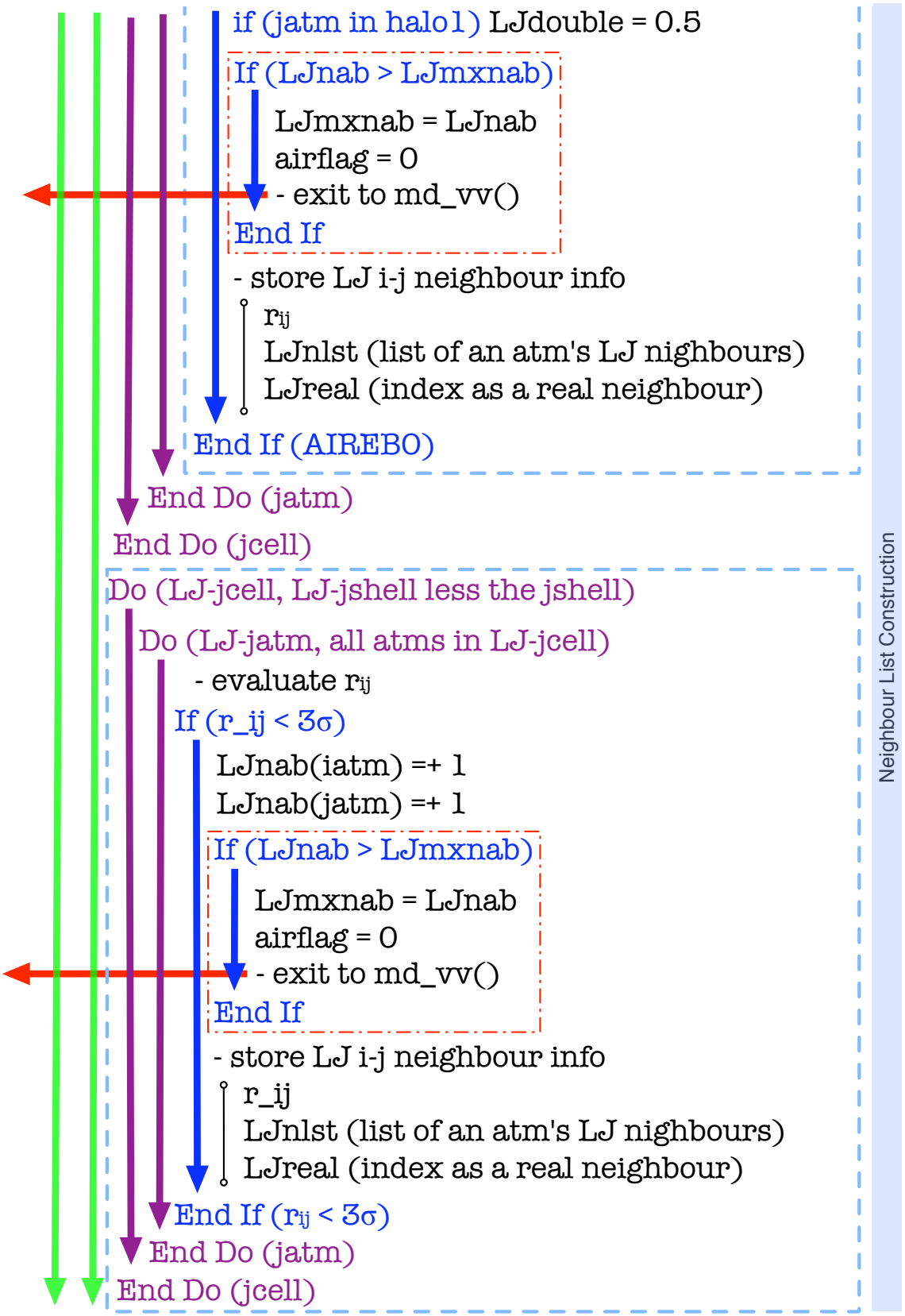

Figure 27: Image 2/3 - *airebo_forces.f90* subroutine pseudo code.

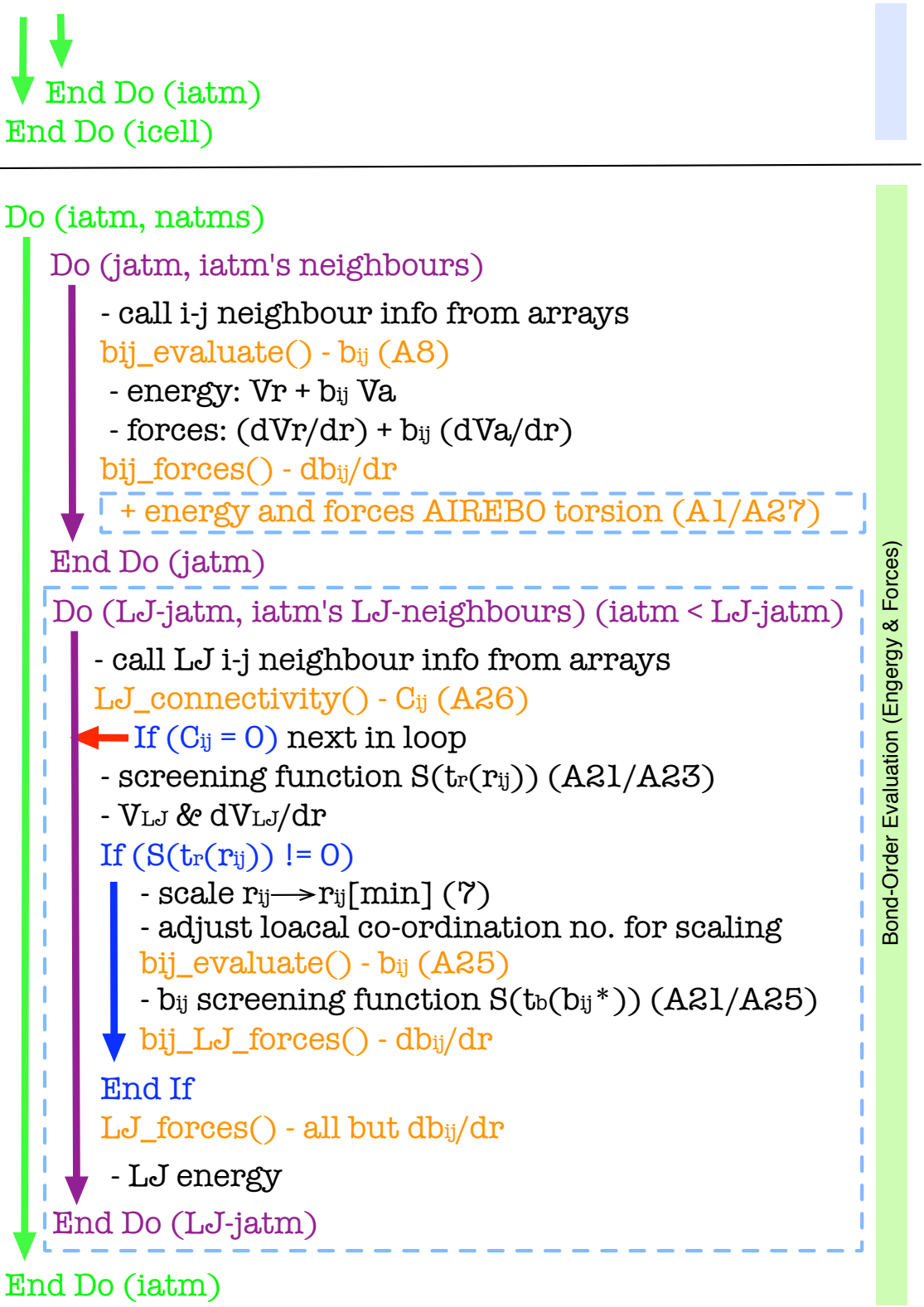

Figure 28: Image 3/3 - *airebo_forces.f90* subroutine pseudo code.

5 Thermally Induced Graphitisation

Of all carbon structures, diamond offers the most impressive thermal properties. This is down to its strong tetrahedral sp^3 bonding. However, one of the main criticisms of diamond as a plasma facing material is the fact that it is only a metastable phase and can graphitise or amorphise given enough thermal energy. This is one reason why only graphite and amorphous carbon based materials are currently used in tokamaks.

Understanding the mechanism behind this phase change therefore has great importance for diamond's candidacy as a plasma facing material. It will also bear on following chapters in this thesis which explore the dependence of temperature on performance considerations such as tritium retention and sputter yield.

5.1 Method

Three planes of the diamond crystal lattice were separately exposed as surfaces and then terminated with hydrogen in varying coverages in a comparative study in resistance to graphitisation on heating.

These surfaces were the diamond (100), (110) and (111) conventional unit cell planes. If the origin is taken to be at the centre of a cube, each of these planes has an equivalent plane in the opposite direction planes respectively (for example, see the (111) plane and its opposite in Figure 29) - the $(\bar{1}00)$, $(\bar{1}\bar{1}0)$ and $(\bar{1}\bar{1}\bar{1})$. For each, permutations of each index reveals similar planes. For example, with diamond the (100) plane, the (010) and (001) planes are similar in structure yet perpendicular to the (100), and each has its equal in the opposite direction. Where for the (100) case there are in total three similar yet inequivalent planes, for the (110) and (111) planes there are six and four similar surfaces respectively. Since it is the (111) diamond layers which preferentially become graphene layers, it is worth noting that there are four possible orientations for this to occur within any sample.

Three diamond slabs of approximately 16000 atoms and of similar dimensions were orientated so that each one of the chosen surface structures were parallel to the x-y plane, that is perpendicular to the z-axis. These then served as the templates for further modifications. For each orientation a sample was created where the slab was periodic in all directions, simulating crystal bulk. Similarly, a surface was created by changing this to periodic in the x and y directions only, and so exposing as a surface either the (100), (110) or the (111) conventional diamond planes. These may be considered as cleaved surfaces, cut from an ideal bulk, and in this respect they are ideal and unrelaxed. For each orientation, one of these surfaces was left 'clean' and

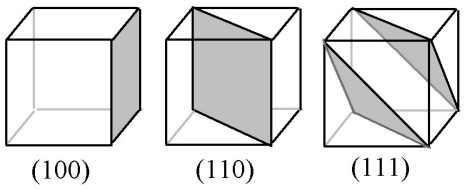

Figure 29: Cubes showing the (100), (110) and (111) Miller planes (the $(\bar{1}\bar{1}\bar{1})$ is also shown, taking the centre of the cube as the origin). These planes through the diamond conventional unit cell form the x-y surfaces of the three basic samples heated in this section.

one was terminated with hydrogen; a single hydrogen atom was added above every surface carbon for every bond severed in creating the surface, and so passivating all dangling bonds. For the (111) surface, slabs with degrees of hydrogenation were also made, where surfaces were terminated with 50% and 25% random hydrogen coverage and another was half covered with a strip of hydrogen leaving half the slab exposed, totaling 12 samples in all.

In preparation, these 12 samples were each heated up from 10 K to 300 K over 10 temperature increments, each lasting 3 ps simulation time (3000 0.001 ps time-steps) - 9 Kps^{-1}. This was done so as to relax the sample, allowing velocities to eventually come into equilibrium at room temperature. The thermostat used was an *npt* Nosé-Hoover thermostat which maintains pressure and temperature as constant, allowing for the system volume to expand or contract and so adjusting bond-lengths to energetically favorable separations as described by the current state of the AIREBO potential.

Following relaxation, the samples were then gradually heated up from 300 K to anywhere between 2000 K and 4000 K, depending on resistance to graphitisation, at regular steps of 5 ps and temperature increments of 34 K[9]. This heat-up was done using an *nvt* thermostat, maintaining the relaxed slab dimensions (in the periodic directions only). For slabs (*i.e.* not bulks), the bottom atoms were frozen to a depth of approximately 25%-30% total slab thickness (specifics given in Table 3). Marked as 'frozen', these atoms automatically have zero velocity throughout the MD run. This was done so as to simulate a continuation into a bulk in the -z direction, meaning that only the +z surface was truly exposed as a surface. Subsequently,

[9]Each of these temperature-steps ran for 5000 time-steps of 0.001 ps and represents a separate initiation of DL_POLY_3 - taking just under 10 minutes cpu time to run. Each simulation was a restart of the previous, but with a slightly higher temperature.

even if all of the free atoms were to graphitise due to heating, these fixed atoms would remain in the relaxed diamond configuration.

Sample	Dimensions	C Atoms	Frozen	Surface Atoms
(100)	$71.6 \times 71.6 \times 17.9$ Å^3	16000	4000 (25.00%)	800 (5.00%)
(110)	$60.1 \times 77.9 \times 20.0$ Å^3	16896	5280 (31.25%)	1056 (6.25%)
(111)	$68.1 \times 69.8 \times 18.5$ Å^3	15552	4320 (27.78%)	864 (5.56%)

Table 3: Sample details. 'Frozen' atoms are along the -z surface of the slab form and are fixed so as to simulate bulk continuation. 'Surface atoms' are those on the +z surface of a slab who have had bonds severed in the process of creating a slab.

5.2 Surface Structure

A preliminary estimate of surface energies may be taken by considering the number of bonds broken in cleaving a slab from the bulk (*i.e.* removing periodic boundary conditions in the z direction). The relaxed C-C bond energy within bulk diamond is here is 3.68 eV, as evaluated with this AIREBO code at an average bond length ∼1.54 Å. These surface energy estimates (given in Table 4) are rather crude in that not only do they not allow for surface reconstruction, but they also assume that severed surface bonds behave as if they were still within the bulk medium. Inevitably, in creating the surface, bond hybridisation will vary from that of an ideal diamond sp^3.

Sample	Surface Area Å(m^2)	Broken Bonds	ΔEnergy eV	Surface Energy Jm^{-2} (eVÅ^{-2})
(100)	5133.52 (5.13×10^{-23})	1600†	5888.0	9.19 (0.57)
(110)	4677.51 (4.68×10^{-23})	1056	3886.1	6.66 (0.42)
(111)	4752.73 (4.75×10^{-23})	864	3179.5	5.36 (0.33)

Table 4: Surface energies of unrelaxed surfaces as cleaved from the ideal bulk based on bond-breaking alone (*i.e.* not talking into account the disruption to the continuous crystal this causes). The lowest surface energy is for the (111) surface.
† The (100) surface atoms have each had two bonds severed, where as for the (110) and (111), only one bond per surface atom was cut in cleaving the surface.

As outlined above, these surfaces were heated to 300 K over 30 ps under an *npt* thermostat, allowing for bond-length relaxation and surface reconstruction. For all orientations the x-y dimensions of the slabs did not vary much during this time. Bond lengths and energies between atoms generally below the first couple of surface layers remained pretty much as was found within bulk diamond (*i.e.* at about 1.54

Å and 3.68 eV). Total configuration energy for each slab was evaluated before and after this heating process, representing un-relaxed (ideal) and relaxed structures respectively. The difference between these energies and those of the bulk for the same samples under the same conditions is in effect the energy required to create two surfaces (±z sides of the slab). Half of this is taken as the surface energy and is given here alongside other reported values in Table 5.

		(100)	(110)	(111)
Unrelaxed (ideal)	*a) This study*	10.96	3.73	5.29
	b) DFT	9.72	7.48	8.12
	c) Brenner	6.64	4.03	2.77
	d) Tersoff	7.57	4.95	4.04
Relaxed	*a) This study*	10.44	2.37	4.98
	b) DFT	9.40	5.93	6.43
	c) Brenner	5.03	2.02	1.39
	d) Tersoff	6.16	3.26	2.66

Table 5: Surface energies (Jm^{-2}) for the three exposed surfaces before and after allowed relaxation. Results a) are from the present study. Results b) were evaluated by Stekolnikov *et al.* in 2002 using density functional theory and the VASP code [72]. Results c) and d) were evaluated using molecular dynamics in 1991 by Halicioglu *et al.* and compare the Tersoff and Brenner potentials [73]. In each set of data, the lowest surface energy is shaded grey.

Generally, surface energies evaluated using a potential (Table 5) are lower than those estimated by simply counting broken bonds (Table 4). This is true too of the unrelaxed case, for although no structural repositioning of atoms has occurred, the extent to which the the local environment at the surface differs from the bulk has affected nearby bond strengths.

(100) Surface

For the (100) slab, each surface atom is only bonded to two atoms below which themselves are sp^3 bonded in the diamond structure and are thus unable to reciprocate in forming double-bonds with the surface atoms. The result is that the only real difference in bonding strength was for those bonds with atoms immediately at the surface where bond energies dropped to about 3.33 eV from the bulk value of 3.68 eV. For this reason, little difference is seen between the relaxed and unrelaxed surface energies (a feature also observed by Stekolinkov *et al.* [72] in their DFT calculations). The weakening of these bonds results in an even greater energy difference between surface and bulk than estimated due to bond breaking alone, and so,

unique to the (100) case, we see a larger surface energy than predicted in Table 4. As with the MD simulations run by Halicioglu *et al.* [73], little surface restructuring was observed. However, the DFT calculations exposed a possible dimerisation of adjacent (100) surface atoms (which are otherwise only bound to two sp^3 carbons below the surface). This (2×1) reconstruction offers a much lower surface energy of about 5.71 Jm^{-2}, lower than that of the (110) surface from the same study. Russell *et al.* [74] experimentally found the (100)(2×1) dimerisation bond to exhibit properties similar to Ċ-Ċ bi-radicals (with a dangling bond at each surface carbon) rather than the C=C double bond found in alkenes.

(110) Surface

Each surface atom on the (110) slab has had one bond severed in creating the surface, and is bonded to two other surface atoms and one sp^3 carbon below the surface. It is the strong bond mixing (4.48 eV at an interatomic of about 1.45 Å) between these adjacent three coordinated surface carbon atoms that drastically reduces the (110) surface energy. So much so, that contrary the estimate on bond-breaking alone, the (110) slab termination is found here to be the lowest energy surface. Although energy values differ greatly, the DFT calculations performed by Stekolinkov *et al.* also found the (110) to be the lowest (1×1) energy surface - a feature expressed by neither the Tersoff nor the Brenner potentials.

(111) Surface

As with the (110) surface, the (111) surface atoms have each had one bond broken in creating the slab. However, each of these is bonded to three sp^3 carbons below the surface (each one of which is bound to three surface atoms and only one other sp^3 atom, directly below itself). The surface layer and this first layer of sp^3 carbons beneath it form the first (111) 'bilayer' - the two component layers of this bilayer are not separated by much in the z-direction and contain the hexagonal structure which preferentially forms the graphene planes on graphitisation.

Since these surface atoms are bonded to otherwise diamond carbons (and not other non sp^3 bonded atoms), there is not a large energy difference on relaxation. However, this is for the conventional (1×1) structure. The surface energy may be reduced by allowing some of the surface atoms to break their bond with the sp^3 carbon below. Although a bond is broken, there are now strongly bonded adjacent sp^2 atoms at the surface. In their DFT calculations, Stekolinkov *et al.* found this (2×1) surface reconstruction to have a surface energy as low as 4.06 Jm^{-2}. This

behavior at the surface was only really observed in the present study when the sample temperature was raised to above 600 K. Although surface energy is indeed reduced, this process of forming sp^2 regions at the surface and breaking bonds with the below bilayer serves to propagate the process of graphitisation, which inevitably leads to a lower configuration energy overall where sp^2 C-C bonding in graphite is of about -5 eV.

Hydrogen Terminated Surfaces

Surface H coverage		(100)	(110)	(111)
100%	*a) AIREBO*		-4.60	-5.44
	b) DFT	-9.11	-9.99	-8.19
50%	*a) AIREBO*	-3.94*		0.17
50% (strip)	*a) AIREBO*			0.69
25%	*a) AIREBO*			2.06

Table 6: Passivating surface dangling bonds with hydrogen reduces surface energy (Jm^{-2}). The (111) surface was terminated with a range of levels of random coverage and also a solid strip covering 50% of the surface.
* One hydrogen for every (100) surface atom (monohydride), for which two bonds each have been broken in creating the surface. Thus classified here as only 50% coverage, although perhaps comparable with the 100% termination for the other samples.

Terminating the sample surfaces with hydrogen passivates otherwise dangling bonds. The effect of this is to somewhat restore lattice structure near the surface to that of the bulk material, and carbon-hydrogen bonds are stronger than carbon-carbon bonds, so for the 100% coverages we have a negative surface energy (Table 6).

The (100) surface was not so easily 100% terminated. If the clean surface carbons do not dimerise in an effort to reduce surface energy, they have two dangling bonds each. Thus 50% coverage would relate to a monohydride phase where each surface carbon atom has only one hydrogen, and 100% coverage results in a dihydride phase. It has been argued [75] that this dihydride phase is highly strained due to H-H repulsion and difficult to form. In the present study it was found that at room temperature a dihydride (100) slab quickly lost molecular hydrogen from the surface leaving a mixture of single and double hydrogen terminated carbon atoms at the surface. The monohydride surface however was stable and of a low surface energy considering the number of bonds broken in creating the clean surface from the bulk.

A Note on Images

In the following images of the carbon slabs in this section, the only elements present are hydrogen and carbon. Hydrogen is represented as small white spheres. Carbon, however, is colour-coded depending on the number of nearest neighbours each atom has.

No. Nabs.	Bond	Colour
< 2		Red
2		Light Purple
3	sp^2	Grey
4	sp^3	Beige
> 4		Dark Purple

5.3 Heating

(111) Surface

The lowest energy surface by dangling bond density, the (111) planes readily become graphene sheets on heating. All the surface sp^2 atoms form half of the top bilayer. For this reason, graphitisation nucleates at, and propagates from, the surface. As seen in Table 7, a clean slab enters a period of phase transition at about 500 K, as opposed to 2500 K for a bulk sample. Passivating the surface dangling bonds with hydrogen has been shown to go some way to simulating bulk continuation [76] with regards to the surface carbon structure, but also to some degree mimicking bulk graphitisation behavior as seen here.

Sample	Temp (K)
Bulk	2500
H-terminated 100%	2000
H-terminated 50% (random)	1000
H-terminated 50% (strip)	500
H-terminated 25%	500
Clean	500

Table 7: Temperature at which the (111) diamond structure begins to re-order (beginning of graphitisation). Although bonds begin to break at the clean surface at about 500 K, the top bilayer does not really begin become a graphene plane until about 700 K. With the 50% strip, only the clean half graphitises at such a low temperature

Clean Slab & Bulk

As mentioned, all the dangling bonds along the (111) surface correspond to half the atoms in the top bilayer. These in effect have already undergone the sp^3 to sp^2 change associated with graphitisation. On heating to above 500 K, the remaining sp^3 atoms at the surface easily break their inter-bilayer bond with the bilayer below and slowly the surface forms a clean graphene sheet and peels away (Figure 31). In addition, since the sheet is also periodic in the x-y plane, there are no dangling bonds at any edge needing satisfying, and so with no contortion can remain relatively flat. This layer-by-layer graphitisation of the clean surface can be seen in the configuration energy profile in Figure 30.

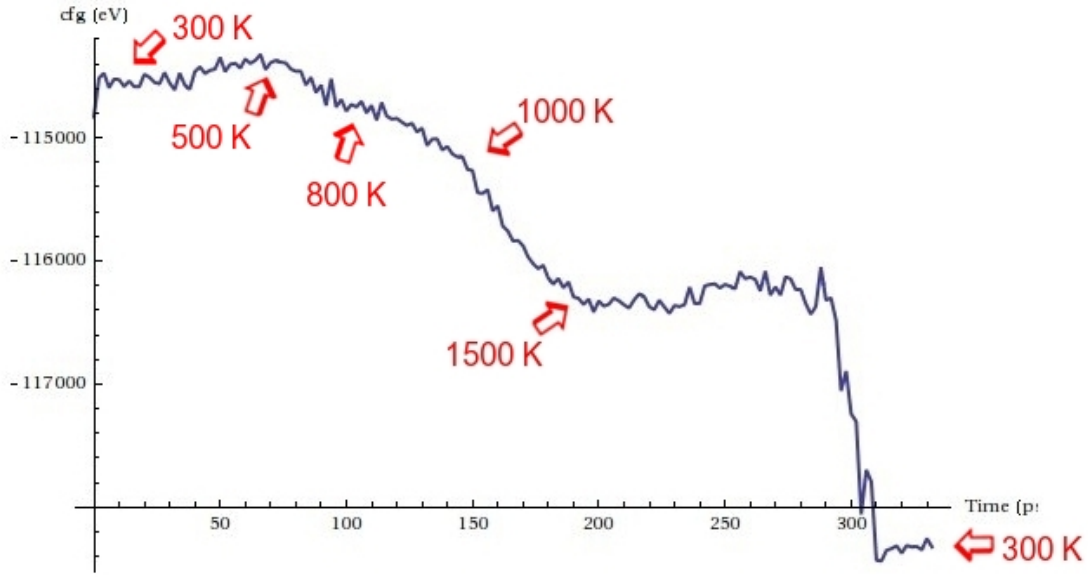

Figure 30: Plot of lattice energy (eV) with time (ps) for heating of the **clean (111) slab** - little heating (500 K, until which there is a gradual increase in configuration energy) is required before the atoms along the underside of the surface bilayer begin to break bonds with the upper atoms of the one below forming regions of adjacent sp^2 atoms on the surface. Although bonds are broken, stronger ones are formed and so the overall configuration energy is reduced. This lowers the surface energy (in comparison to the diamond bulk) but nucleates layer-by-layer graphitisation. The first bilayer begins to peel away at about 800 K, and this continues until just over 1500 K at about 200 ps, when the final un-frozen layer has finished separating. On cooling back to 300 K (>290 ps) the level to which the configuration energy has reduced in graphitising is apparent.

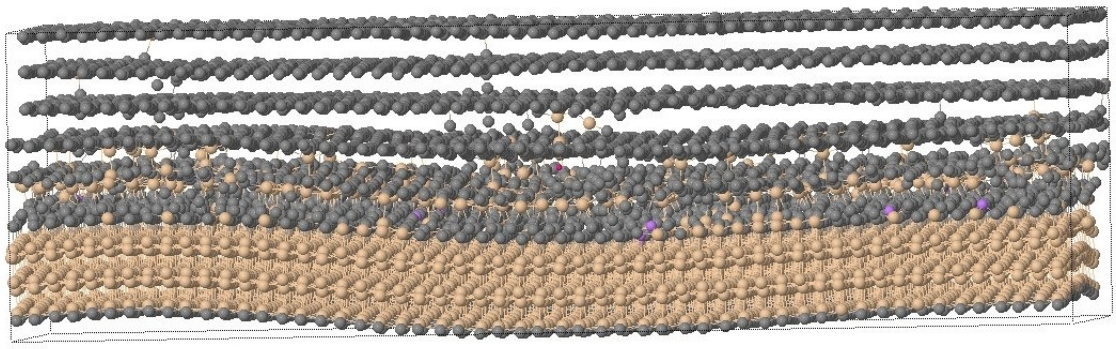

Figure 31: The (111) slab towards the end of the graphitisation process. The top four (111) bilayers have completely 'peeled' away into neat graphene sheets (the bottom two and a half form the frozen region).

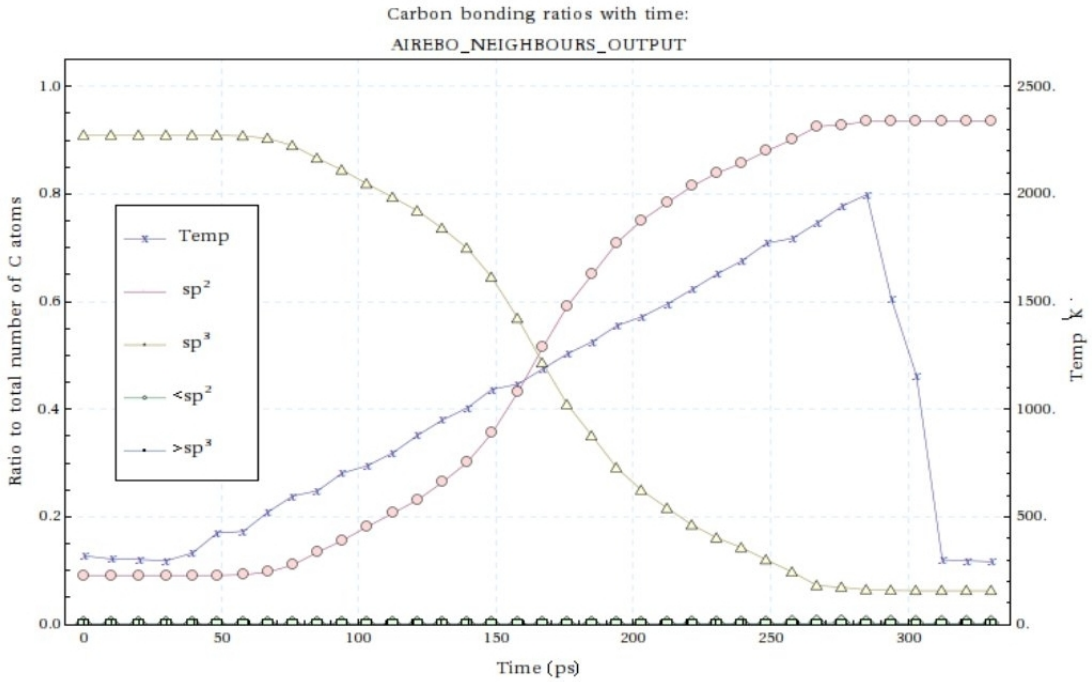

Figure 32: Bonding ratios (sp^2/sp^3) of the **clean (111) slab** - as the sample is heated, there is a smooth decrease in the level of sp^3 bonded atoms which is matched by an equal and opposite trend in the sp^2 bonding. The initial 10% sp^2 bonding is due to the $\pm$z surfaces, and the final 8% sp^3 is due to the frozen -z carbons.

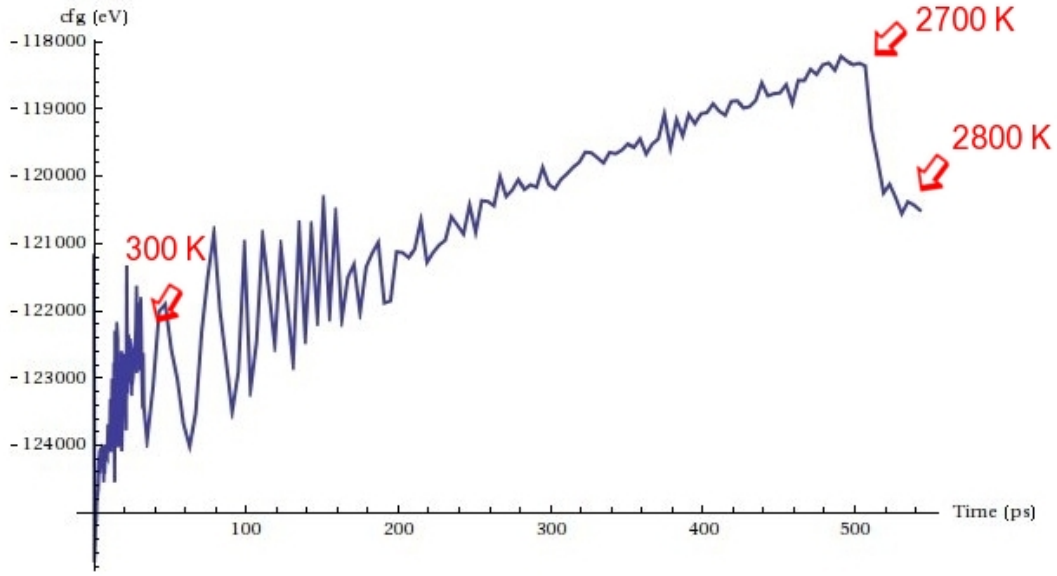

Figure 33: Plot of lattice energy (eV) with time (ps) for heating of the **bulk (111) sample** - The diamond structure is maintained during most of the heating process with no obvious point for graphitisation to nucleate from. As the sample is heated the configuration energy becomes less negative due to thermal excitation. Between 2700 K and 2800 K (490-525 ps) the structure undergoes rapid phase change from an all sp^3 diamond bonded one to a sp^2 graphitic one. On cooling back to 300 K (not shown) the total configuration energy has been reduced to about -125000 eV (8.03 eV per atom or 5.36 eV per sp^2 bond).

Degrees of Surface Hydrogenation

Passivating an otherwise clean surface with hydrogen goes some way to replicating a continuation into a bulk medium as far as the structure of the surface carbon atoms are concerned, and duly increases the temperature of graphitisation to something comparable with a bulk sample rather than a surface. However, because on heating the surface carbons in the presence of hydrogen cannot form clean sp^2 bonds with their carbon neighbours there is a certain degree of disorder towards the surface. In addition, in the (111) surface case, the carbon-hydrogen bonds exist in an orientation were otherwise bond-breaking would occur in graphitisation (perpendicular to the (111) plane). Because of this, the hydrogenated (111) surface resisted graphitisation until approximately 2000 K (in comparison with the clean slab at 500 K). Somewhat a mixture of features from the bulk and clean slab samples, graphitisation did not necessarily begin at the surface as with the clean slab, nor did it easily propagate uniformly as with the bulk which resulted in many domains of graphite orientated along different (111) directions.

Simulations for surfaces randomly covered covered with hydrogen for 25%, 50% and 100% dangling-bond saturation were heated and displayed almost proportional suppression of graphitisation to their level of saturation, which eventually occurred at 500 K, 1000 K and 2000 K respectively. While termination with hydrogen may be energetically favorable for the surface, it also hinders the propagation of graphitisation from the surface down into the bulk. For the lightly terminated case (25%) this results in not completely separated graphene-like layers and a high degree of surface disorder. Instead of a layer-by-layer peel-away mechanism, surface regions where there is a relative lack of hydrogen act as a nucleus for graphitisation which propagates perpendicular to the surface. These pyramidal islands of sp^2 bonds expand and where possible merge, thus in some way under-cutting the hydrogen terminated regions. This happens to a lesser extent for the 50% terminated case and the final sample is left with interconnected and irregular graphene 'layers' with some sp^3 left throughout.

When analysing the configuration energy profiles with time, as seen above in the (111) slab, there is generally a period of steady energy increase with temperature before the structure changes. As seen in Figure 35, with the onset of graphitisation, the configuration energy smoothly drops, but due to the subsequent surface disorder it rapidly fluctuates and greatly increases. Because of this, although the underlying majority of the sample may have cleanly graphitised, the surface disorder clouds the

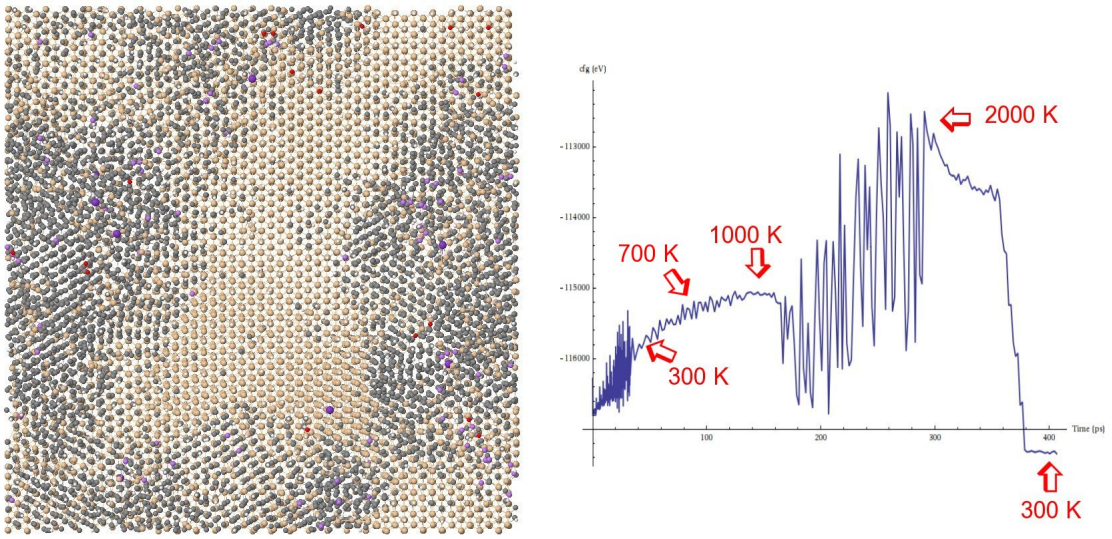

Figure 34: Random 50% hydrogen terminated (111) slab - Left: At 1000 K, seen from above. Domains of graphitisation (orientated in one of the four (111) directions) can be seen here to begin merging - this is just before the surface really started to become disordered. Right: The period of graphitisation (beneath the surface) begins at about 700 K (100 ps) and reduces the rate of increase of configuration energy with temperature before the surface disorder drastically increases at 1000 K (160 ps). Graphitisation is complete after about 2000 K and on cooling back to 300 K there is a clear energy difference between the two ordered structures, despite the surface disorder.

energy profile and generally reports a higher configuration energy than what was probably expected.

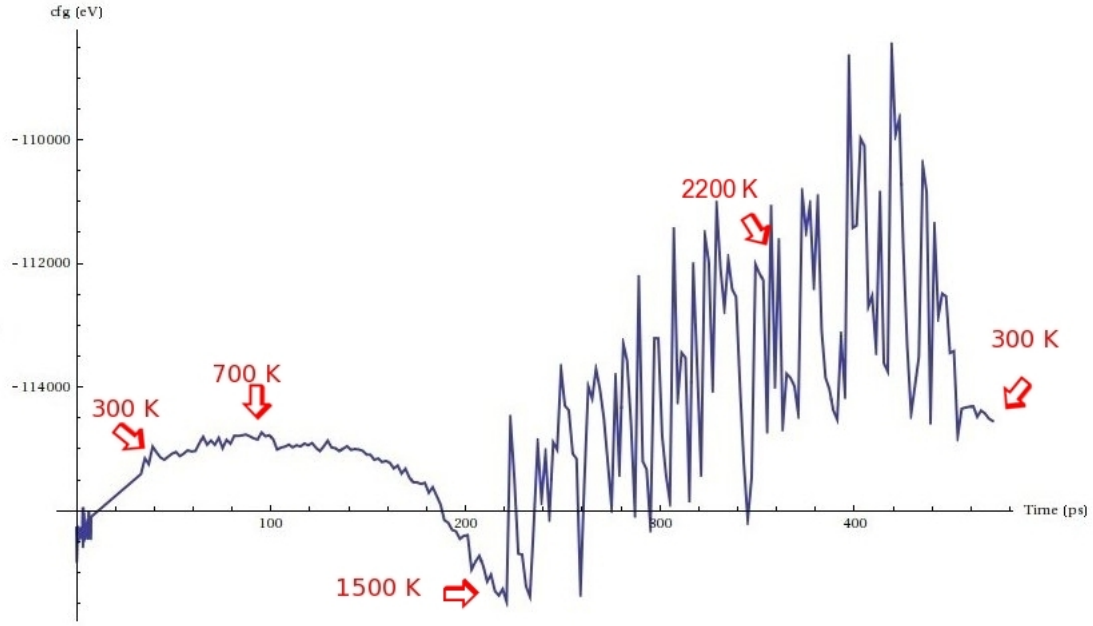

Figure 35: For the 25% hydrogen terminated (111) sample, the majority of the surface carbon atoms are sp^2 bonded and on heating encourage neighbouring atoms on the underside of the top bilayer to break bonds with those of the bilayer below in an effort to reduce configuration energy. This is as with the clean surface and is here represented by the smooth decrease in energy between 700 K and 1500 K (100-220 ps). After this period the surface becomes disordered as the hydrogen prevents convenient graphene layers forming. However, the spread of sp^2 bond forming (which stops after about 2200 K) was initiated at the surface and has resulted in sub-surface graphene layers orientated parallel to the surface. Despite this, disorder dominates at the surface over any crystal structure which cancels out any gain in configuration energy due to graphitisation of sub-surface layers. This is why on cooling back to 300 K there is no substantial gain in energy.

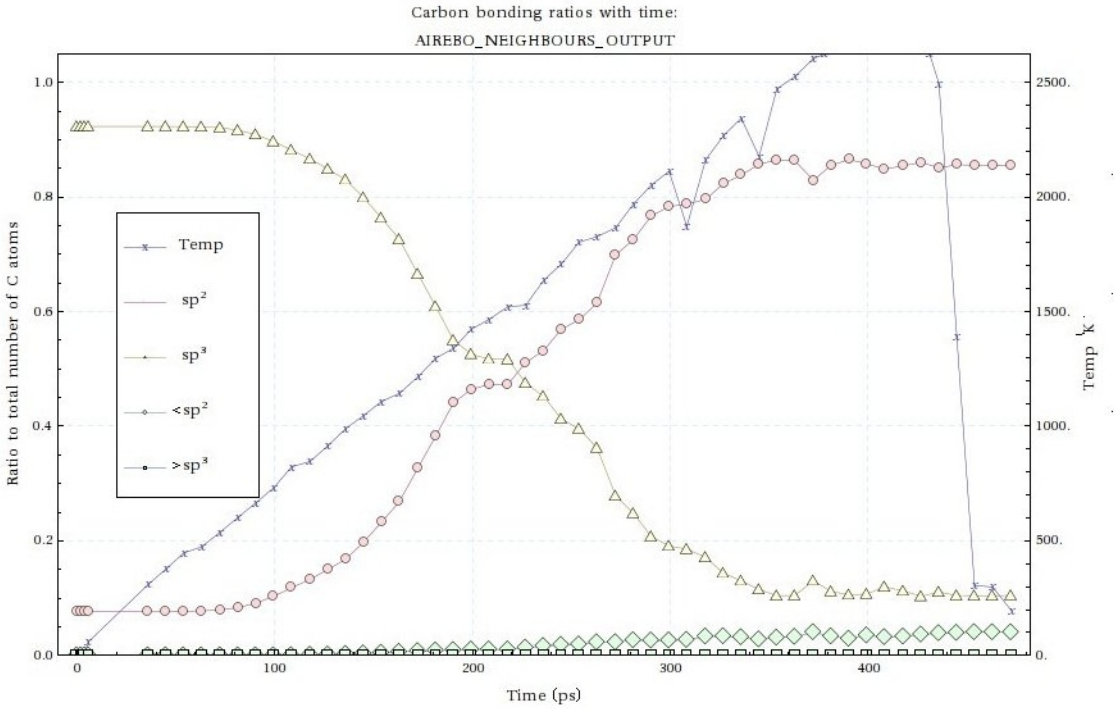

Figure 36: Bonding ratios (sp^2/sp^3) of the **25% random hydrogen terminated (111) slab** - Although there is a significant level of sp^2 bonding in the final sample, these do not form ordered graphene sheets.

A surface with a strip of hydrogen termination which covers roughly half the surface was also heated. As one would expect, the exposed clean half underwent graphitisation as did the fully clean sample at about 500 K (Figure 37). At about 2000 K the section under the hydrogen strip began to undergo a phase change and the surface began to disorder. Where these graphene layers from the clean half met the bulk diamond underneath the hydrogen strip, graphitisation was encouraged, but rather than completely undercut the hydrogen surface, these graphene layers in the x-y plane bonded with (111) planes which intersected the frozen diamond thus resulting in curved graphene layers. Although the surface disorder of the hydrogen-terminated surface disrupted clean graphitisation, exposure to the clean graphene encouraged a small degree of order (Figure 38).

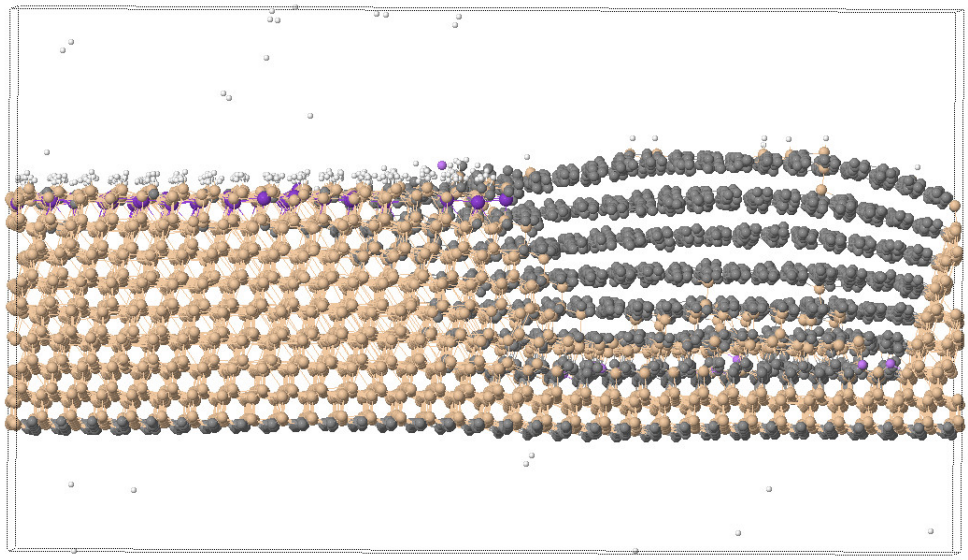

Figure 37: 50% strip hydrogen terminated (111) slab, 1500 K - The left half of the sample surface is terminated with hydrogen and resists graphitisation to a much higher temperature than the clean surface which has already formed graphitic layers parallel to the surface. Above this temperature, the graphitisation begins to undercut the hydrogen terminated surface and sp^2 bond forming propagates.

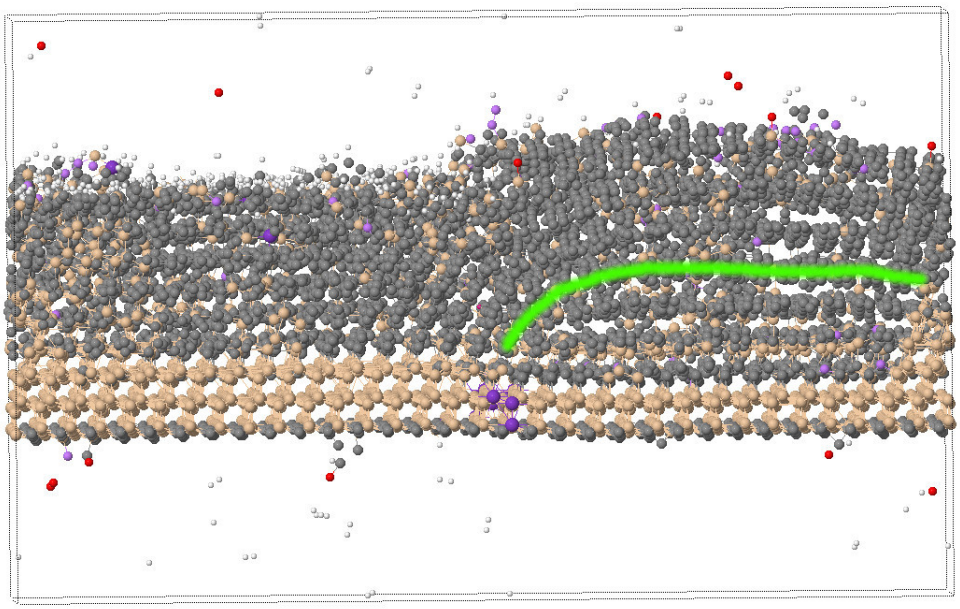

Figure 38: 50% strip hydrogen terminated (111) slab, 2500 K - sp^2 bond forming has spread to the hydrogen terminated half of the slab (left-hand side) but has not necessarily formed graphene layers parallel to the surface. Graphitic layers underneath the clean surface (right-hand side) merge with (111) layers of a different orientation forming curved sheets.

(110) Surface

With the (110) sample, the clean surface was stable to much higher temperatures (Table 8) than the (111) surface. This is due to the fact that there are no partially sp^2 bonded (111) bilayers ready to become graphene sheets as there are with the (111) surface.

Sample	Temp (K)
Bulk	3100
Clean	2400
H-terminated	1900

Table 8: Temperature at which the diamond structure begins to re-order (beginning of graphitisation).

Since for the (110) surface there is no dominant orientation for graphene layers to form (the four (111) directions are equally as likely), domains develop which merge at interfaces resulting in a 'herring-bone' pattern. The combined effect of this can result in graphene layers that zig-zag. The four (111) planes can make two pairs which result in this pattern. For the clean (110) slab (see Figure 39), this causes surplus would-be graphene left at the surface, in one of these zig-zag valleys, to close up on itself and form tube-like structures. Although some sp^2/sp^3 mixing exists at domain interfaces, this is surprisingly efficient in maximizing the number of sp^2 bonds.

The hydrogen-terminated surface graphitised at a slightly lower temperature than did the (111) hydrogenated surface and with a lot less disorder with about 90% of the unfrozen carbons taking on sp^2 bonding. This is because two (111) planes exist perpendicular to the (110) surface which may gradually separate and uniformly propagate graphitisation. This develops as pyramidal domains nucleated at the surface where there is more freedom for structural change (see Figure 40). The final graphene layers remain straight because the ends are generally terminated with hydrogen and thus they do not need to satisfy any dangling bonds (Figure 41).

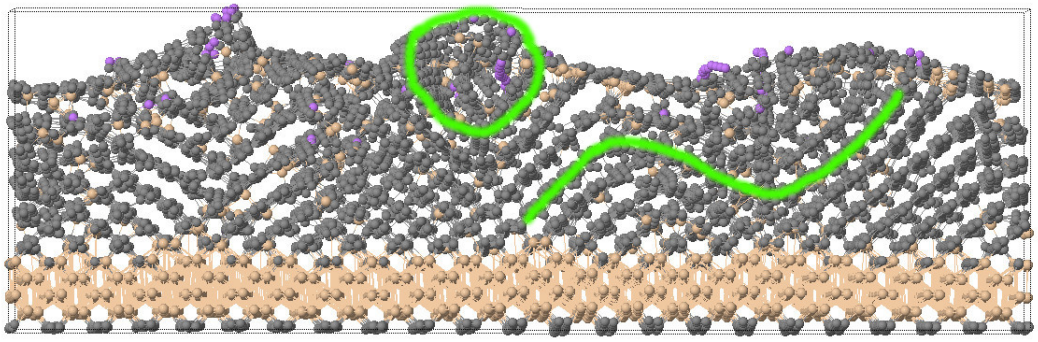

Figure 39: Clean (110) slab at 300 K, post-heating - Zig-zag graphene layers leave cylindrical tubes at the surface as they seek to satisfy dangling bonds at the edge of graphene layers.

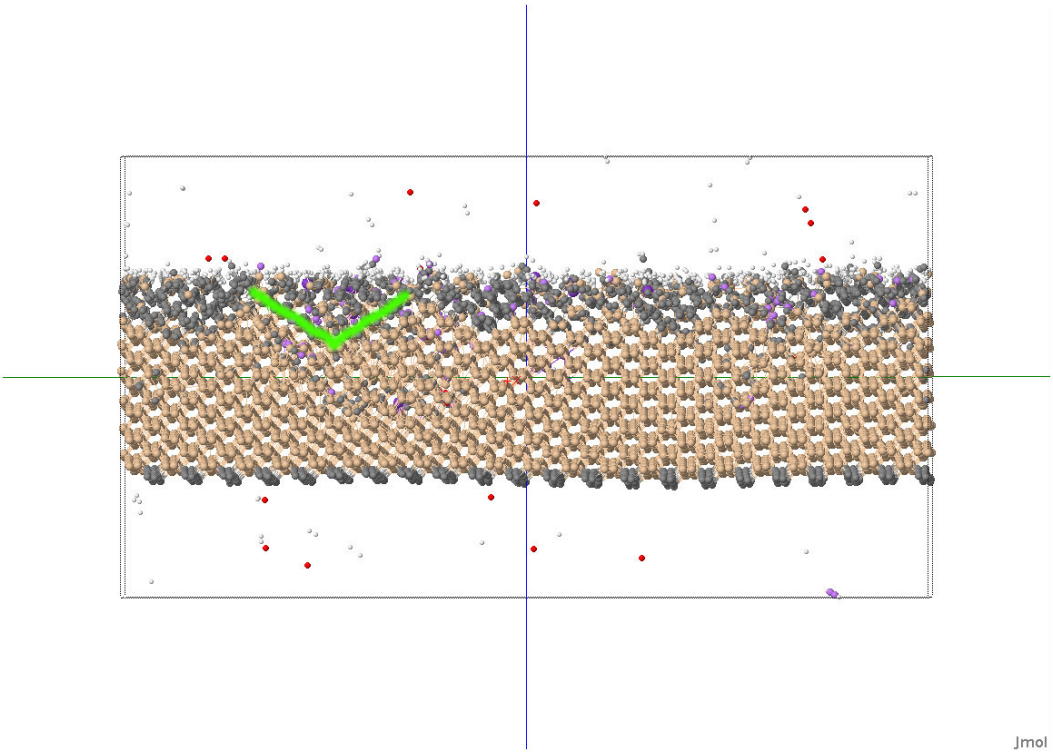

Figure 40: Hydrogen terminated (110) slab at 2068 K, pre graphitisation. Some pyramidal domains of graphite have nucleated at the surface and are propagating into the slab.

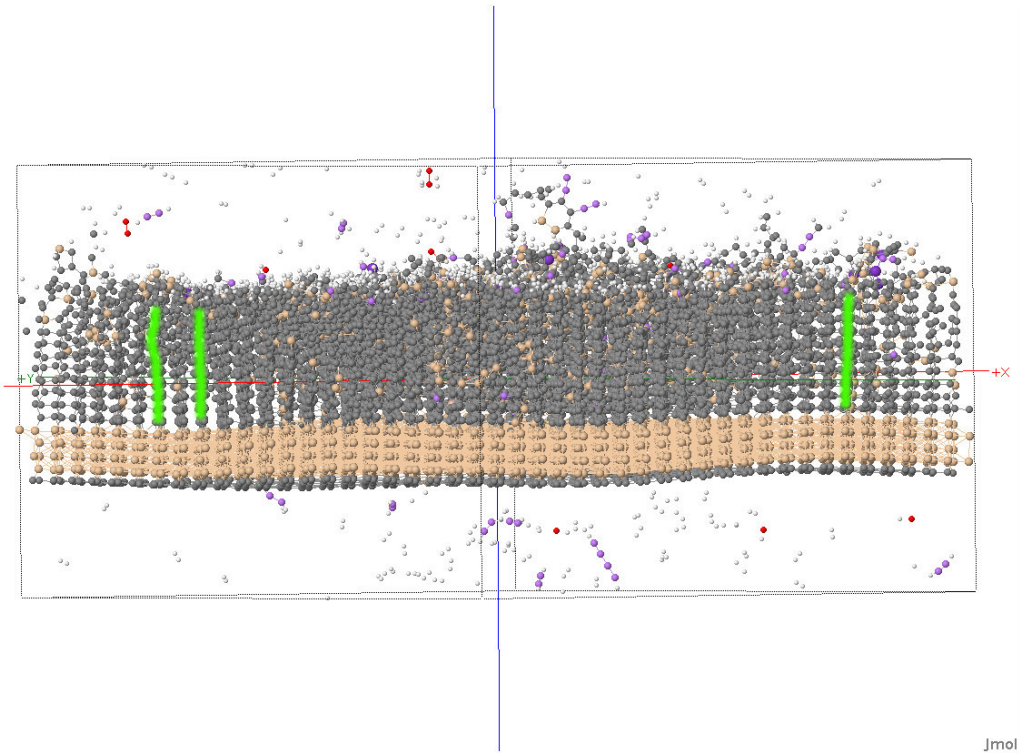

Figure 41: Hydrogen terminated (110) slab at 2918K, post graphitisation. The two (111) planes perpendicular to the (110) surface have preferentially graphitised. The slab is orientated so that a corner of the sample in the x-y plane is pointing out of the page - this is so that the graphine layers can be seen better in a snap-shot.

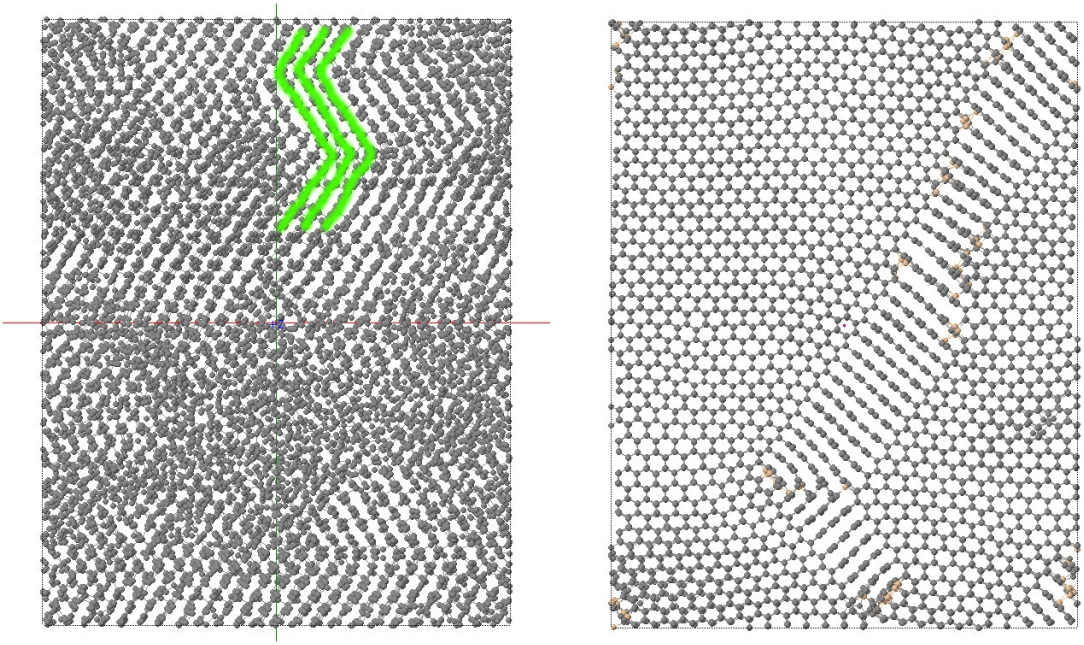

Figure 42: Left: Hydrogen terminated (110) slab at 2918 K, post graphitisation - Top view of the sp^2 bonded carbon only (other carbon removed from image). The graphene layers form perpendicular to the (110) surface where the dangling bonds of the graphene sheet edges are already passivated with hydrogen. There are two (111) planes perpendicular to the surface, and without any obvious choice of orientation they form the herring-bone pattern of connected domains. Right: Bulk (110) at 300K, post graphitisation - The bulk does not have the preference of passivating layers in any one direction and so graphene orientation in the other two (111) directions also occurs (not necessarily perpendicular to the surface, in this case the majority is parallel).

(100) Surface

Sample	Temp (K)
Bulk	2400
Clean (1×1)	700/1700
(1×1):H	1000
(1×1):2H	500

Table 9: Temperatures at which the (100) diamond structure begins to re-order (beginning of graphitisation).

The bulk (100) sample underwent clean graphitisation between 2400 K and 2800 K as did the (111) bulk. Interestingly, the clean (1×1) surface began to undergo sp^2 bond forming at the surface (and just below) at 700 K until 1000 K, but then stopped until at about 1700 K. Only from this temperature on did graphitisation begin to propagate into the sample properly, with complete graphitic sp^2 restructuring at about 2500 K (Figure 43). The final sample had very little surface disorder.

The (100) monohydride surface, (1×1):H (one H atom for each surface C), cleanly graphitised between 1000 K and 2000 K with little surface disorder. However, the dihydride surface, (1×1):2H, was problematic from the beginning with hydrogen release at room temperaure. Surface disorder encouraged graphitisation at low temperature (500 K) resulting in about 80% sp^2 bonding by 2500 K but with large surface disorder and hydrocarbon molecules breaking away from the surface. In a DFT study, Sang Yang *et al.* [77] concluded that this (1×1):2H surface was energetically unstable due to strong H-H repulsion between adjacent surface sites. This favorably relaxed to the (1×1):H structure which Yuemei L. Yang and D'Evelyn [75] found to be the most stable (100) surface over the temperature range of 298-1500 K.

5.4 Chapter Summary

This chapter is a comparative study of the behavior of three *ideal* diamond orientations on heating. The general conclusion drawn is that surface reconstruction plays a large role in stablising against graphitisation. Where atoms are able to easily form sp^2 bonds with reciprocating neighbours graphitisation happens at lower temperatures. The extreme case is the clean (111) surface which begins to undergo a phase change above 500 K.

Temperature thresholds reported here, especially the high temperatures of graphitisation, do not necessarily relate to experimental values, and vary wildly here be-

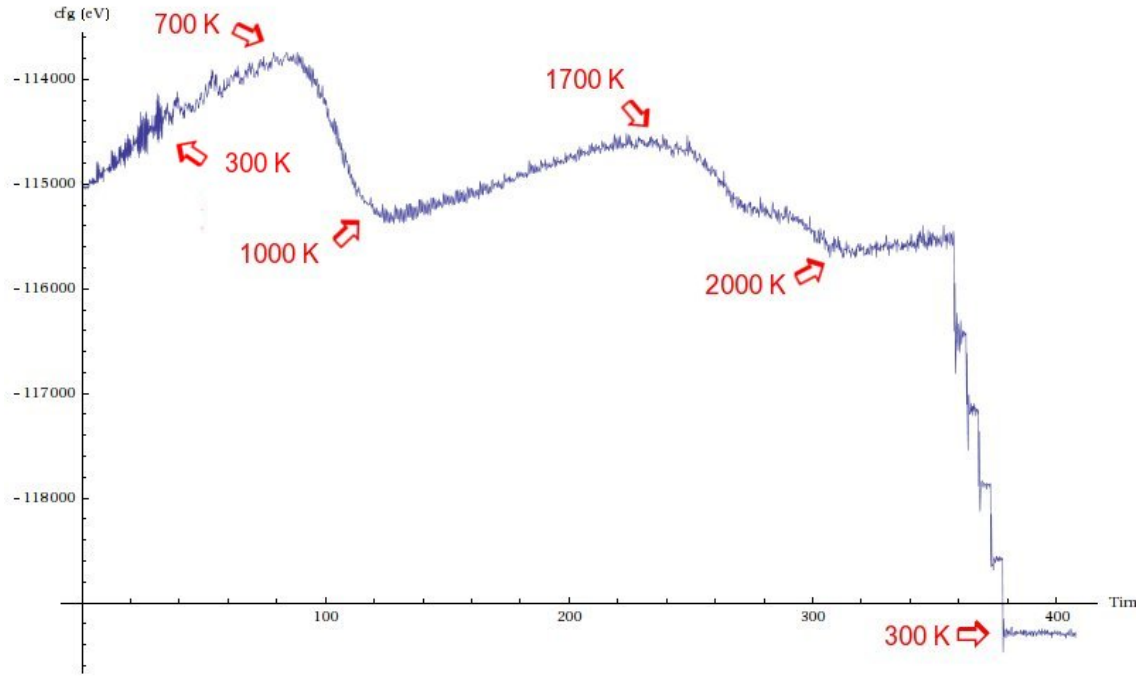

Figure 43: Plot of lattice energy (eV) with time (ps) for heating of the **clean (100) sample** - As with all others, heating the sample gradually decreases the configurational lattice energy. In addition to this, there are two periods of sp^2 bond forming which sharply reduce lattice energy. One between 700 K and 1000 K where the surface (and just below) predominantly adopts sp^2 bonding, and then again between 1700 K and 2000K where graphitisation propagates through to the rest of the slab.

cause these are simulations of uniform, ideal surfaces. As seen with the gradated hydrogenation of the (111) surface, if sp^2 bond formation can take place in one area it will act to initiate the process of graphitisation. Generally speaking, it is observed that at about 600 K the surface is able to restructure slightly. Depending on the surface, this will either initiate graphitisation, as with the (111) case, or simply minimise surface energy further, as with the (100). Above this, true graphitisation may occur above 1000 K, again depending on the structure. With the bulk and (111) 100% hydrogenated samples diamond structure remained to very high temperatures because there was no defect to initiate sp^2 bond formation.

Of the bulk samples, it is surprising to see the (110) sample graphitising at such a distinctly different temperature from the other two since in the bulk form these orientations are essentially equivalent. This is most likely due a size effect: although the diamond structure is similar in all directions, graphite is not. This could very well have an effect on the temperature of this phase change since the diamond (111)

	Temp (K)		
	(100)	(110)	(111)
Bulk	2400	3100	2500
Clean	700/1700	2400	500
H-terminated 100%	500†	1900	2000
H-terminated 50%	1000#		1000*
H-terminated 50% (strip)			500
H-terminated 25%			500

Table 10: Summary of temperatures of graphitisation for different diamond orientations and at varying degrees of surface hydrogenation.
∗ random coverage
† dihydride (1×1):2H surface
# monohydride (1×1):H surface

hexagonal layers contract on graphitising.

For the clean surfaces, the (110) sample offered by far the lowest surface energy. This concurs with it having the highest temperature of graphitisation, close to that of the bulk diamond. The (111) surface is particularly susceptible to graphitisation since all upper-surface atoms are already sp^2 bonded and already make up half of the first (111) bilayer, which preferentially becomes a graphene sheet. The (100) surface underwent two periods of obvious structural change, the first of which was at about 700 K. Since this initial change was localised at the surface only, it can perhaps be attributed to a surface reconstruction closer to the energetically favorable (2×1) dimerisation mentioned above [72, 77]. True graphitisation begins to penetrate below the (100) surface at about 1700 K.

Terminating the surfaces with hydrogen, in an effort to passivate dangling bonds and replicate a bulk-like sp^3 bonding, had the greatest effect on the (111) surface. It seems the strong influence of the surface sp^2 bonded atoms on their neighbours does rapidly induce layer-by-layer graphitisation. Passivating these dangling surface bonds not only removes the immediate opportunity to form sp^2 bonds with neighbours but restores diamond tetrahedral bonding, whereas the (100) and (110) surface energies may be lowered by forming fewer but stronger bonds, and not in the tetrahedron structure. Where the clean (111) surface does not reconstruct a great deal, with surface atoms not forming stronger bonds with neighbours, it does readily reform the diamond structure on hydrogenation. Reducing the level of random hydrogen coverage reduced the temperature of graphitisation, since propagation of sp^2 bond forming nucleates from un-passivated atoms. A lower limit of about 25%

coverage results in graphitisation at a similar temperature to the clean surface. However the upper graphene sheets in this case are not so orderly due to the presence of remaining hydrogen.

The (110) H-terminated surface, however, graphitised at about the same temperature as the (111) but with a lot more order. This is due to the hydrogen atoms in the (110) structure passivating dangling surface bonds, which then later terminate the ends of the graphene layers, allowing neat vertical graphite strips to form.

The monohydride (100)(1×1):H surface did not passivate all surface dangling bonds (only one of two per surface atom) and lead to graphitisation at quite a low temperate, one only marginally better than that of the clean (100)(1×1) surface. However, graphitisation in this case was relatively neat. In contrast, the dihydride (100)(1×1):2H surface rapidly disordered at the surface at very low temperatures (>300 K) and therefore quickly allowed disorderly graphitisation to propagate. In concurrence with Sang Yang *et al.* [77] findings, it is concluded that this dihydride configuration is not stable, despite allowing for greater surface bond passivation. A promising alternative is a (2×1) dimerisation between two adjacent surface atoms plus a single hydrogen bonded to each - the (100)(2×1):H reconstruction.

6 Diamond Tritium Bombardment

A plasma facing component in the divertor region of a tokamak will be exposed to high fluxes of hydrogen and its isotopes. For ITER this is expected to be of power loads ∼10 MWm^{-2} [78] which corresponds to ion fluxes of $\phi = 2\text{-}6 \times 10^{24}$ ions $m^{-2}s^{-1}$ at energies 10-30 eV. As mentioned above, a major disadvantage of using carbon is its high reactivity with hydrogen. This can lead to enhanced sputtering and tritium retention. The severity of this, however, is hugely dependent on the carbon structure, including carbon bond-hybridisation ratios, lattice regularity and hydrogen saturation. Experiments have shown that even within the sub-category of carbon fibre composites, sputtering yields can differ drastically due to topological differences, for example, where erosion was observed to occur preferentially between fibres [12]. It is therefore reasonable to expect that the rigid diamond lattice may behave very differently from other carbon structures, such as graphite and amorphous carbon, on exposure to fusion plasmas.

In this section, diamond surfaces of temperatures 300-2100 K were exposed to incident 15 eV tritium atoms at a flux of $\phi = 10^{29}$ ions $m^{-2}s^{-1}$. The tritium ions were modelled using hydrogen parameters but with three times the proton mass. Note that throughout this section, and others relating to tritium bombardment, the terms *atom* and *ion* may be used interchangeably to refer to the incident particle even though charges are not explicitly modelled. Similarly, use of the terms *hydrogenation* and *hydro-carbon* are extended to refer to bonding with hydrogenic isotopes as well.

6.1 Method

The surfaces detailed in Section 4, the clean and hydrogenated (100), (110) and (111) diamond orientations, were gradually heated up in Section 5 in investigating their resistance to graphitisation. In this section, each surface was taken at temperatures 300 K, 600 K, 900 K, 1200 K, 1500 K, 1800 K and 2100 K and exposed to tritium bombardment at about one incident ion every 0.3 ps. The exact interval time was varied slightly accommodating for small differences in bombarded surface area in keeping the incident flux fixed (see Table 6.1).

Whereas in Section 5, where the samples were prepared and heated to the desired substrate temperatures, a Nosé-Hoover *nvt* thermostat was used in scaling all atomic velocities, here a Langevin thermostat[10] was employed to scale only a selection. The

[10]See the DL_POLY_3 manual: `http://www.cse.scitech.ac.uk/ccg/software/DL_POLY/`

samples were made from bulk material by opening-up the z-boundary and effectively creating a vacuum. The slabs remained continuous in the x-y plane, and it's here at the edges of the cell that the Langevin thermostat stochastically adds/subtracts random elements of velocity depending on the desired temperature. The influence of the thermostat was limited to within 4 Å of the cell edges and ion bombardment was targeted at the surface at least 6 Å from the edge. This outer perimeter thus acts as a heat sink, removing incident energy as it dissipates, without the need to actively scale the velocities of any atoms involved with bombardment interactions. Atoms within the first 2 Å of the slab underside were frozen and only the topside was bombarded with tritium.

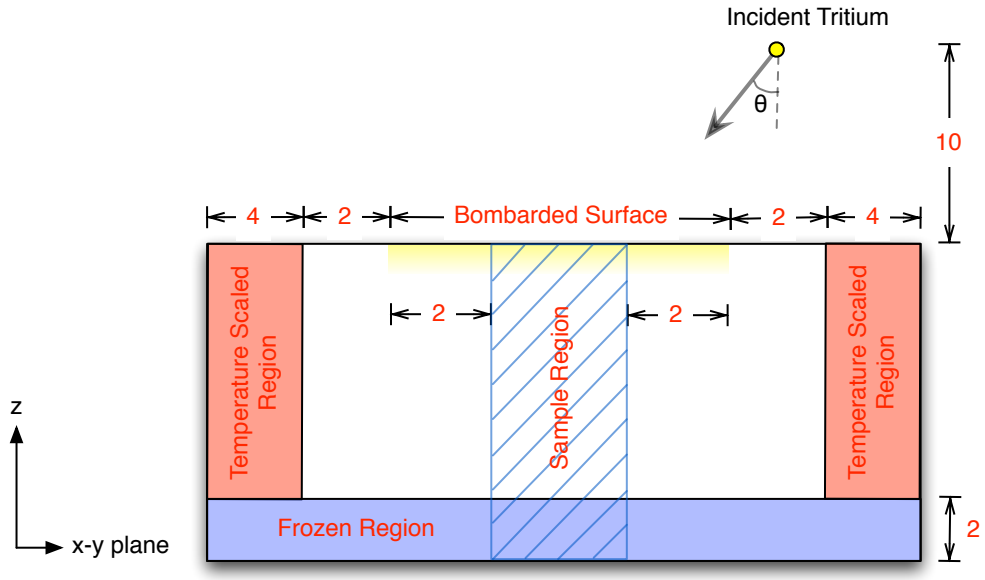

Figure 44: Schematic cross-section of a bombarded sample. Atoms initially in the frozen region are chosen to be fixed, *i.e.* they never acquire any velocity. Carbon atoms that at any point fall within the temperature scaled region are subject to the Langevin thermostat. Incident tritium atoms bombard a surface at least 2 Å from this scaled perimeter. Later in this section *depth profiles* in the z-direction will be taken in quantifying structural damage and tritium retention, this is sampled from within the bombarded surface 4 Å from the scaled regions. Distances are labelled in Angstroms and not drawn to scale.

Each incident tritium was introduced to the system at a height of 10 Å above the surface with a kinetic energy of 15 eV. Impact site coordinates were selected randomly, as were off-normal incident angles in the range $0° < \theta < 80°$ (the azimuthal angle was completely randomized). A velocity-Verlet integration algorithm [79] with time-steps of 1 fs was used and an interval of about 0.3 ps was chosen between incident impacts, which corresponds to an ion flux $\phi = 10^{29}$ ions $\mathrm{m}^{-2}\mathrm{s}^{-1}$.

Material was considered as sputtered or reflected if it was found 10 Å above the surface at the end of each 0.3 ps run and was removed from the simulation. Exact times in between impacts for the different surfaces are given in Table 6.1.

Slab	Bombarded Area	Impact Interval
(100)	(72.16-12)×(72.16-12) = 3619.23 Å^2	0.265 ps
(110)	(60.40-12)×(78.31-12) = 3209.40 Å^2	0.300 ps
(111)	(68.58-12)×(70.33-12) = 3300.31 Å^2	0.291 ps

Table 6.1 - Bombarded areas and impact time intervals fixing incident tritium flux to $\phi = 10^{29}$ ions m^{-2}s^{-1}. Bombarded areas are evaluated as the product of total surface dimensions less 6 Å in both directions. Thus the bombarded area is at least 2 Å from the 4 Å temperature scaled perimeter.

It was decided to use only the REBO part of the whole AIREBO potential (see Section 4.2 for details of the potential). The additional Lennard-Jones term in the AIREBO is especially useful for modelling gaseous hydrocarbon particles but comes at a huge computational cost (see Figure 23). Since we are simulating what is largely a dense solid over large time scales (large by molecular dynamics standards), and those molecules which are sputtered are quickly removed, it was decided that this was a compromise worth making. The dominant bond-order term which considers carbon bond hybridisation strength is integral to the REBO part and preliminary tests showed little difference in using the two for this simulated environment.

In Section 5 the three surface orientations were found to graphitise at different temperatures. This was attributed to the energetic stability of the surfaces, largely based on bonding (severed and reconstructed), and orientation of the conventional (111) planes (which preferentially form the graphitic layers). In addition, the passivation of dangling bonds with hydrogen went some way to replicating bulk continuation of the material and so increased resistance to graphitisation. Throughout all of this we are dealing with ideal structures. On bombardment with tritium, however, following induced damage at the surface there remains little to distinguish between the samples other than orientation of the original (111) planes. This considered, it is not then surprising that following initial surface disruption, the nature of bombardment damage and tritium retention showed no dependence on crystal orientation (Figure 45). Similarly for the the hydrogen-terminated surfaces, not only was there no clear distinction between the different orientations, but once surface hydrogen had initially been removed via bombardment there was little difference

between the clean and hydrogen-passivated surfaces. With this in mind, and for the sake of continuity, only the (110) clean surface will be discussed in detail throughout this section, but may be taken as an example of the general case. If anything, with regards to tritium retention, it may be argued that the (110) surface would possibly present a worst-case-scenario since here the conventional (111) diamond planes are perpendicular to the surface. The reason being, as seen in the above Section 5, given enough energy these (111) diamond planes preferentially form the graphitic layers. In this situation inter-layer bonds are severed and intra-layer bonds are strengthened, thus potentially opening up direct routes for tritium transport into the bulk material.

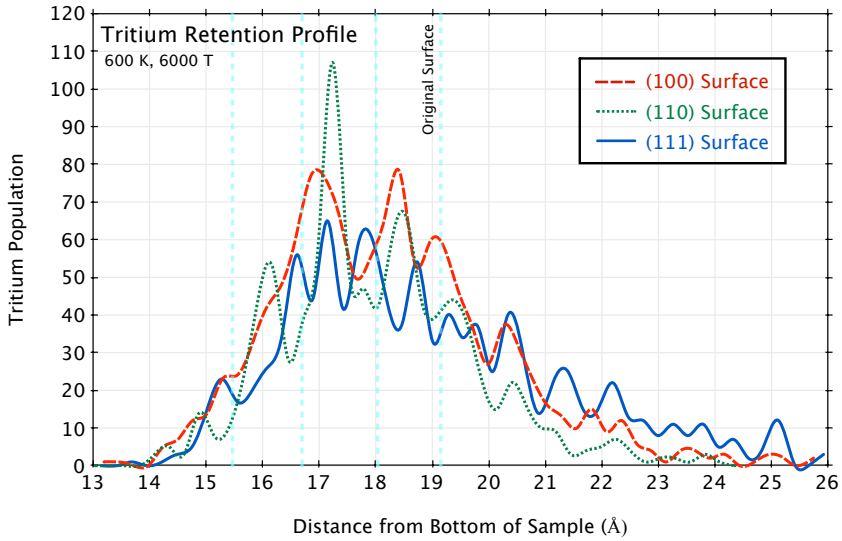

Figure 45: Tritium retention profiles at 600 K after a fluence of 6000 T for the three clean surface orientations: (100), (110) and (111). Dashed vertical lines show positions of the (110) diamond layers. Depth profiles, tritium retention levels and level of damage were similar for all three surfaces.

6.2 Structural Damage

At each substrate temperature 18000 cumulative impacts were executed, equivalent to a total simulation time of 5.4 ns and a fluence of 5.4×10^{20} ions m^{-2}.

As explored above in Section 5, diamond will undergo a phase transition and graphitise given enough energy. It is reasonable to expect this change at about 1000 K. Bombardment of the original diamond surfaces over the temperature range 300-2100 K will cover this and so it is possible to contrast the bombardment of an ordered diamond structure with one that has been thermally damaged/graphitised.

Final images of the bombarded slabs at from 300 K to 18000 K are shown in Figures 46, 47, 48 and 49.

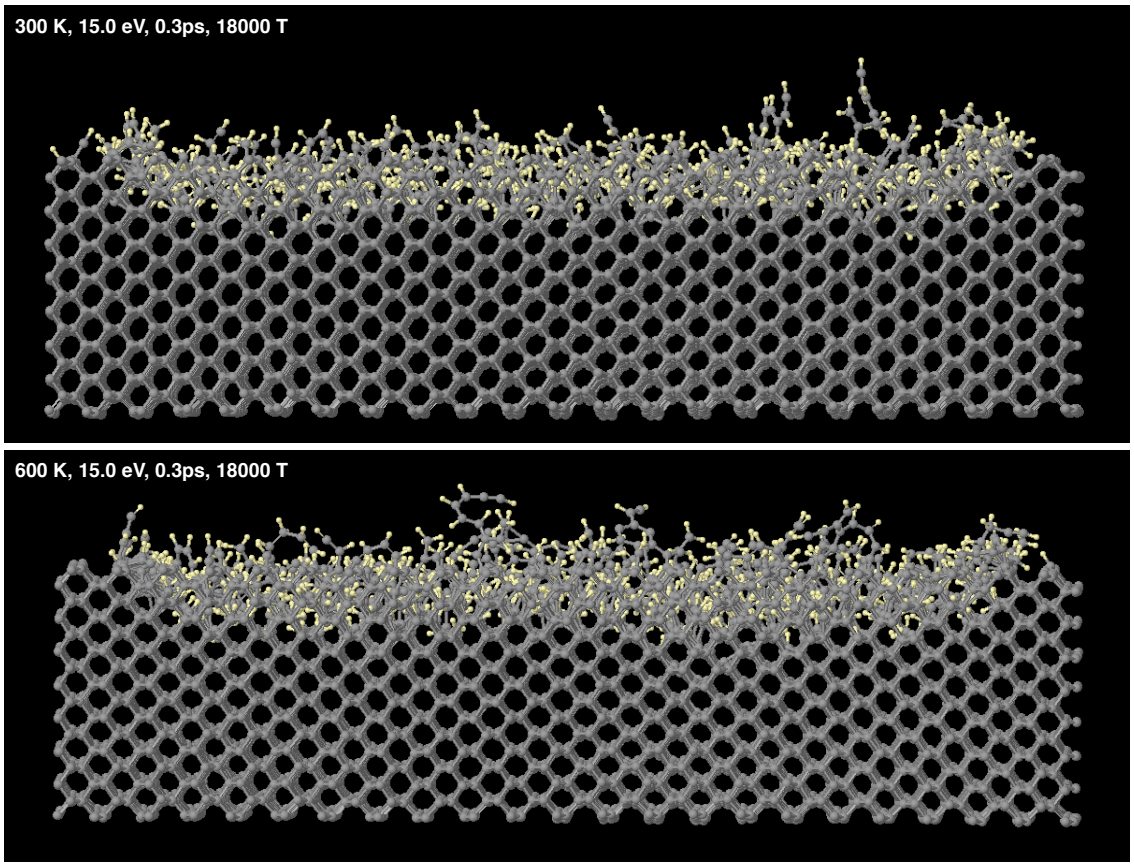

Figure 46: 300 K and 600 K (110) slabs following bombardment with 18000 tritium atoms. Tritium accumulates at the surface, and also produces protruding hydrocarbon chains. Below the retentive area the diamond structure is maintained.

If the incident ions do not have enough energy to sputter material kinetically ($<$ 30 eV for carbon) the term *chemical sputtering* is used to highlight the significance of chemically breaking bonds in the sputtering of material. As an extension to this, Salonen *et al.* [80] highlight a process they term *Swift Chemical Sputtering*. The underlying mechanism of this involves the impinging ion having enough kinetic energy to place itself in-between two otherwise chemically bonded atoms and so break the bond. If the bond was the last C-C connection between a hydrocarbon and the substrate, the molecule may be sputtered. It was observed in this study that when the ideal diamond surface is initially bombarded, it is by this process that surface atoms begin to break bonds with those below. As more bonds become broken, the surface loses more of its ideal structure, opening up more dangling bond sites re-

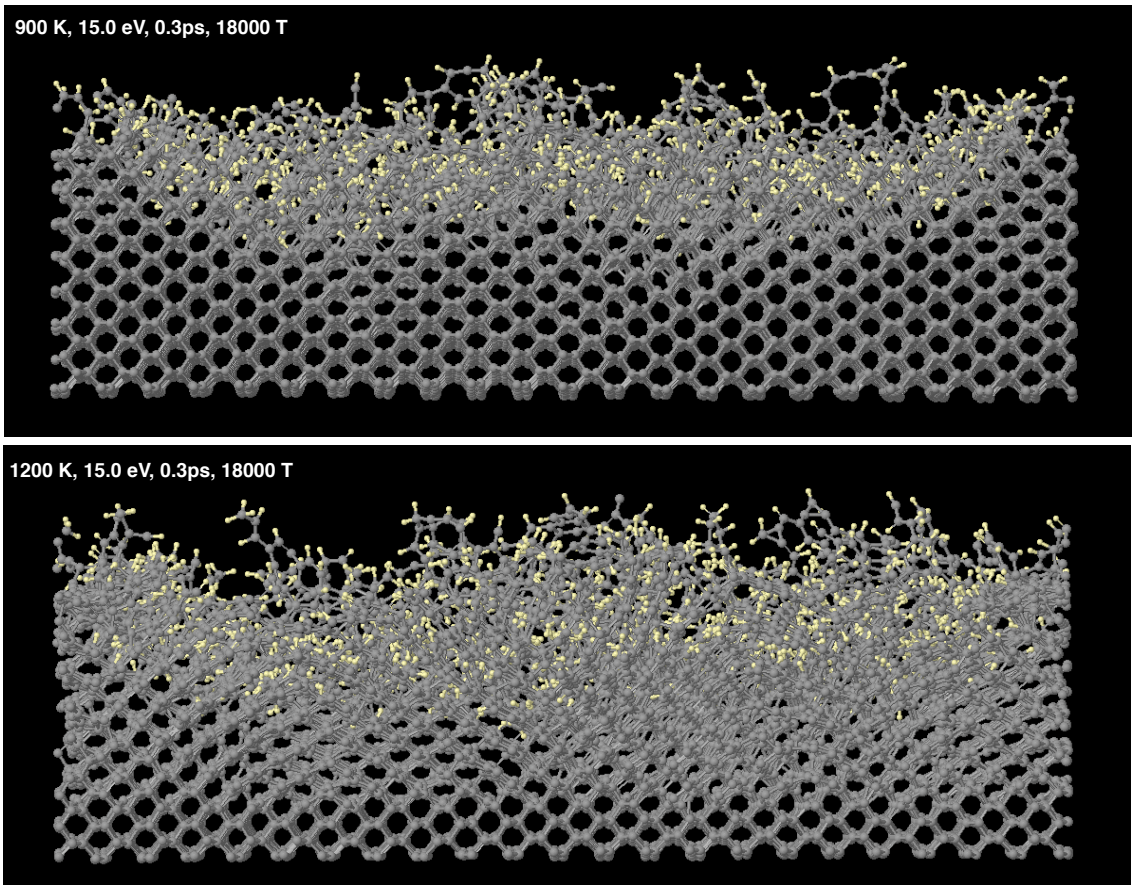

Figure 47: 900 K 1200 K (110) slabs following bombardment with 18000 tritium atoms. At temperatures approaching the graphitisation threshold diamond structure is lost near the surface. This allows for deeper tritium penetration and longer protruding hydrocarbon chains.

ceptive to bonding with incoming tritium and allowing incident ions to penetrate deeper. This quickly leads to structural damage and disorder in the diamond surface and so discussing specific surface orientations begins to lose significance.

In the current simulations it was observed that as carbon material was eroded from a diamond structure, tritium accumulation at the surface developed in-between what remained of the diamond layers. This can be clearly seen in the 600 K atom depth profile plotted in Figure 51a. Beneath this, and to the same x-axis scale, Figure 51c shows a depth profile of carbon atoms only, distinguishing between atoms with four or three nearest neighbours (either other carbon atoms or tritium) interpreted as sp^3 and sp^2 bonding respectively. Highlighted here is that as carbon atoms are eroded, adjacent carbon atoms remain roughly in their original positions. The number of atoms with two or one nearest neighbours was negligible, demonstrating that even with a strong preference to form sp^2 bonds, remaining carbon atoms retain

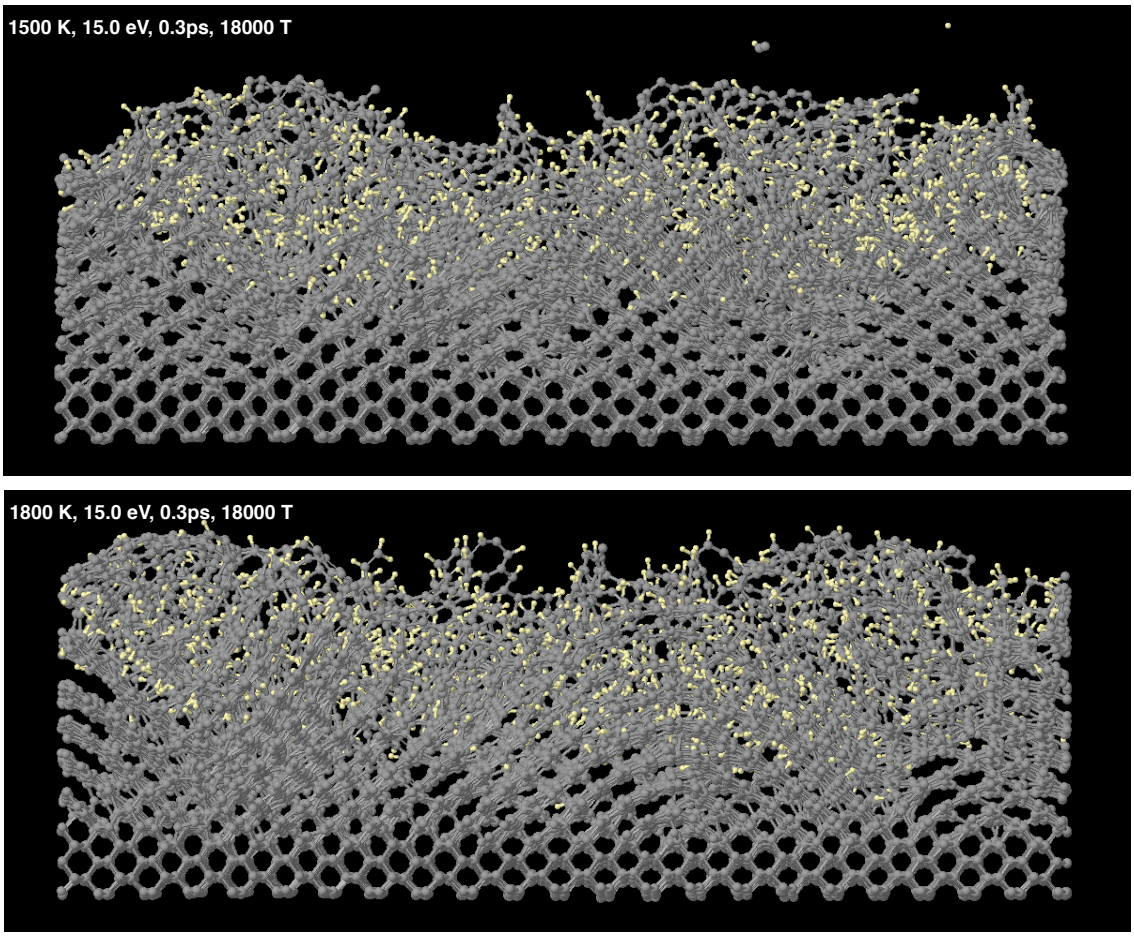

Figure 48: 1500 K and 1800 K (110) slabs following bombardment with 18000 tritium atoms. At temperatures above the graphitisation threshold diamond structure throughout the sample which allows for much deeper tritium retention.

their original diamond co-ordinates.

Increasing the substrate temperature leads to further structural damage. As the temperature threshold of graphitisation is approached, given that the incident ions also impart a certain amount of thermal energy at the surface, the upper layers in which tritium is deposited lose a lot of their diamond structure. This is evident at 900 K in Figure 51b where retained tritium is no-longer accumulated in tidy peaks behind diamond layers. Looking at the carbon bond-type profile at 900 K (Figure 51d) the extent of bond breaking penetrates much deeper than the tritium does and there is little sp^3 bonding within the tritium retention area (>15 Å from the bottom of the slab). Despite this, carbon atoms below the tritium retention remain in original diamond z-positions. The profile of this sp^2 bonding suggests that this is a surface induced effect (*i.e.* not simply due to substrate temperature), since it reduces away from the surface, and could be an artifact of these extremely high

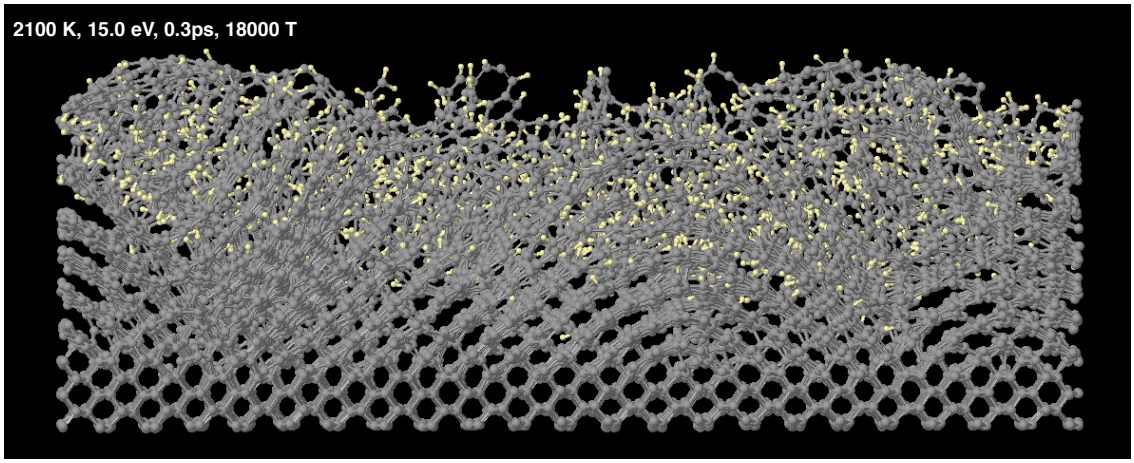

Figure 49: 1800K (110) slab following bombardment with 18000 tritium atoms. With exception of the frozen lower 2 Å and atoms immediately above the structure has graphitised, allowing deeper tritium penetration

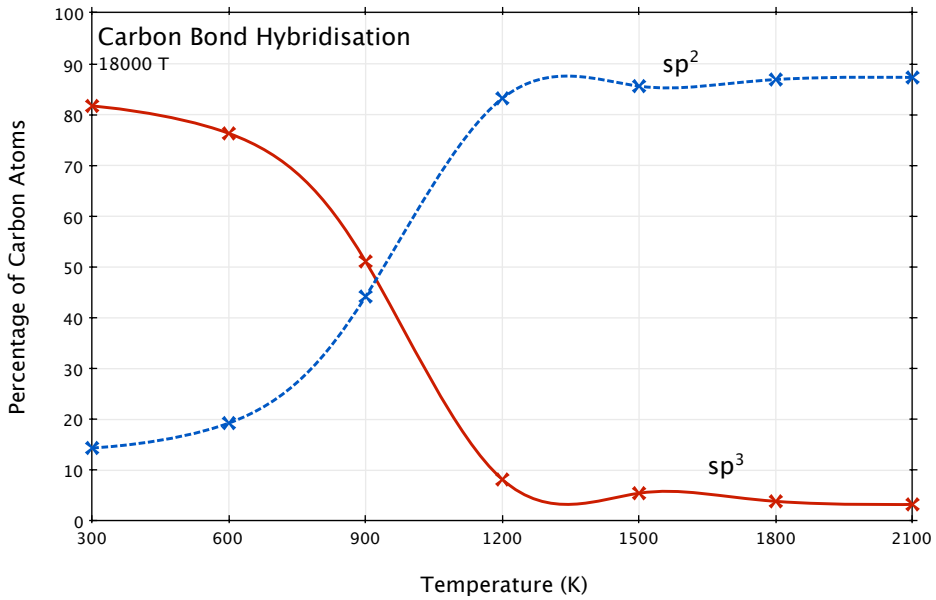

Figure 50: Carbon bond-hybridisation mixing with increasing temperature (sampled 5 Å from cell edges and bottom surface). Although bond breaking becomes significant, and the population of sp^2 bonding increases, for 900 K, these carbons remain in diamond like positions (see Figure 51d).

fluxes (10^5 orders of magnitude larger than actual divertor conditions). However, despite this, the depth at which tritium is retained is not too dissimilar from the 600 K case (∼5 Å below the original surface). This suggests that even though the upper surface suffers greater damage, and bond-breaking has propagated down in to the sample, the remaining diamond-like structure beneath prevents deeper tritium penetration.

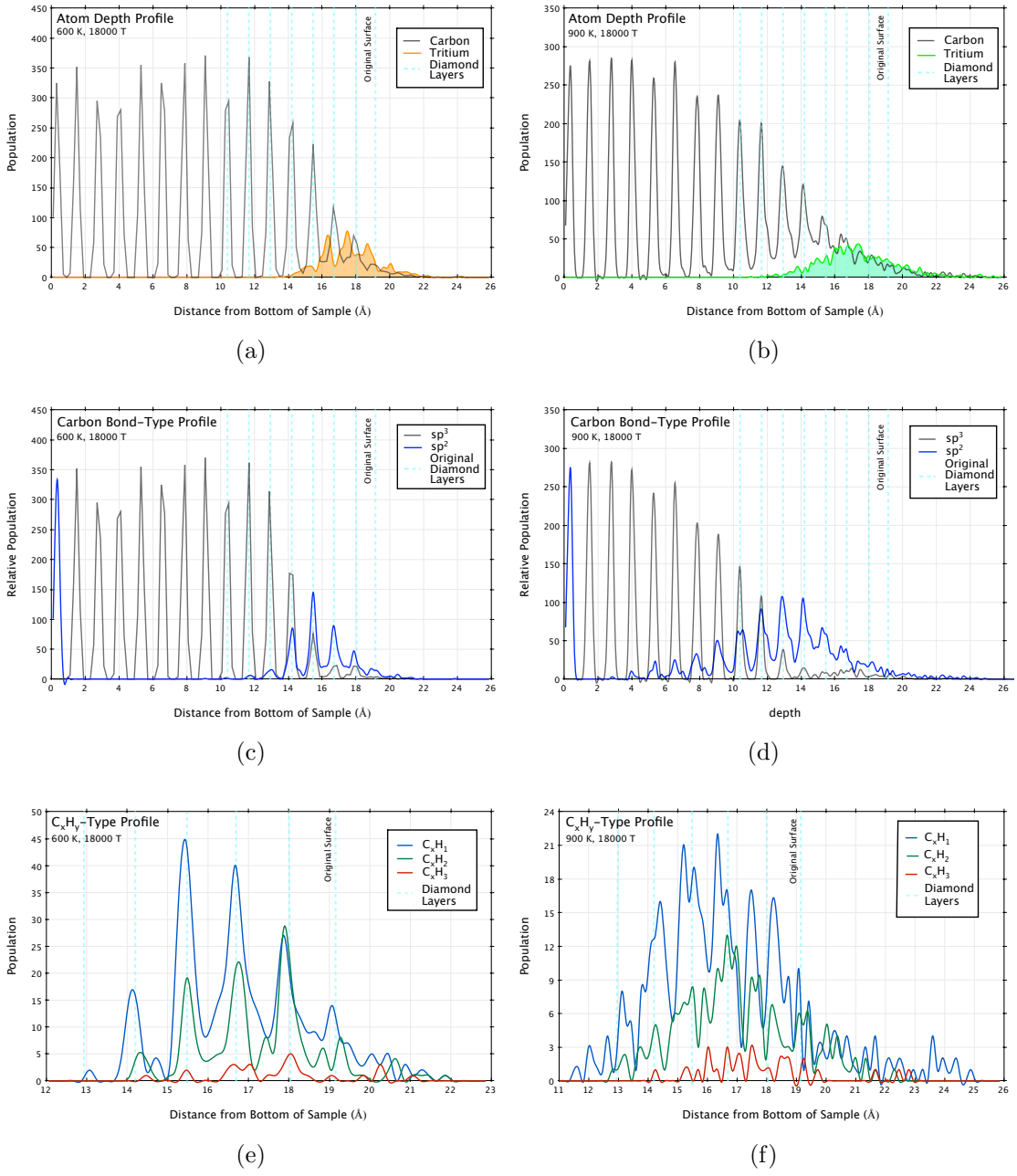

Figure 51: (110) atom depth profiles at 600 K and 900 K following bombardment with 18000 tritium atoms at a flux of $\phi = 10^{29}$ ions $m^{-2}s^{-1}$. a) and b) show atom depth profiles and the extent of tritium retention. c) and d) show the bonding ratios of carbon atoms. Seen here is that even though sp^2 bonding is forming due to damage, remaining carbon are situated in the original diamond positions. e) and f) show the saturation of carbon atoms within the damaged region. Above about 1000 K the diamond lattice begins to break down. Below this temperature the residual diamond structure, beneath surface damage, prevents deeper tritium penetration and thus further damage.

At temperatures above ∼1000 K the samples have all largely graphitised (as seen in the sp^2/sp^3 ratios in Figure 50 and bond-type profiles at 1500 and 1800 K in Figures 52c and 52d). This temperature is slightly lower than was found in Section 5 for the ideal surfaces (*i.e.* without defects) but does correspond to the surface induced graphitisation of the partially hydrogenated samples (see Section 5.4). Since the progression of graphitisation with temperature seems to be surface induced (see Figure 51d) the graphitisation is most likely enhanced by surface damage and incident energy flux due to bombardment. Figure 49 shows the 1800 K slab following bombardment. In this case, the graphitic layers have formed herringbone (see Section 5.3 on the (110) graphitisation pattern) zig-zags perpendicular to the x-z plane. These layers facilitate greater tritium transport deeper into the slab. At 1500 K and 1800 K, Figures 52a and 52b show that tritium can penetrate to a depth of at least ∼10 Å below the original surface. In addition to this, tritium is retained to a similar height above the original surface. This is not simply due to protruding hydrocarbon chains, as with the lower temperature samples, but also due to swelling. The inter-graphitic-plane separation is ideally ∼3 Å, about twice as large as the C-C bond separation that existed between the planes as diamond (111) layers. Although this is not a 'clean' graphitisation, in that the there are small domains of perpendicular graphitic layer orientation, there will still be some extension into the z-direction. Adding to this, we now have incident tritium atoms damaging what graphitic structure exists as well as positioning in-between the layers, thus enhancing swelling.

In summary, the majority of the structural damage observed in these simulations was dominantly due to substrate temperature, *i.e.* thermally induced graphitisation. Thus it is reasonable to consider the low-temperature and high-temperature samples as different structures, specifically diamond and graphite-like respectively.

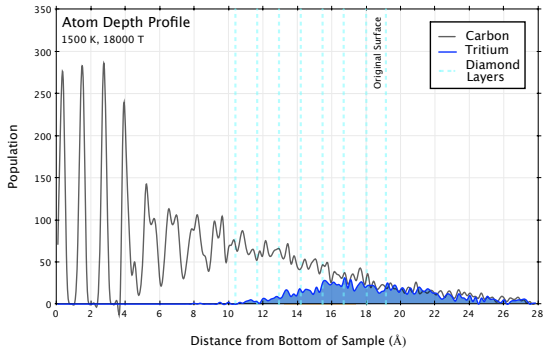

(a)

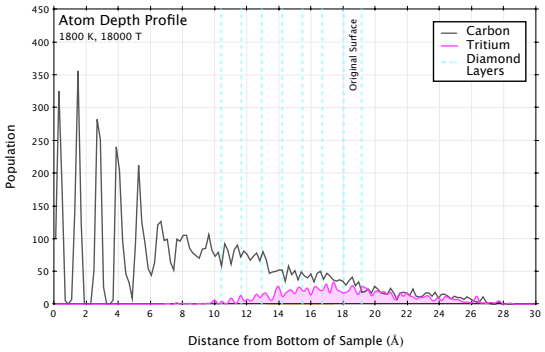

(b)

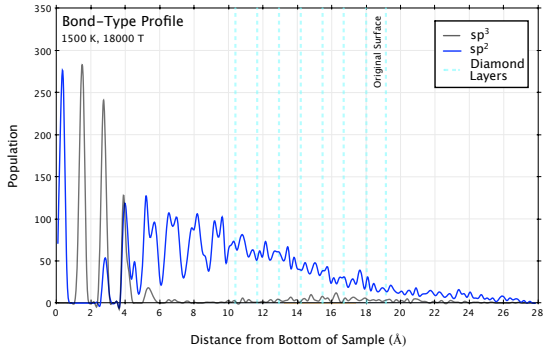

(c) (compare with net ratios in Figure 50)

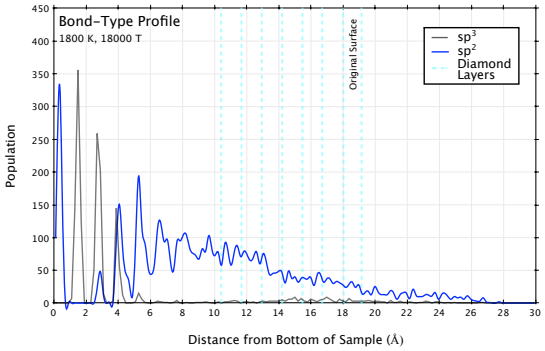

(d) (compare with net ratios in Figure 50)

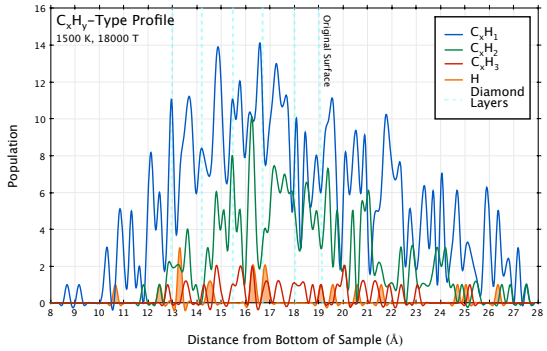

(e)

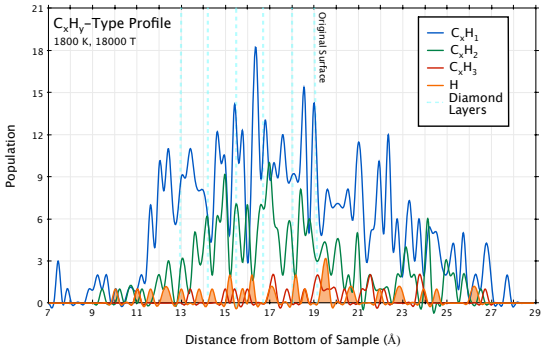

(f)

Figure 52: Depth profiles like Figure 51 for the 1500 K and 1800 K (110) samples following bombardment with 18000 tritium atoms at a flux of $\phi = 10^{29}$ ions $m^{-2}s^{-1}$. Positions of the original pre-bombardment diamond layers are shown with dashed light-blue lines. Greater structural damage due to substrate temperature (graphitisation) allows for deeper tritium penetration.

6.3 Tritium Retention

During the course of bombardment, the majority of incident tritium was reflected, especially initially when the target was a clean and relatively undamaged diamond surface. Naturally, as the surface became damaged, and more C-C bonds were broken, and thus receptive to incident tritium, the rate of retention increased. During this initial surface damage period, at all temperatures, there was a net tritium retention rate of about 26%. After 6000 incident ions (an equivalent fluence of 1.8×10^{20} ions m^{-2}) this rate dropped-off and the surface tritium levels began to saturate (Figure 53a). Samples that strongly remained diamond-like (300 and 600 K) showed a convergence to a saturation level of 1200 tritium atoms (a surface density of 3.7×10^{19} ions m^{-2}). The graphite-like samples ($\geq$ 900 K) did not clearly converge to a particular level within the given simulation time, which could be due to the ability of tritium to diffuse down into the sample (as discussed above) and neither easily desorb nor hinder further accumulation at the upper surface. Examining final tritium retention levels (Figure 53b) shows a clear difference between the two temperature dependent structures with retention levels rapidly increasing for temperatures $\geq$ 900 K. This corresponds to the temperature driven structural change shown in Figure 50, but then there is a significant drop in apparent tritium retention $>$ 1500 K. This drop can be explained by considering reflection and desorption rates.

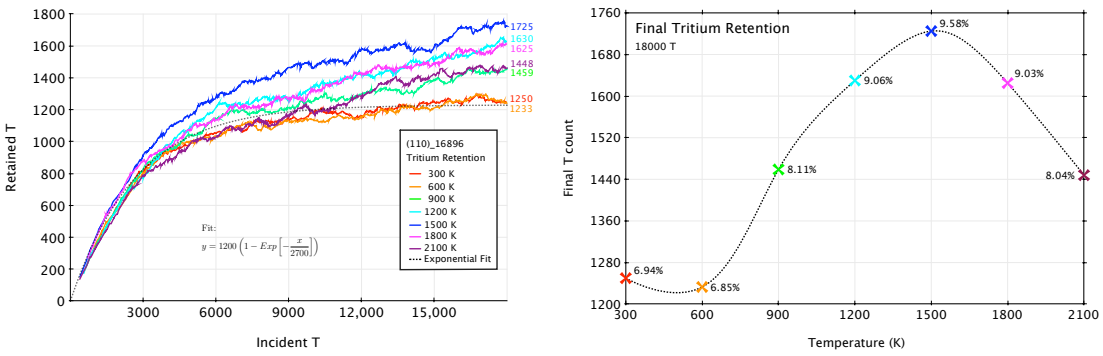

(a) (b)

Figure 53: Tritium retention - low-temperature (300 and 600 K) structures saturate at about 1200 retained atoms. Above 600 K there is a sharp increase in retention, peaking at 1500 K and then decreasing.

Tritium will leave the system by either reflection, desorption or be sputtered as part of a hydrocarbon molecule. In these simulations, a particle/molecule is considered as reflected if found >10 Å above the surface by the end of the impact run ($\sim$3 ps) and is, or contains, the incident tritium atom, otherwise it is classed as

desorbed. This reflection rate will clearly be dependent on surface structure, since a disordered surface will be less dense and regular, thus allowing the incident ion access to deeper impact sites. Figure 54 shows two plots relating to tritium retention over three periods: up to a fluence of 6000, up to a fluence of 18000 and the period between 6000 and 18000 (*i.e.* retention during saturation/initial damage, total retention and retention post-saturation/damage). The most important is the third period, post-initial damage, since this more accurately represents something closer to a steady-state situation. Over such short simulation times (∼5 ns) it is important to distinguish between effects of the initial ideal surface and the damaged surface.

In understanding thermally activated mechanisms it is necessary to examine relative dissociation energies of the atoms/molecules involved. Figure 55 shows temperatures at which various bond types are likely to be broken by thermal vibrations and thus result in desorption. This is evaluated using an Arrhenius rate equation.

$$R_{desorption} = \nu \mathrm{Exp}\left[-\frac{E}{k_B T}\right] \tag{42}$$

For a given temperature, T, the exponential term is proportional to the fraction of atoms in a Maxwell-Boltzmann distribution that will have kinetic energies greater than E, the activation energy of desorption, taken here to be the bond energy as evaluated by the simulation code used throughout these simulations. Although this energy may not necessarily be the dissociation energy required to break a bond in individual dynamic environments, it is a good guide to threshold temperatures above which one may expect significant desorption. What is considered as a 'significant' desorption rate ($\mathrm{R}_{desorption}$) is arbitrarily taken to be anything corresponding to above about 10% of all particles after one minute. Since rates rapidly rise (shown by the closeness of the 10%, 20% and 30% lines in Figure 55) once $E \approx k_B T$, this seems an appropriate figure to take. The prefactor, ν, is interpreted as a temperature-independent attempt frequency based on the assumption that bound atoms vibrate at about 10^{13} times per second.

In Figure 55 bond-energies are quoted for C-T and C-C bonds (dashed red and solid blue lines respectively). Carbon to carbon bonds are evaluated for diamond like and graphite-like structures as 3.7 and 5.5 eV. What is important regarding desorption, are the bond energies for hydrocarbon molecules and tritium atoms bound to surface carbon atoms. The lowest bond energy of 3.2 eV is for a tritium bound to a carbon which is otherwise sp^3 bonded to three neighbouring carbons and cor-

responds to an activation temperature just below 1100 K. A similar temperature has been noted before as a threshold for thermal desorption [81]. Where the surface carbon atom is not bound to three other carbons but more tritium atoms, maintaining a neighbour count of four, the C-T bond becomes much stronger (about 4.4 eV) and relates to a temperature of about 1430 K. Bonds between tritium and carbon where the carbon has only two or one other carbon neighbours are at about the same energy. The weakest bound hydrocarbon molecule to a surface carbon is a CH_3 which has a C-C bond strength of about 3.9 eV and corresponds to a temperature of about 1260 K. Less saturated molecules, CH_2 and CH_1, are progressively stronger with C-C energies of 5.3 and 6.0 eV respectively. It is this threshold temperature of 1430 K for tritium bound to surface carbons that gives rise to the increase in atomic reflection/desorption seen in Figure 54 and thus the decrease in net tritium retention above 1500 K. Pospieszczyk *et al.* [53] found that for graphite at wall temperatures above 1300 K thermal release of hydrogen is dominantly in its atomic form.

Figures 54a, 54c and 54e show the combined amount of tritium reflected and desorbed as either molecular or atomic tritium (T_2 or T). A common feature to the plots is a minimum. This is at 1500 K for 6000 tritium and 1200 K for 18000. It is the reflection/desorption minimum of the 6000 tritium curve which gives rise to the local maximum seen in Figure 54e at 1500 K, even though the post-damage minimum is clearly at 1200 K. This shift to a lower temperature maximum for post-damage retention may simply be due to weaker C-T bonding with increased saturation and reduced incident energy dissipation amongst surface atoms due to lattice damage. On breaking these figures down into reflected and desorbed components the cause of these minima is apparent. Figures 54b, 54d and 54f show this and are weighted so that a T_2 molecule counts twice as much as a T atom. Generally, the amount of tritium reflected/desorbed as single atoms is at least twice that as for molecular tritium. Also, with increasing temperature, the amount of reflected material decreases whereas the amount of desorbed material increases.

The reflection rate is strongly dependent on surface condition and in this respect is a secondary effect of an increasing substrate temperature. For example, there is a much larger atomic reflection rate for the pre-damaged period, a feature of the early bombardment of a clean, ideal diamond surface. The desorption rates, however, generally have the same form for both pre- and post-damage periods. This suggests a dominant dependence on substrate temperature rather than surface structure, although the two influences are difficult to separate.

With increasing temperature reflection rates decrease and desorption rates in-

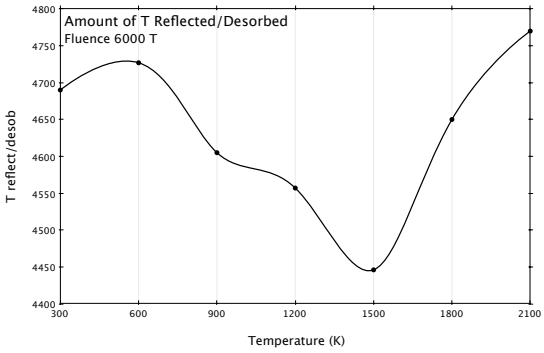

(a) Pre-damage period (Fluence < 6000)

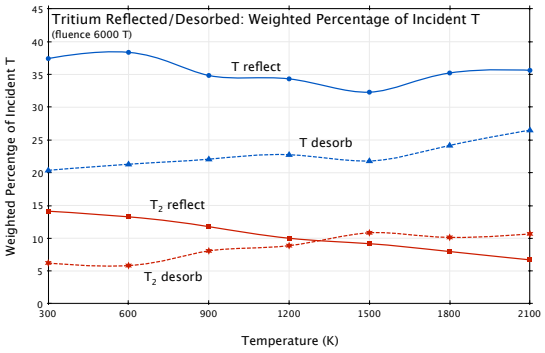

(b) Pre-damage period (Fluence < 6000)

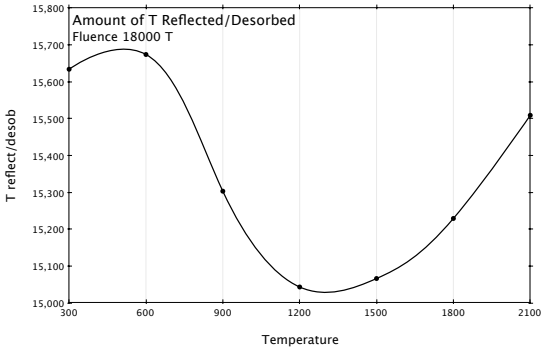

(c) Total (Fluence < 18000)

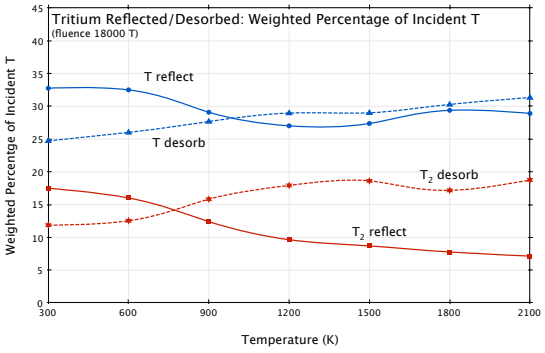

(d) Total (Fluence < 18000)

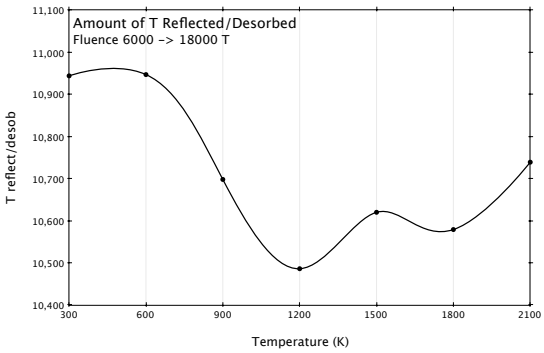

(e) Post-damage period (Fluence > 6000)

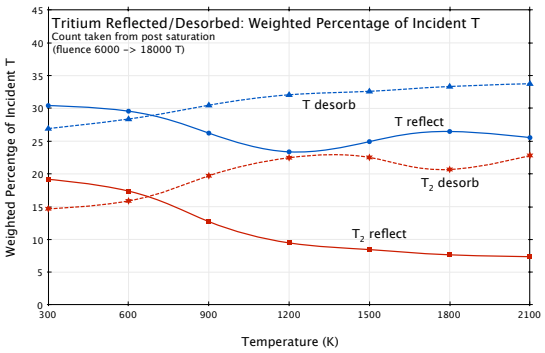

(f) Post-damage period (Fluence > 6000)

Figure 54: Reflection/desorption curves. Left: Net. Right: Reflection and desorption shown separately for T and T_2. With increasing temperature, a decreasing reflection rate (due to structural damage) and an increasing desorption rate (due to thermal activation) results in the minima seen in the figures on the left.

crease. A small step exists in this otherwise gradual trend which corresponds to the structural change quantified in Figure 50. A larger drop in reflection rates compared with the increase in desorption at this point leads to the net increase in tritium retention seen above 600 K. This is a feature common to the atomic, T, and molecular, T_2, yet for the former there is an increase in both reflection and desorption above

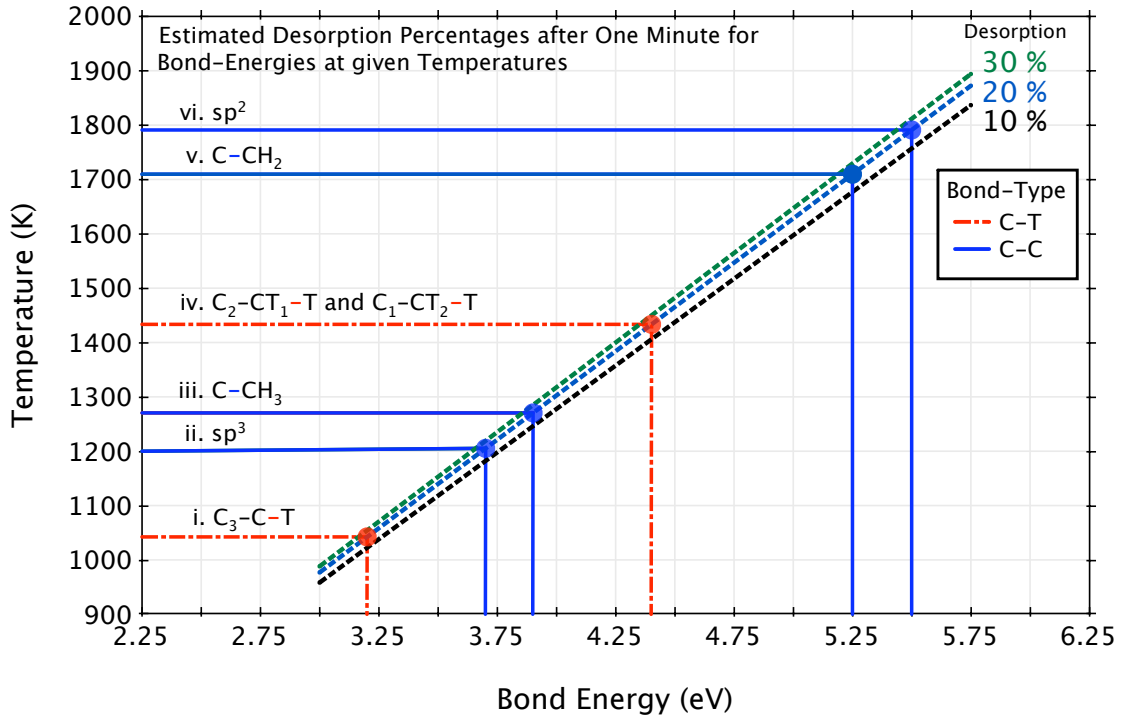

Figure 55: Temperatures at which desorption rates become significant (>20%) after one minute for various bond-energies based on Equation 42. As evaluated by the MD code used in these simulations and in order of increasing bond energy, they are: *i.* The T-C bond of a tritium atom bound to an otherwise sp^3 bonded carbon (whose other neighbours are carbon atoms) is of about 3.2 eV and corresponds to a temperature of about 1050 K.
ii. At 3.7 eV is the C-C bond between two sp^3 atoms (which have only carbon neighbours, *i.e.* diamond-like) this is 1200 K.
iii. For the C-C bond between a CT_3 molecule and a carbon atom (irrespective of that C atoms neighbour environment) this is 3.9 eV and a temperature of 1260 K.
iv. At 4.4 eV and 1430 K is the C-T bond energy where the carbon atom has four neighbours (as in the first bond quoted, *i.*) but the other three are not all carbon. C-T bonds where the carbon atom has only three and two neighbours have similar energies of 4.55 and 4.51 eV respectively.
v. The C-C bond connecting a CT_2 molecule is about 5.25 eV, closer to the sp^2 bond strength (compare with bond *iii.*), and relates to a temperature close to 1700 K.
vi. The strongest bond is between two sp^2 bonded carbons whose neighbours are carbon (*i.e.* graphite-like) at 5.5 eV and corresponds to a temperature of 1800 K.

1500 K. As noted above and in Figure 55 line *iv*, this high temperature increase is primarily due to the enhanced thermal desorption of tritium bound to various carbon complexes. This increase in desorption (and thus decrease in 'sticking rates') gives rise to the net decrease in retention seen above 1500 K.

6.4 Sputtering

Sputter yields are important, not just in monitoring structural damage, but also because sputtered material may contaminate the plasma itself and redeposit on the reactor inner wall, potentially enhancing tritium retention.

As with tritium retention trends, there are clear before and after surface-damage periods, again about the 6000 incident tritium mark. Following initial damage, sputter yields in terms of carbon loss settle into linear trends with continued bombardment. Figure 56a shows the remaining number of carbon atoms of the original 16896. Final carbon counts are shown in Figure 56b. In general the higher temperature samples sputtered more carbon than the lower temperature, also there is a local maximum in the curve at 1500 K and what appears to be the beginning of a sputter decrease at 2100 K. The shape of the curve closely resembles that of the tritium retention levels, or rather the level of tritium not retained, specifically for the post-damage period (Figure 59f).

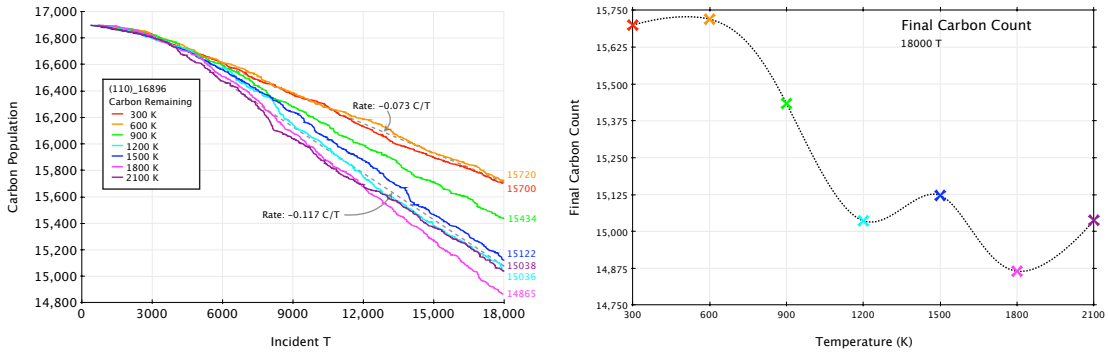

(a) (b)

Figure 56: a) Amount of carbon remaining of the original 16896 atoms as bombardment progresses. Linear sputter rates develop after a fluence of about 6000 ions. b) Final carbon count for the different temperatures. Generally the more material is lost for the graphite-like high temperature cases than for the low temperature cases where the diamond lattice remains largely intact.

The most common species of hydrocarbon sputtered, in terms of molecule count and mass, contained a single carbon atom, and progressively larger molecules were less frequent. From Figure 57, it is clear that it is these single carbon molecules which dominate the carbon sputtering process as larger molecule counts remain comparatively similar for pre and post-damage samples despite the temperature increase. As with the tritium desorption curves (Figure 54f) there is a sharp increase in C_1H_y yield for temperatures above 900 K.

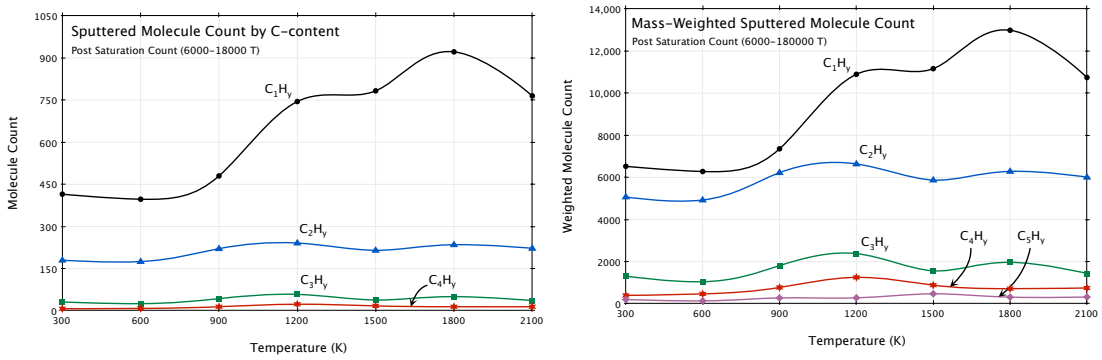

(a) (b)

Figure 57: Sputtered C_xH_y molecule type. a) Molecule count. b) Mass weighted count

Mostly, within the 0.3 ps time period in-between successive bombardments, hydrocarbon molecules sputtered did not contain the incident tritium atom (compare counts in Figures 57a and 58a). Although an incident ion need not be combined with the sputtered molecule, and the sputtering due to bombardment rather than desorption may take a little longer than the allowed 0.3 ps, it is interesting to note a decrease in 'reflected' hydrocarbon molecules above 1800 K (Figure 58a). Absent from the reflected hydrocarbon graph (Figure 58a), but seen in the sputtered molecule count (Figure 57a), is the enhanced sputter yield at 1200 K. This is due to a combination of structural change and the increased desorption rates above this temperature as evaluated in Figure 55. These desorption threshold-temperatures play a large role in sputter yields, seen in the difference in count scales for Figures 57 and 58, from hundreds for desorption to tens for reflection respectively.

On the whole, however, comparatively little tritium is removed from the surface via hydrocarbon sputter/desorption, as compared with atomic and molecular desorption (roughly only one sixth of net tritium not retained). The amount of tritium in ejected hydrocarbons is shown in Figures 59a, 59c and 59e (compare with T and T_2 Figures 54a, 54c and 54e) and shows a clear maximum as with previous graphs, but with hydrocarbon tritium content sputtered roughly the same at the two temperature extremes. This is because with increased temperature there is an increase of carbon sputtered (Figure 57) yet the saturation of these molecules (Figure 58b) reduces due to enhanced surface desorption.

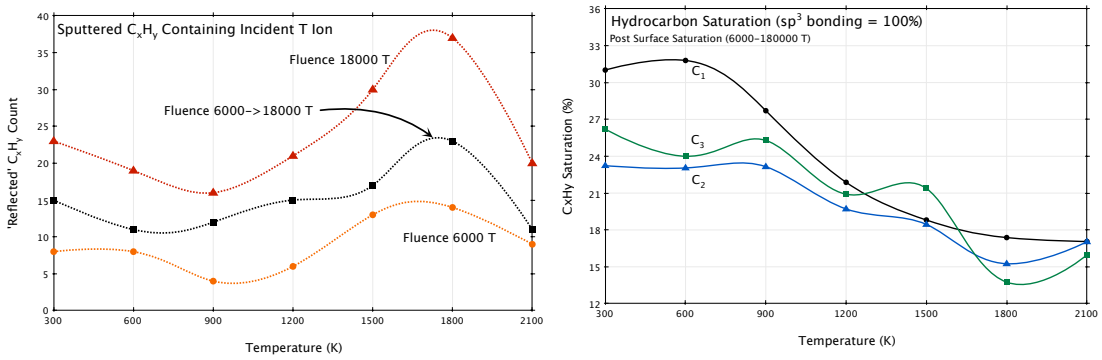

(a) (b)

Figure 58: a) Sputtered molecule count where incident tritium is part of sputtered product. b) Sputtered molecule tritium saturation, taking all carbon atoms as having a coordination of four as 100%

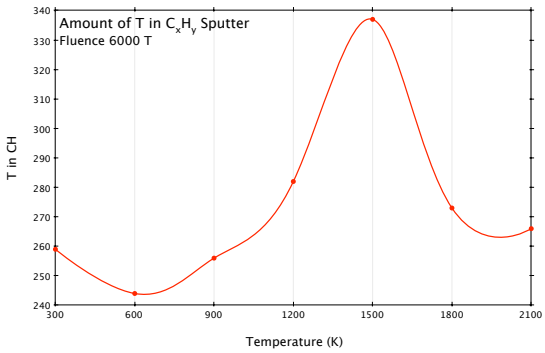

(a) Pre-damage period (Fluence < 6000)

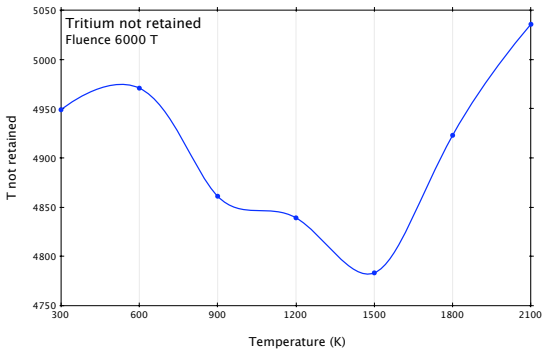

(b) Pre-damage period (Fluence < 6000)

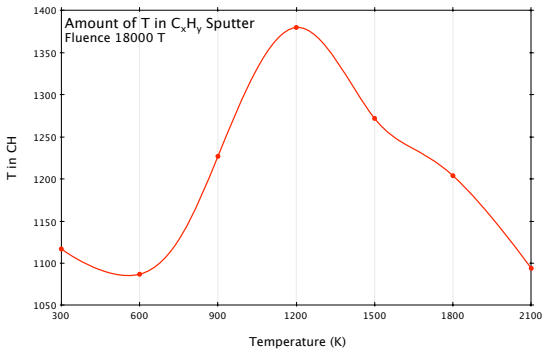

(c) Total (Fluence < 18000)

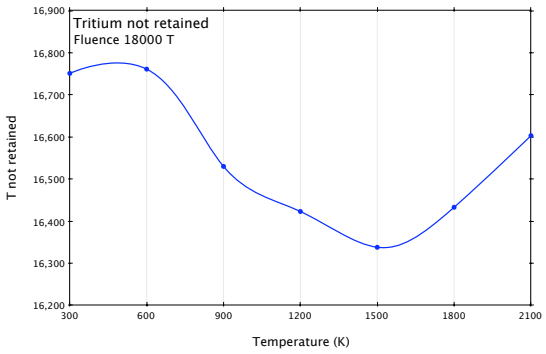

(d) Total (Fluence < 18000)

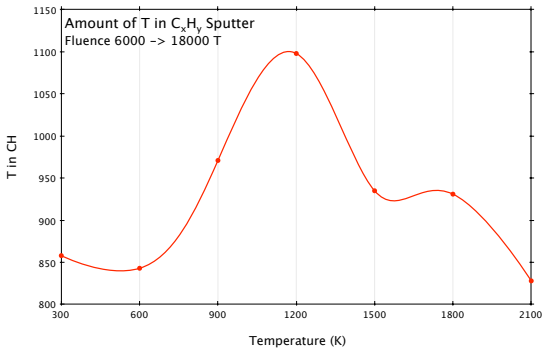

(e) Post-damage period (Fluence > 6000)

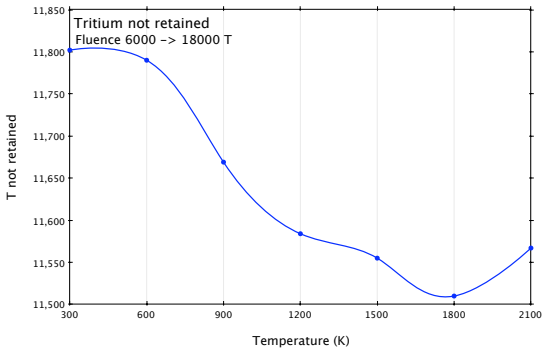

(f) Post-damage period (Fluence > 6000)

Figure 59: Left: Amount of tritium sputtered via hydrocarbons strongly correlates with tritium refection/desorption levels (*i.e.* surface saturation) shown on the left of Figure 54. Right: Net effect of reflection, desorption and hydrocarbon sputter on tritium retention. Figure 59d corresponds to Figure 53b showing final retention

6.5 Diamond Etching Mechanism

Figure 51 shows a strong diamond structure remaining immediately below the tritium retention region for low temperature (< 900 K) bombardment. This residual structure is largely responsible for lower tritium retention and sputter yields and can be explained by examining how damage develops with time. Figure 61 shows the build-up and erosion of tritium with time. Tritium is able to penetrate deeper only as upper layers are eroded but is still generally confined to inter-layer positions as much of the diamond structure remains. This gradual layer-by-layer erosion and the lack of any evidence for tritium diffusivity through the diamond lattice confines retention and structural damage to the top four to five diamond layers only.

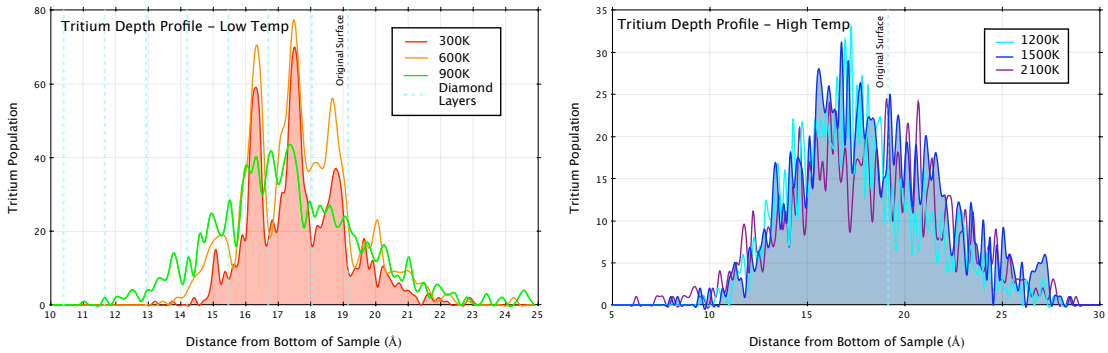

(a) (b)

Figure 60: Tritium penetration with temperature after fluence 18000 T a) At low temperatures the diamond structure prevents deep penetration and causes retained tritium to gather in between diamond layers. b) At higher temperatures the diamond structure is lost and tritium penetrates much deeper and is not confined to inter-layer positions.

Recent experimental evidence has reported that on exposure to a plasma, diamond will form a thin amorphous hydrocarbon layer at the surface above a surviving diamond structure [64]. Results of simulations presented here concur that, although material is eroded, the damage due to low energy (15 eV) bombardment is confined to the surface. It also appears that the depth of this damage remains roughly of a constant thickness as diamond layers are successively eroded. This layer-by-layer mechanism is responsible for limiting the tritium retention to what the damage region can accommodate in satisfying carbon sp^2 bonding and for preserving a diamond structure below. Considering this, it is possible that what Porro *et al.* [64] identified as an amorphous layer based on Raman spectroscopic observations of sp^2/sp^3 concentrations could still in fact retain a certain amount of the

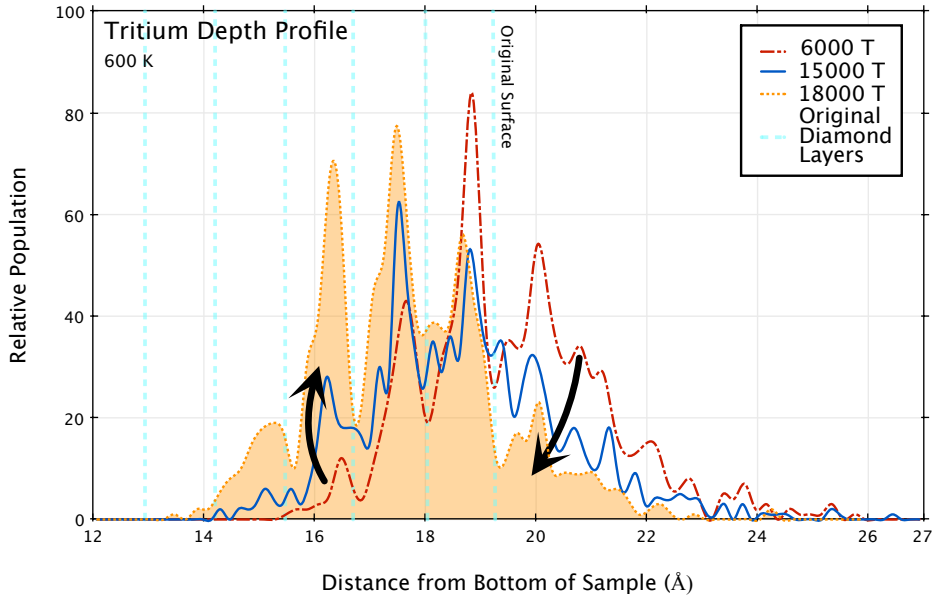

Figure 61: Tritium depth profile of the 600 K sample at different fluences. Tritium gathers initially at the surface and below the first two diamond layers. As carbon material is sputtered from these layers the tritium is able to penetrate deeper and so can accumulate behind successively deeper layers. This layer-by-layer etching means the remaining diamond structure below the damaged region localises damage and thus tritium retention to the surface.

original diamond structure (Figure 51c).

Limiting structural damage of the diamond lattice to near the surface will mean that the exceptional thermal properties for which diamond would be a desirable plasma-facing material would remain for the bulk of the material. Specifically, the rapid transfer of heat away from the surface would help limit further thermally induced structural damage such as graphitisation or amorphisation.

6.6 Chapter Summary

The dependence that tritium retention levels and sputtered products of diamond have on substrate temperature was studied under a fixed tritium flux (10^{29} ions $m^{-2}s^{-1}$) and incident ion energy (15 eV). The surface bombarded was initially diamond, but due to the temperature range covered (300-2100 K) reconfiguration to the diamond structure due to thermally induced graphitisation occurred above about 1000 K (Figure 50). Therefore, with increased substrate temperature, not only are thermally activated desorption barriers crossed (Figure 55) but also the nature of the structure bombarded is radically different (compare Figures 46 and 49). The

combination of these two features can be seen in many of the above figures. The structural change is evident where there is a sudden change above 1000 K (for example in the total sputtered hydrocarbon count in Figure 57), and thermal thresholds, such as those outlined in Figure 55, can explain features such as the rapid decrease in tritium retention above 1500 K (for example Figure 59b).

At temperatures below 1000 K much of the diamond structure remains intact despite the surface bombardment (Figure 51). Those carbons near the surface also show a preference to form sp^2 bonding (Figure 51d). The fact that it is these carbons which later sputter, producing under-cordinated hydrocarbon molecules, contradicts the assumption of Horn *et al.* [28] that it is the sp^3 surface radicals which lead to sputtering (Figure 11). This could however be a feature of the high fluxes and short simulation times used here. Despite this, the remanence of these carbons in the original diamond positions, even within the damaged region, causes retained tritium to build-up between the original diamond layers. Only as upper layers are gradually eroded away do deeper layers become accessible, in effect limiting the retentive layer to about 6 Å. The result of this is a layer-by-layer erosion mechanism (Figure 61) and the concentration of retention to the upper few diamond layers. Only with the onset of a thermally induced structural phase change does the depth of this retentive layer increase. Practically, in a fusion environment, confinement of retention to the upper surface would not only limit damage to the material itself but could also facilitate easier tritium reclamation on cleaning.

7 Graphite Tritium Bombardment

In Chapter 6 cumulative tritium bombardment simulations were run on diamond (110) surfaces over a range of substrate temperatures. At higher temperatures desorption rates for various bond-energies become important factors affecting sputter yield and tritium retention. In addition to this, as explored in Chapter 5, at temperatures above about 1000 K the diamond structure begins to undergo a phase-change, reconfiguring diamond-like sp^3 bonding to graphite-like sp^2 hybridisation. Although sp^2 bonds are stronger than sp^3, the tetrahedral diamond structure enhances carbon's physical properties and, as demonstrated above, plays a major role in confining damage due to bombardment and thus tritium retention to the upper surface. Section 6 discusses these features and relates them to the structural change due to substrate temperature. In this section those structural differences are compared with each other at similar temperatures. Whereas in Section 6 what is referred to as graphite-like and compared against diamond is also at a higher temperature, here a diamond sample is first thermally graphitised and then cooled back down to substrate temperatures desired before bombardment.

7.1 Method

The graphite samples bombarded in this section were taken from Section 5 which studied thermally induced phase-changes. The clean (110) diamond surface was heated to 3000 K over 5 ps increments of 34 K. The under side of the diamond slab was frozen to a depth of 4 Å ensuring there was in effect only one surface. The processes of bombardment and analysis were identical to those described above for diamond in Section 6.1.

The purpose of this section is to compare the bombardment of diamond and graphite-like surfaces at the same substrate temperature. The choice of a suitable graphite sample is complicated due to significant differences between different crystal orientations. For example, the ideal graphite inter-layer spacing of about 3.35 Å is quite large in comparison to these sample sizes. Since it was the diamond (110) surface bombarded above in Section 6, graphitised (110) samples from Section 5.3 were an obvious choice. Although these did not 'cleanly' graphitise, preferring instead a herring-bone formation (Figure 62), pretty much all free (non-frozen) atoms formed sp^2 bonds and clearly not in a random amorphous structure. Of all 16896 carbon atoms, 3649 (22%) were frozen. The unfrozen region expanded vertically on heating reducing the sample density. As mentioned, this is not an ideal crystal and so may be expected to have a higher density than that reported for graphite. There

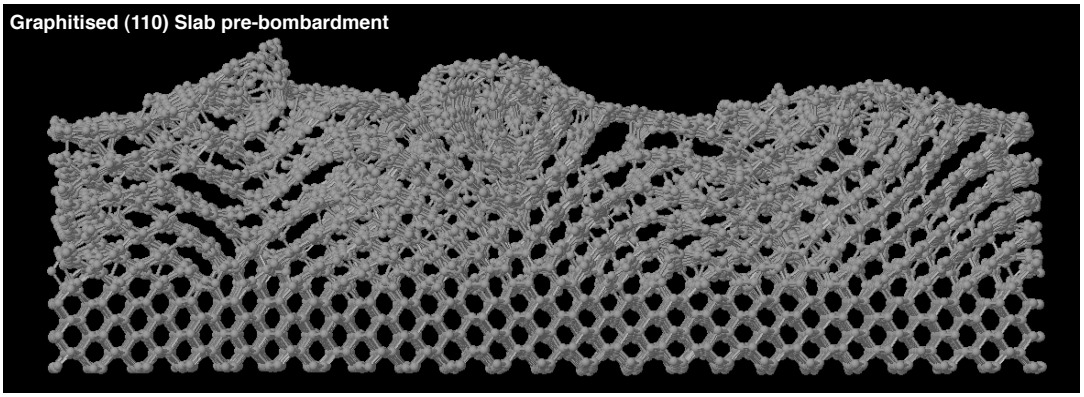

Figure 62: Graphitised slab pre-bombardment. The (110) diamond slab as initially heated to 3000 K and then cooled to desired substrate temperatures. The bottom 4 Å were frozen in the diamond configuration frozen (22% of slab).

is a spectrum of reported densities for real carbon structures depending on bonding ratios and structure (evident in the diversity of 'amorphous' carbon materials) but these roughly range from about 1.8 g.cm^{-3} for amorphous carbon to 2.3 g.cm^{-3} for graphite and 3.5 g.cm^{-3} for diamond. Although it is difficult to confidently extrapolate a density from such small, non-uniform MD samples, the initial graphitised structures used here were of a density of about 2.6 g.cm^{-3}.

7.2 Carbon Sputter and Tritium Retention

Since the stronger sp^2 bonding is stable over the temperature range studied here (300-2100 K), in contrast to the diamond sp^2 case, there is no real structural difference between the two temperature extremes. Because of this the carbon etching rate is similar for all temperatures (Figure 65a) with only a very slight increase with increasing temperature (Figure 65b), most likely due to surface carbons being slightly less tightly bound due to them having greater kinetic energy.

Figure 65b compares the final carbon counts at different temperatures for these graphite samples and the diamond samples from the above section. A steady-state etching rate was established for the diamond case after a fluence of about 6000 tritium (Figure 56a). For these graphite samples it takes longer for the rate of loss of carbon to settle (see Figure 65a). This is better seen in Figure 67a where the tritium saturation levels for the various temperatures are reached after a fluence of about 12000 tritium. It is, therefore, perhaps not a fair comparison to simply consider final carbon counts following a fluence of 18000 tritium for the two samples (Figure 65b). A better comparison of carbon sputter rates is to compare the amount of carbon lost after a fluence of 12000 tritium, once a steady-state erosion has been established for

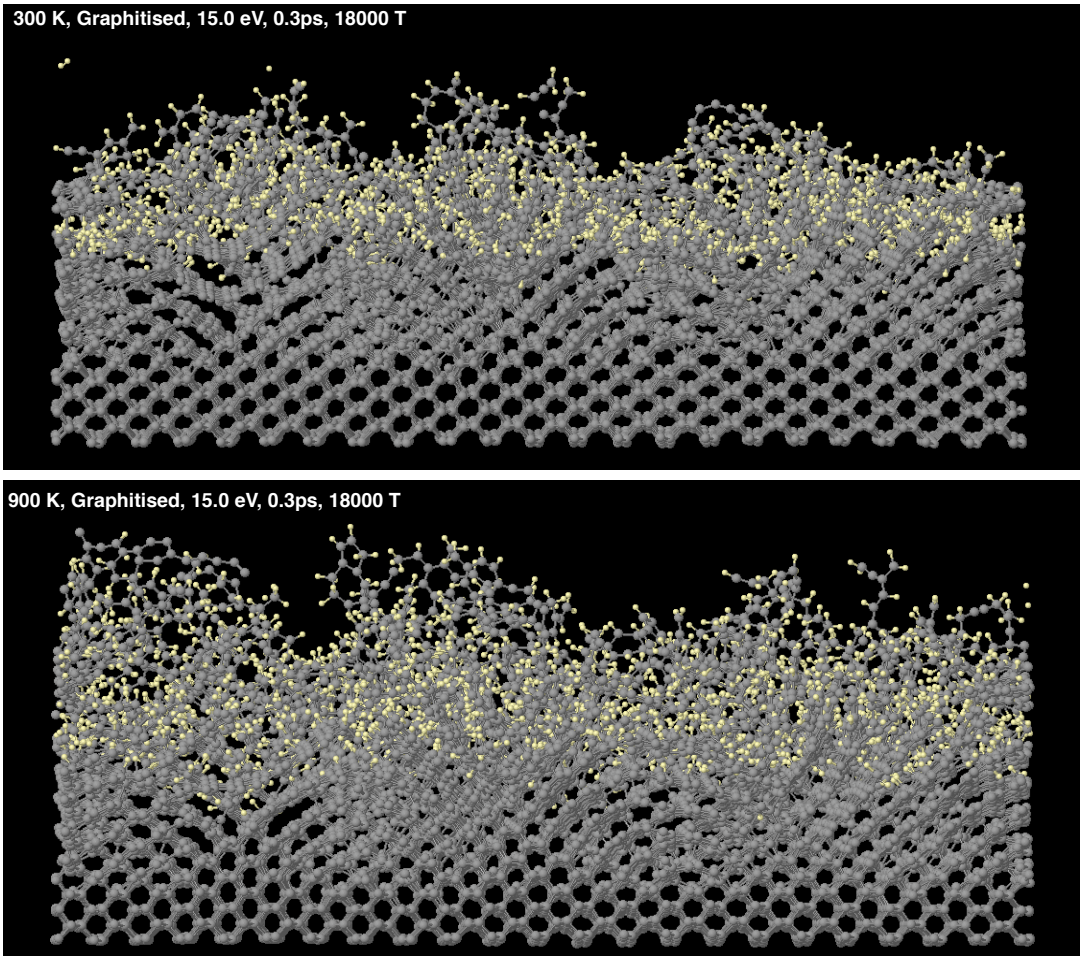

Figure 63: The graphitised sample at 300 K and 900 K following bombardment with 18000 tritium atoms.

all surfaces. This is shown for both the diamond and graphitised cases in Figure 66. Generally, sputter rates for both samples increase with temperature until about 1800 K when they begin to reduce. In the diamond case, there is also a distinct increase in sputter rate after 900 K. As discussed in Section 6.4, this increase for diamond is due to structural change (beginning of graphitisation) after about 1000 K. Before this temperature the graphitised surface sputter rate is about 20-40% more than the diamond surfaces. Above this temperature, the diamond sputter rates are actually greater than the graphitised, but they then converge for temperatures about 1500 K. This sharp increase for diamond above 1000 K was attributed to the thermally induced formation of sp^2 bonds at the surface, breaking confinement due to the diamond structure, and the increased thermal desorption of CH_3 radicals bound to the surface (Figure 55). Although the diamond structure does undergo the beginning of a phase change towards graphitisation, its density is still higher than that of the

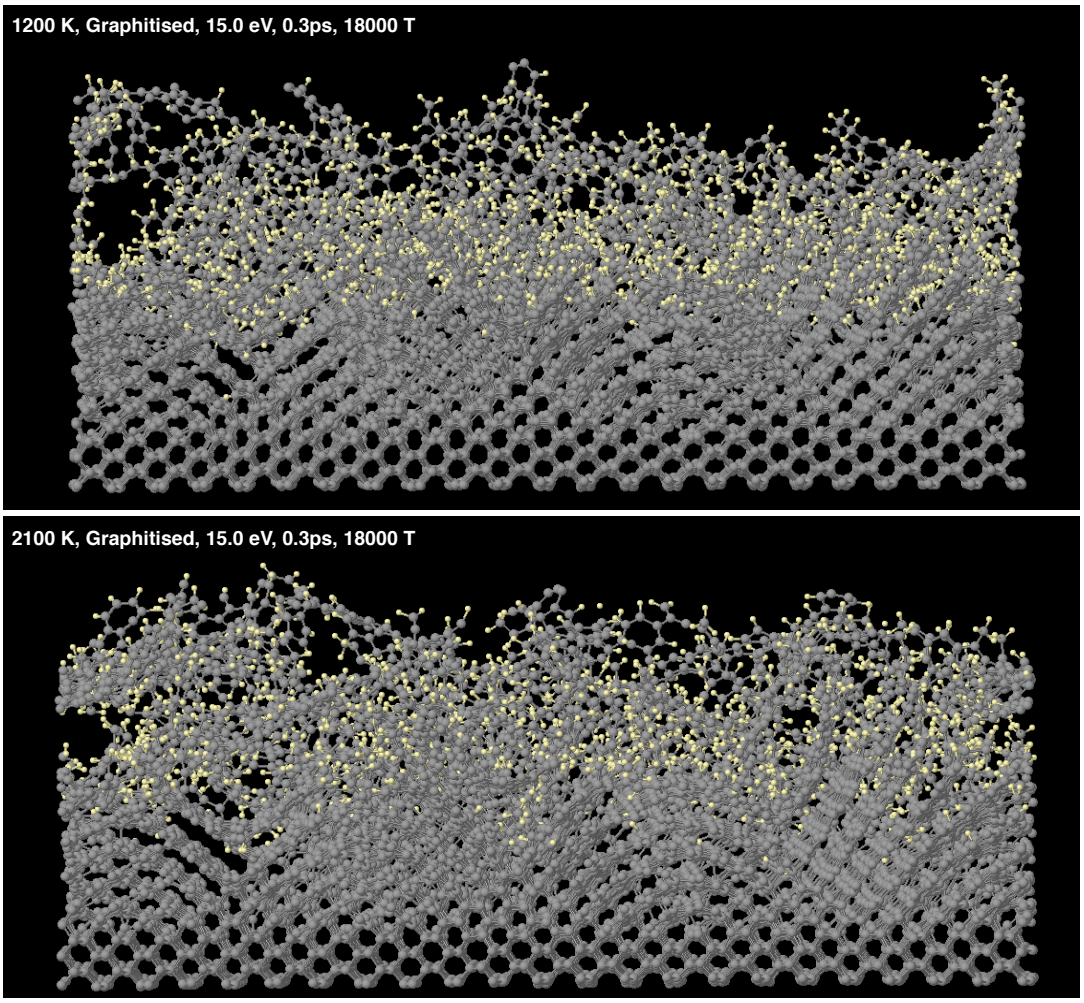

Figure 64: The graphitised sample at 1200 K and 2100 K following bombardment with 18000 tritium atoms.

graphitised samples (which were graphitised up to a temperature of 3000 K) which leads to a greater tritium concentration at the surface and thus the presence of more tritium saturated carbons. As the graphitisation of the diamond surface becomes more complete the sputter rates converge.

There is a much clearer distinction between the two surfaces in terms of tritium retention. In Section 6.3, the remaining diamond structure beneath a surface-damage region was attributed with limiting total tritium retention and confining it to the surface, even at higher temperatures (> 1000 K) where the upper part of the slab begins to graphitise. In the absence of that residual diamond structure tritium is able to penetrate deeper and so the surface is able to accommodate more before it saturates. This is shown in Figure 67b which plots final tritium retention levels. For

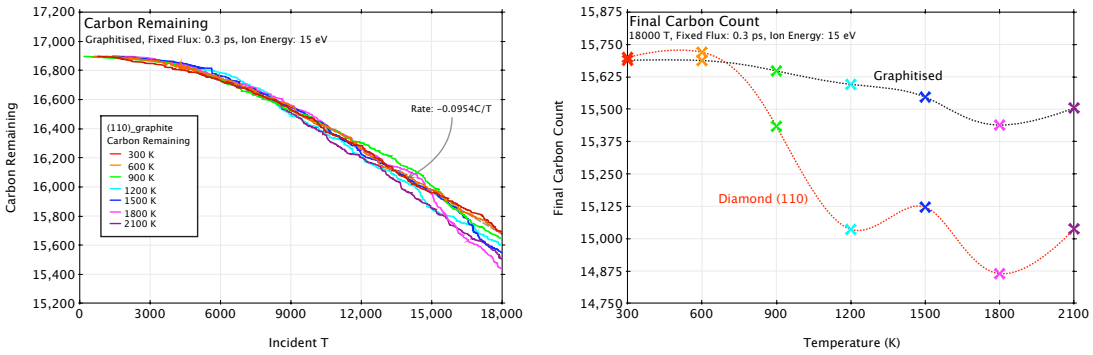

(a) (b)

Figure 65: a) Carbon count during bombardment. Loss of material due to sputtering settles to steady rates after a fluence of about 12000 tritium. b) Final carbon count for the graphitised samples compared with those for the diamond samples (diamond line reproduced from Figure 56b).

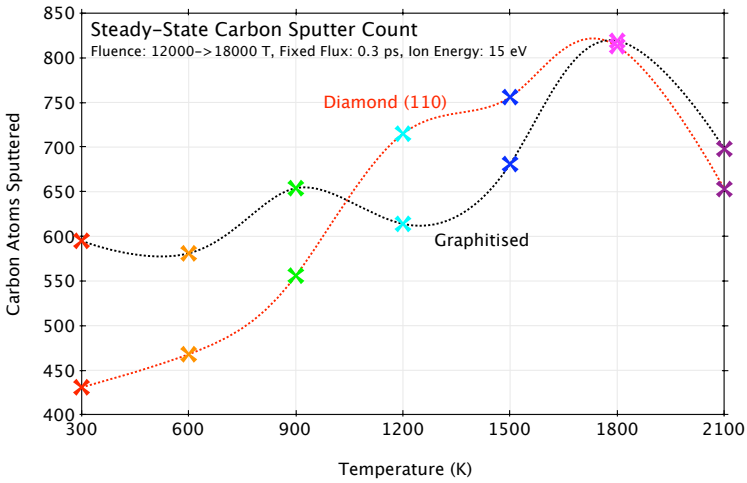

Figure 66: Amount of carbon sputtered after a fluence of 12000 tritium (*i.e.* once steady-state erosion has been established)

temperatures below 1000 K the graphite sample retained 50-75% more tritium than did the diamond surface. Above this, graphite still retained more than diamond, but this difference went from about 30% at 1200 K to 18% at 2100 K.

Generally, there is an initial increase in tritium retention with increasing temperature for both surfaces. The graphitised surface then gradually retains less for temperatures above 1000 K due to enhanced thermal desorption. For the diamond surface, the initial increase does not happen until about 1000 K, above which the surface gradually graphitises with higher temperatures. For both surfaces retention reduces above 1500 K where the thermal desorption of tritium bound to the surface increases significantly (see Figure 55).

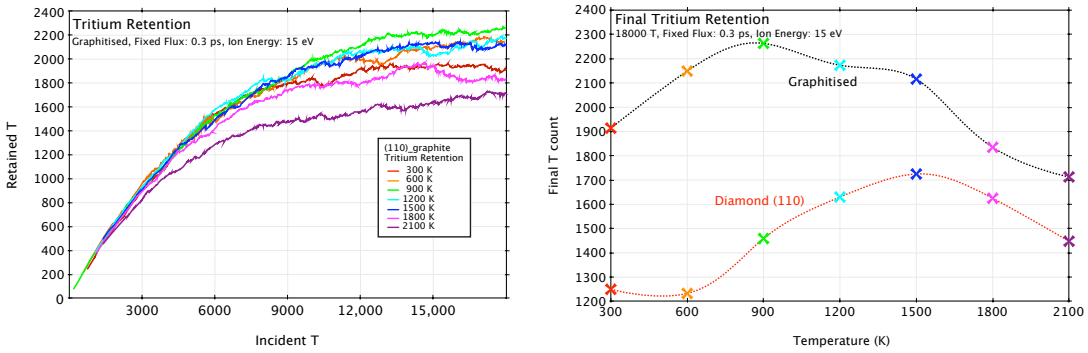

(a) (b)

Figure 67: a) Tritium retention during bombardment. The surface saturates at different temperatures after a fluence of about 12000 tritium. b) The final tritium count following a fluence of 18000 tritium. Graphite surfaces retain more than the diamond due to deeper ion penetration. Above 1500 K significant tritium desorption reduces the retention for both diamond and graphite.

7.3 Chapter Summary

In this section graphitised surfaces were exposed to tritium bombardment and compared against the diamond surfaces from the previous chapter. In the case of the diamond surfaces, residual diamond structure beneath a damaged surface region confined and limited tritium retention (Section 6.3). Without this structural confinement, tritium was able to penetrate deeper and so the graphitised surface at all temperatures studied here retained much more, up to 75% for the 600 K case (Figure 67). For temperatures below 1000 K, the graphite surfaces sputtered more carbon material than did the diamond. This will have consequences for tritium retention via hydrocarbon redeposition.

The depth of this tritium retention region for the diamond and graphite samples at 600 K is seen in Figure 68. Where the diamond structure remains beneath the damaged region, retention penetrates to a depth of about 6 Å (and in tidy peaks between the diamond layers, Section 6.5). For the graphitised surface at the same temperature this is closer to about 9 Å. In comparison, a recent experimental study on the retention of deuterium in hard amorphous hydrocarbon films at 650 K [82] found the development of a soft retentive layer on the surface to a depth of 14 Å. The erosion yield and product spectrum of surfaces have been found to depend strongly on the a-C:H structure [83, 84, 85].

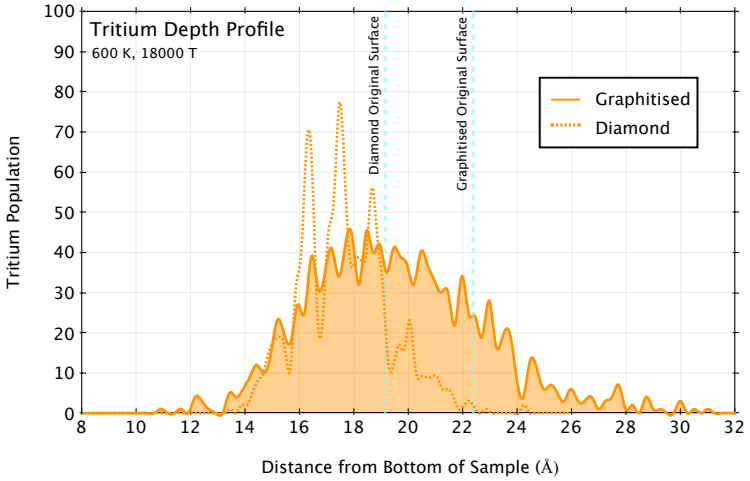

Figure 68: 600 K tritium depth profile for graphite and diamond following bombardment. The graphite surface retained approximately 75% more tritium and over a deeper retentive region.

8 Flux & Ion Energy Dependence

The net power load on the divertor will depend on two variables: the energy of incident ions and the rate at which they bombard. As stated above, for ITER this is expected to be a load of ∼10 MWm^{-2} [78] at energies 10-30 eV and ion fluxes of ϕ = 2-6 × 10^{24} ions $m^{-2}s^{-1}$. Various mechanisms to cool the plasma to this level are being considered, for example injecting impurities and reduced magnetic confinement.

Although incident ion energy may vary depending on design and operation mode, generally it is expected to be below the physical sputtering threshold (∼30 eV). It is therefore of interest to examine how, at a fixed flux and substrate temperature, diamond performs under bombardment over such a range of ion energies. As well as this, although the pico-second time-scales of molecular dynamics simulations restricts us to extremely high fluxes (∼10^{29} ions $m^{-2}s^{-1}$), well above what may be physically expected, it is also worth varying fluxes within our computational limit.

8.1 Method

The following simulations were conducted much as those from the above Chapter 6.1 where the effects of substrate temperature were investigated. Differences are that the thermostat no longer applies to the perimeter of the slab, but the region within 2 Å of the frozen atoms. The bombarded area was also extended to cover the whole surface (Figure 69). This in effect confines the heat-sink to the underside of the slab. The purpose of this was so that the temperature gradient in the z-direction, and thus thermal conduction of energy away from the surface, may also be observed.

Cumulative bombardment simulations of 18000 tritium ions were carried out on the (110) diamond surface examining, separately, the dependence on incident ion energy and flux on surface damage and sputter yield. These were all carried out at substrate temperatures of 300 K, well below graphitisation and desorption thresholds.

In examining the dependence of flux, the diamond surface was bombarded with 18000 15 eV tritium ions at intervals of 0.3 ps, 0.6 ps, 0.9 ps and 1.2 ps. Corresponding fluxes at these interval times are given in Table 8.1. Although these rates span only a comparatively small range considering that divertor fluxes are expected to be ∼10^{24} ions $m^{-2}s^{-1}$, it is clear from the wall times required to run these simulations that such physical fluxes are not currently possible with molecular dynamics of this scale.

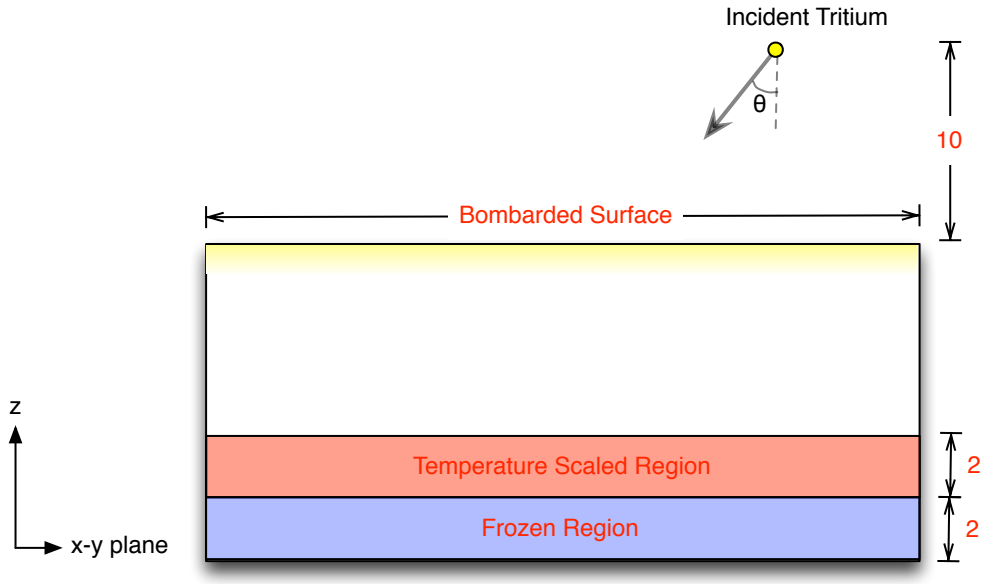

Figure 69: Schematic cross-section of a bombarded sample. Distances are labelled in Angstroms and not drawn to scale.

Interval Time (ps)	Ion Flux (ions $m^{-2}s^{-1}$)	Simulation Time (ns)	Wall Time (days)
0.3	7.05×10^{28}	5.4	13.5
0.6	3.52×10^{28}	10.8	26.0
0.9	2.35×10^{28}	16.2	38.3
1.2	1.76×10^{28}	21.6	51.1

Table 8.1 - Fluxes and total times simulated for 18000 bombardments of the entire (110) surface ($4.73 \times 10^{-17} m^2$) varying the interval time between consecutive impacts. Wall time taken for these simulations is also given for a job split over one quad-core processing unit (about the maximum number of cores in terms of efficiency due to scalability issues).

Simulations studying effects dependent on incident ion energy were carried out in a similar manner. Here, substrate temperature was scaled to 300 K and the interval time in between consecutive ion impacts was held fixed at 0.6 ps ($\phi = 3.52 \times 10^{28}$ ions $m^{-2}s^{-1}$, just over one third of the flux used in Chapter 6.1). Four cumulative bombardment simulations were run with tritium energies of 7.5 eV, 15.0 eV, 22.5 eV and 30.0 eV.

8.2 Incident Flux

Current experimental limitations mean that there is little data available for fluxes above about 10^{19} ions $m^{-2}s^{-1}$, whereas due to computational limitations simulations are rarely able to model fluxes below about 10^{28} ions $m^{-2}s^{-1}$. Divertor region fluxes are expected to be in between these two at about 10^{24} $m^{-2}s^{-1}$. Not only are simulations restricted to high fluxes, because of the computational costs only times scales of the nano-second order are possible. This limits the range of high fluxes which can be modelled. Despite this, this section looks at the dependence of sputter yield and tritium retention over the flux range available. In previous simulations in this thesis, tritium has bombarded surfaces at intervals of 0.3 ps and 0.6 ps. Here this is extended to 0.9 ps and 1.2 ps. Although this is however still a very narrow range of fluxes covered (all still of the order 10^{28} ions $m^{-2}s^{-1}$) and therefore its quite difficult to confidently extrapolate much of a trend from the data, this is still of interest and relevant to understanding the nature of the simulations themselves.

Four diamond surfaces were bombarded with 18000 tritium atoms at these interval times which correspond to total simulation times given in Table 8.1. Therefore it is worth bearing in mind that not only is the rate of incidence a factor, but also total simulation time as well.

The depth of damage and tritium retention appears to be independent of flux variation over this range (Figures 70, 71 and 72). There is also little diffusion into sample seen over larger time scales, although due to the rigidity of the diamond lattice, these times may still be too short of observe this. At this high flux regime, the sputter yield is proportional to the fluence rather than flux. This means that there is negligible background sputter and all material removed from the surface is directly due to the incidence of a tritium and not simply its presence at the surface. Figure 73a shows that over this flux range the amount of hydrocarbon sputter containing the incident ion increases and then levels off after 0.9 ps. This does not necessarily mean that more sputtered material contained the incident ion, but rather that this interval time is comparable to the time taken for the ion to sputter material. Thus what has previously been generally classed as desorption is not necessarily independent of the incident ion. Because net tritium retention does not change over this range this suggests that it takes a maximum of about 1 ps for the incident ion to to induce a surface hydrocarbon to sputter. Interestingly the percentages of reflected and desorbed atomic and molecular tritium (Figure 73b) level off earlier, by about the 0.6 ps interval time. Assuming that the time taken for an incident ion to simply be reflected from this height above the surface (10 Å)

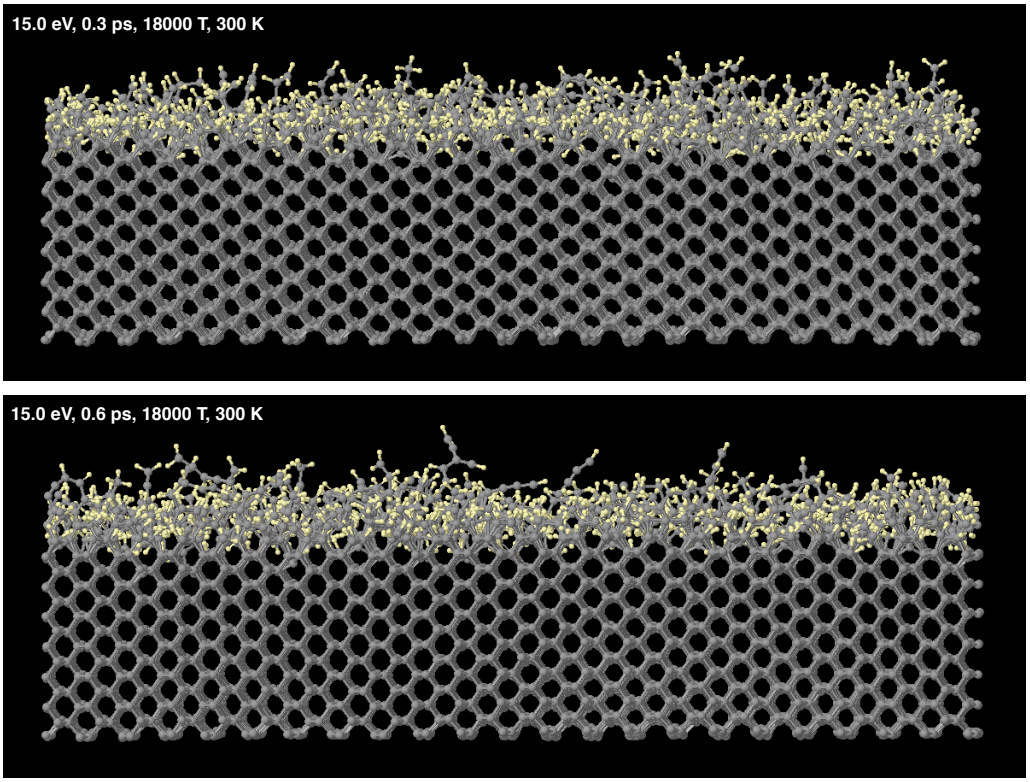

Figure 70: Final surfaces following bombardment of diamond at 300 K with tritium at intervals of 0.3 ps and 0.6 ps. There is little obvious difference between the two.

is about 0.6 ps and the time taken for an incident ion to sputter a hydrocarbon is about 1 ps, this suggests that the time taken for the ion to chemically interact at the surface is on average about 0.4 ps.

Although the total amount of carbon sputtered due to bombardment remains the same for the four fluxes, with increasing interval time (decreasing flux rate) there is a small decrease in the amount of single carbon atoms sputtered which is matched by an equal increase in the amount of carbon sputtered as double carbon molecules (Figure 74b). With increasing interval time there is also an apparent increase in the saturation of the hydrocarbon molecules and so the amount of tritium sputtered as part of a hydrocarbon molecule (Figure 75). This is the case even for the single carbon molecules despite its noted decrease in yield. The increase in tritium leaving the surface as part of a hydrocarbon molecule is matched by a decrease in the total amount of atomic or molecular tritium either desorbed or reflected (Figures 76a and 76b respectively).

These observed trends with flux are possibly linked to the mobility of tritium already at the surface. With increasing interval time surface tritium atoms have longer to find more stable and stronger bonding situations before they are bom-

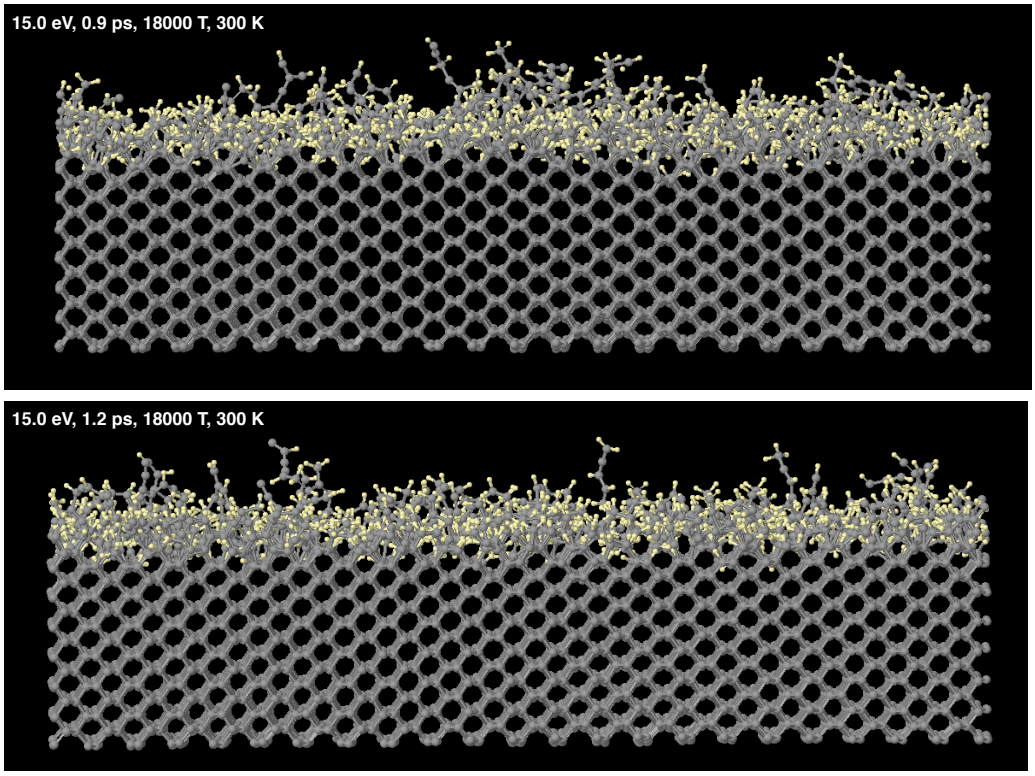

Figure 71: Final surfaces following bombardment of diamond at 300 K with tritium at intervals of 0.9 ps and 1.2 ps. There is little obvious difference between the two.

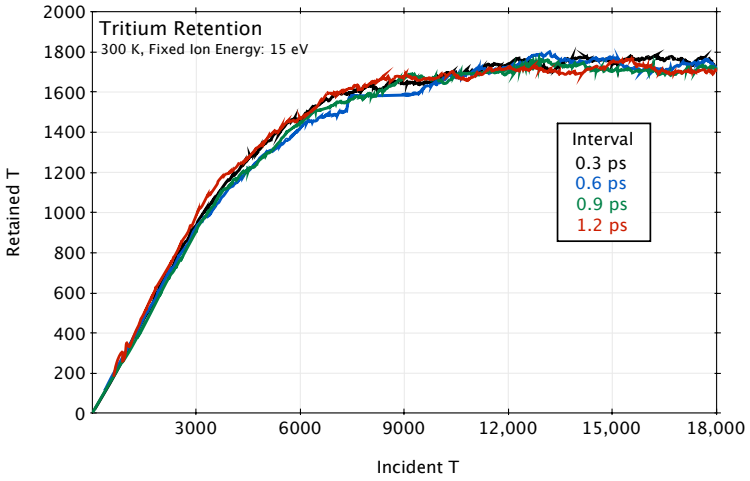

(a)

Figure 72: Tritium retention. All surfaces saturated after a fluence of about 9000 tritium. These retention profiles are virtually indistinguishable and suggest no dependance on flux over this range.

barded by another tritium. With the gradual increasing of average bond strength less atomic or molecular tritium is released (Figure 76b), which is dominantly due

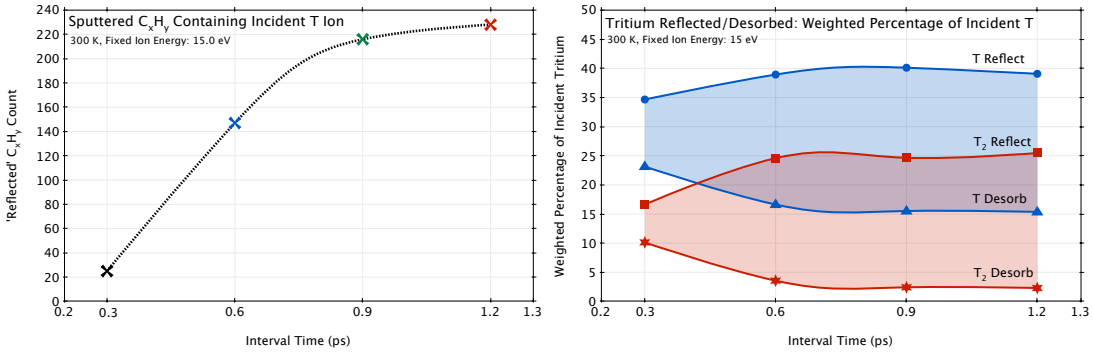

(a) (b)

Figure 73: a) Amount of hydrocarbon material to be sputtered within the given incident interval time. This levels off after about 1 ps suggesting that this is the maximum time taken to sputter material from this bombardment height. b) Percentage of incident tritium that was either reflected within the interval time or desorbed as either atomic or molecular tritium. These values level off after an interval time of about 0.6 ps. The net amount of tritium leaving from the surface without being bonded to a carbon atom remains about the same, corresponding to the constant level of tritium retention seen for the four fluxes.

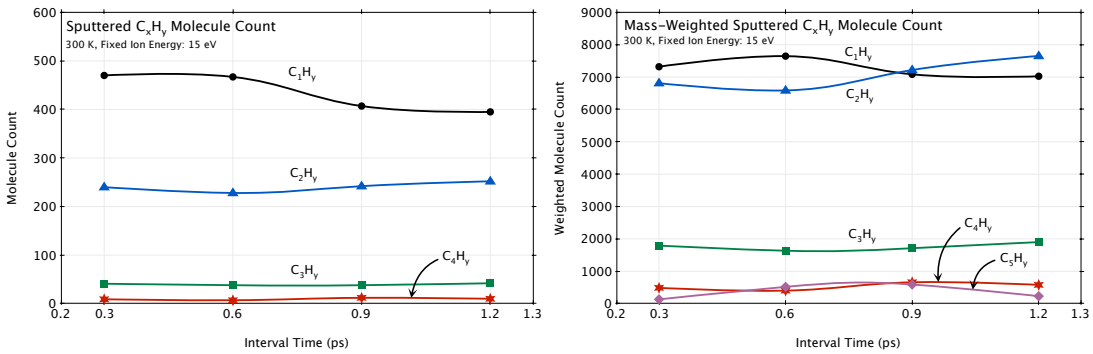

(a) (b)

Figure 74: a) A breakdown of the hydrocarbon sputter yield. With increasing interval time there is a slight increase in single carbon sputter at the expense of the double carbon sputter. b) The same data but weighted for molecule mass illustrating the constant net yield for the four fluxes.

to a drop in atomic release (Figure 77). If the tritium is not released in its atomic or molecular form but remains bonded to surface carbons, then it makes sense that when these carbons are sputtered, they have a greater tritium saturation (Figure 75). A slight increase in surface carbon saturation could also be responsible for the increase in double carbon molecule yield at the expense of the single carbon yield, since in the presence of more tritium adjacent carbons are less likely to reform a

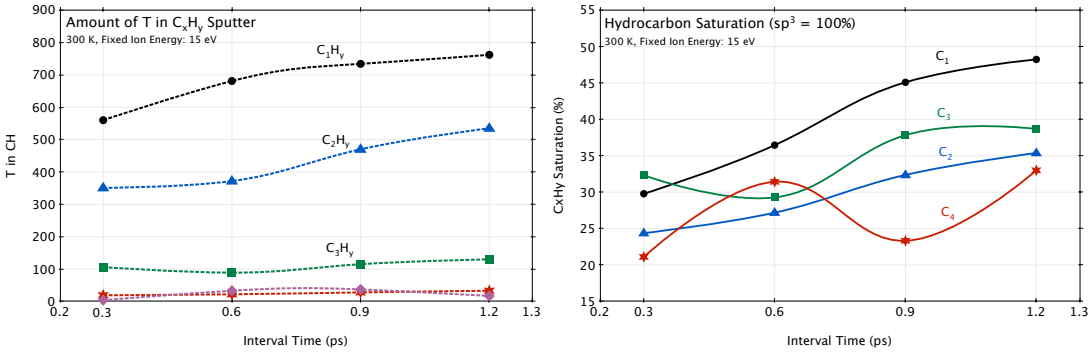

(a) (b)

Figure 75: a) The amount of tritium sputtered as part of a hydrocarbon molecule. b) Saturation of the sputtered hydrocarbon molecules. Both figures illustrate the increase in tritium content with increasing interval time (decreasing flux).

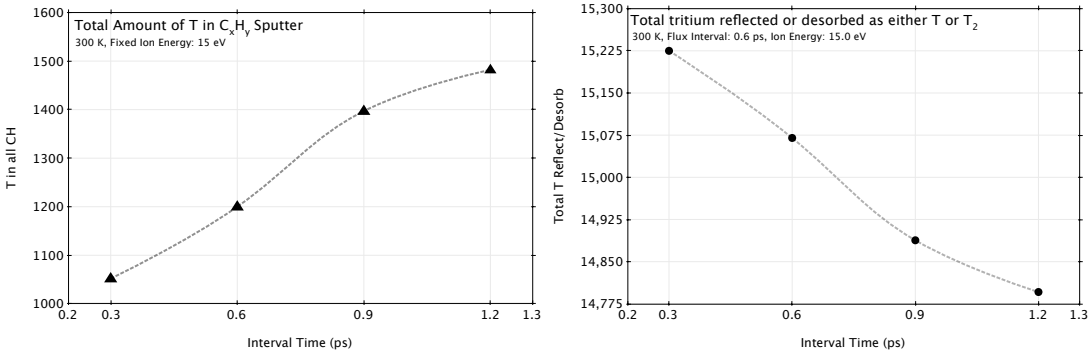

(a) (b)

Figure 76: Tritium can leave the surface as either part of a hydrocarbon molecule (Figure a), or in its atomic or molecular form (Figure b). Although there is a net increase in tritium removed from the surface as part of a hydrocarbon molecule (Figure a), this is matched by a decrease in the amount of tritium either reflected or desorbed in its atomic or molecular form.

bond.

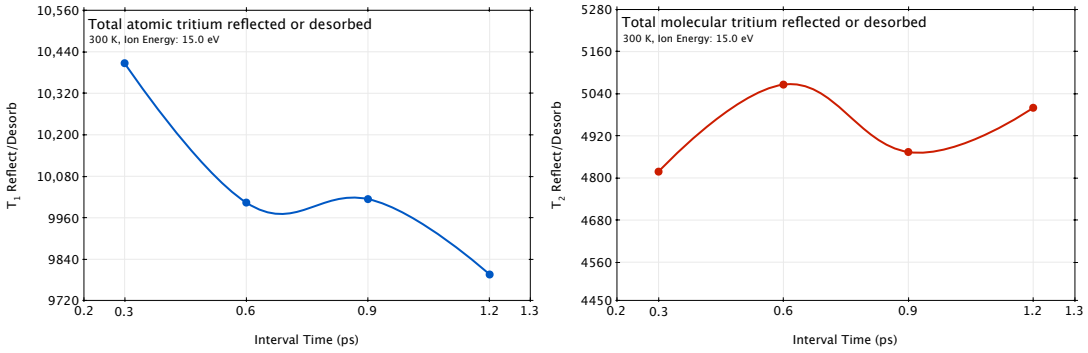

(a) (b)

Figure 77: The amount of tritium which leaves the surface not as a hydrocarbon (Figure 76b) can be broken down into atomic and molecular contributions. The decrease in reflected or desorbed tritium with increasing interval time is mostly due to a decrease in atomic tritium (Figure a) rather than molecular tritium (Figure b). Both graphs drawn to the same scale.

8.3 Incident Ion Energy

Generally, in terms of damage and sputter yield due to bombarding energy, there are considered to be two regimes. High energy ions have enough kinetic energy to ballistically knock atoms out of bonds and also to penetrate deeper into a structure before losing their energy. This is known as *physical sputtering*. Reducing the incident energy reduces the sputter yield and damage. Low energy particles which do not have enough energy to physically sputter may still cause damage through their chemical reactivity. This is referred to as *chemical sputtering*. The threshold where one regime finishes and another begins is not always clear, nor is it necessarily a unique value.

For carbon in general as a divertor material it is chemical sputtering which presents one of the biggest problems. Due to the high reactivity of carbon with hydrogen there are serious concerns regarding tritium retention in the wall and sputtered hydrocarbons contaminating the plasma or redepositing elsewhere within the chamber. It is expected that divertor ion bombardment will be of energies of about 15 eV, below the typically quoted physical sputtering threshold for carbon of about 30 eV. It is therefore important to understand how the sputter yield and tritium retention of diamond depends on incident ion energy about this expected value.

Figures 78 and 79 show four images of the (110) surface following cumulative bombardment with 18000 tritium ions of 7.5 eV, 15.0 eV, 22.5 eV and 30.0 eV. It was decided to conduct these simulations at 300 K. Although divertor temperatures will be higher than this, the aim here is to isolate effects due to incident ion energy on diamond and so a temperature well below graphitisation and significant desorption temperatures is desired.

As these images clearly show, with progressively increasing ion energy the surface suffers greater damage both in terms of tritium penetration and the production of protruding hydrocarbon chains. This is a reasonable trend to expect, since the greater kinetic energy an incident ion has, the greater probability it will be able to penetrate further into the diamond structure. Deeper penetration means deeper disruption to the diamond structure and thus a thicker damage layer. The layer-by-layer mechanism by which incident ions damage and remove material was identified in Chapter 6. As tritium gains access to deeper diamond layers due to damage, it is able to disrupt the above structure and thus perpetuate progressively deeper penetration. This process is taking place here at all incident energies where below the damaged layer there are clear borders with the surviving diamond structure.

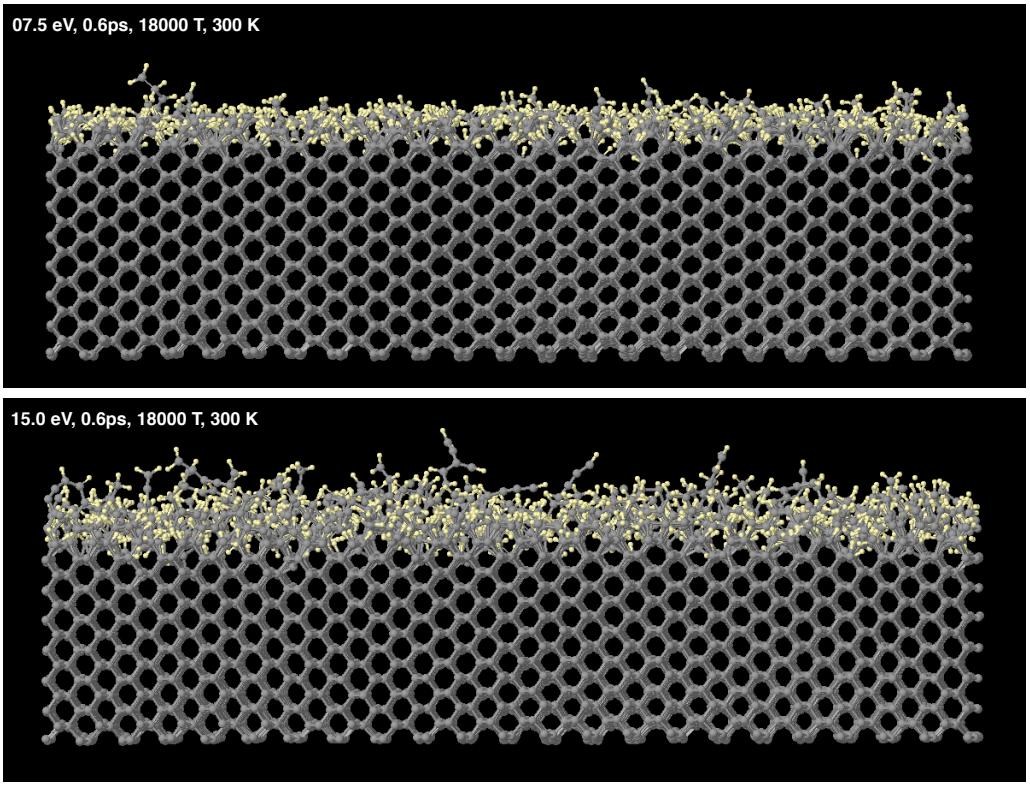

Figure 78: Final samples following bombardment with 18000 tritium atoms at constant flux and substrate temperature (0.6 ps intervals and 300 K) but different ion energies. From top to bottom: 7.5 eV, 15 eV. This is not a cross-section but a view of the whole slab side-on.

After a fluence of about 6000 ions carbon sputter for all energies settles down to to steady rates (Figure 80a). Net tritium retention also converges to different saturation levels depending on ion energy (Figure 81a). As would be expected, the largest ion energy removes the most carbon and leads to the greatest tritium retention, but there seems to be a linear relationship between ion energy and sputter yield and tritium retention (Figures 80b and 81b)).

Examining the sputter material itself also reveals this direct proportionality with increasing energy (Figure 82). As observed in previous chapters the majority of the sputtered material is made up of single and double carbon molecules. In fact, almost as many carbon atoms are sputtered as double-carbon molecules as single-carbon molecules (Figure 82b). Extrapolating these linear trends down to lower energies gives us x-axis intercepts of 5.73 eV and 6.50 eV for C_1H_y and C_2H_y molecules respectively. It is interesting to observe that these energies are comparable to the

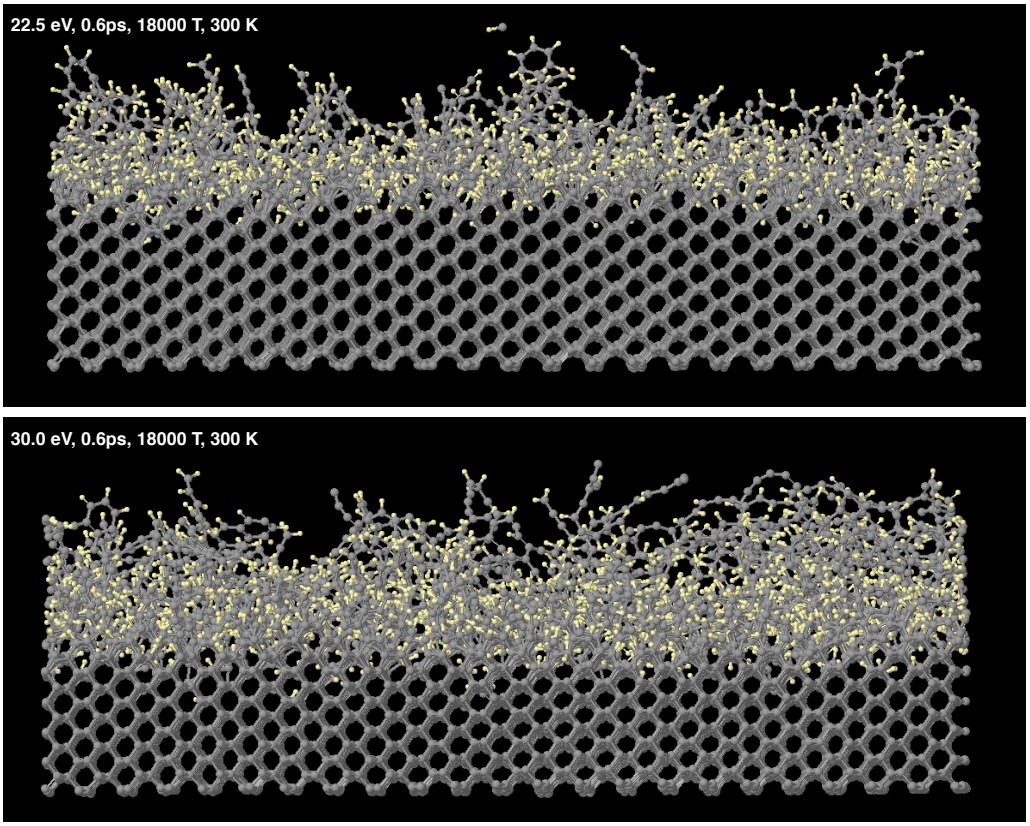

Figure 79: Final samples following bombardment with 18000 tritium atoms at constant flux and substrate temperature (0.6 ps intervals and 300 K) but different ion energies. From top to bottom: 22.5 eV and 30 eV. This is not a cross-section but a view of the whole slab side-on.

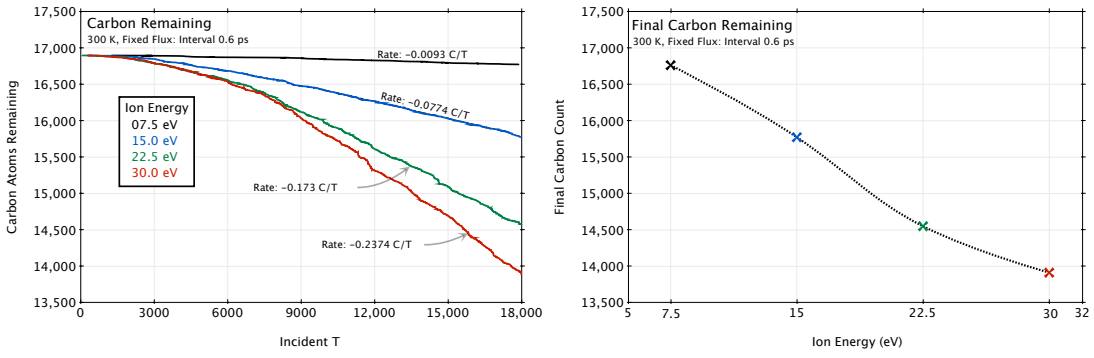

(a) (b)

Figure 80: Carbon atoms remaining of the original 16896 during bombardment by tritium atoms over a range of incident energies. a) A steady-state carbon loss is established after a fluence of about 6000 tritium ions on what was originally a clean surface. b) Final carbon count for the various energies. The amount of carbon removed appears to be directly proportional to the bombarding ion energy.

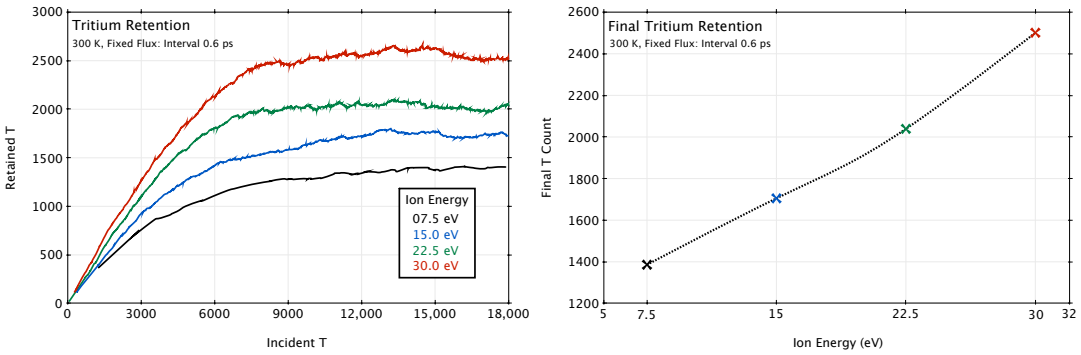

(a) (b)

Figure 81: Tritium retention following bombardment at various ion energies. a) After about 6000 incident ions the surface seems to saturate at a level depending on incident ion energy. b) Final tritium levels following bombardment with 18000 ions. These correspond to saturation densities of 2.93×10^{19} m^{-2}, 3.60×10^{19} m^{-2}, 4.31×10^{19} m^{-2} and 5.29×10^{19} m^{-2} for ion energies 7.5 eV, 15.0 eV, 22.5 eV and 30.0 eV respectively.

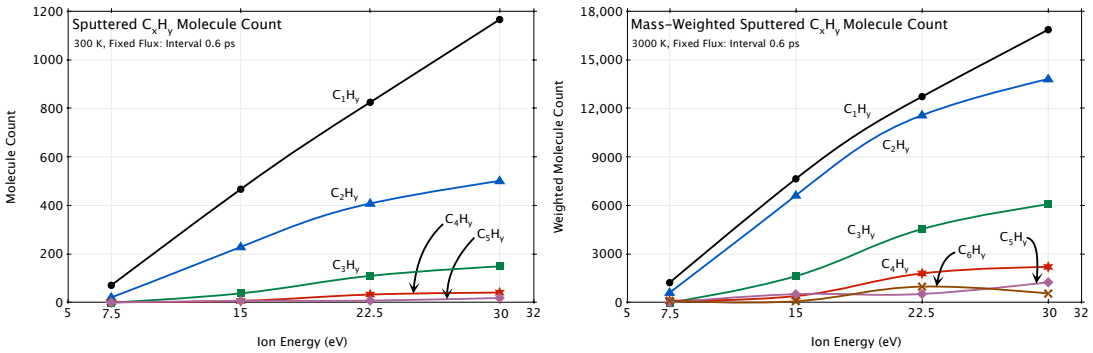

(a) (b)

Figure 82: Sputtered hydrocarbon species with varying ion energy. There is a linear increase of sputter with increasing ion energy, clearly seen for the smaller molecules which form the majority of the yield. a) Molecule count. b) Count weighted for molecule mass.

stronger carbon-carbon/carbon-tritium bonds formed within the damaged upper surface structure (Figure 55). This is not to say that sputtering would necessarily be zero below these energies, but that the simple presence of tritium alone may not be enough to remove large amounts of material. More that perhaps the incident ion must have enough energy to place itself between two otherwise bound atoms before significant sputter may occur. This is the underlying principle behind the sputter mechanism proposed by Salonen *et al.* which they call *swift chemical sputtering* [80].

Figure 83a shows the amount of tritium lost from the surface as part of a sput-

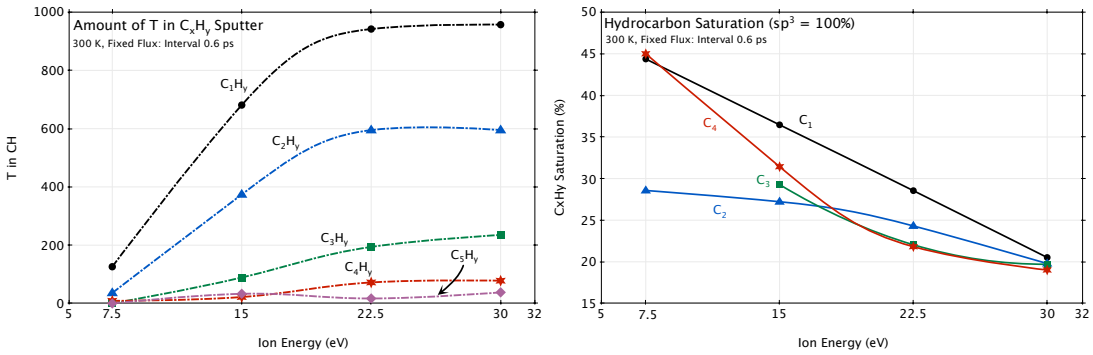

(a) (b)

Figure 83: a) The net amount of tritium carried away by different sputtered hydrocarbons at varying incident ion energies. b) The saturation of those hydrocarbon molecules as a percentage. Fully saturated sp^3-like bonding is considered as 100 %, *i.e.* CH_4, C_2H_6, *etc*...)

tered hydrocarbon molecule. With the exception of the 30 eV case, this looks similar to the hydrocarbon molecule count shown in Figure 82. However, the 30 eV and the 22.5 eV simulations show approximately the same amount of tritium sputtered via hydrocarbon molecules for all species, breaking what otherwise appears to be the linear trend of Figure 82. This high energy plateau is because, although more molecules are being sputtered, the tritium saturation of those molecules is less than for lower energies. Figure 83b shows the saturation of these sputtered hydrocarbons over the range of incident energies. For the single carbon molecules there is a linear decrease in saturation as striking as that of the increase for sputter count (Figure 82a). The product of these two straight lines is what is effectively plotted in Figure 83a.

The reduction in saturation of sputtered molecules with increasing energy is due to the ability of these incident ions to penetrate deeper into the diamond surface. As seen in Figures 78 and 79, the lower energy ions do not penetrate as much as the higher energy ones and so the tritium is concentrated closer to the surface. This also means that damage is restricted to the penetration depth of incident ions, thus the direct proportionality seen in the above plots. Greater damage means more sites receptive to incident tritium and the loss of confinement of tritium retention to the upper surface, reducing saturation. The reduction in sputtered hydrocarbon saturation reflects this.

A reduced tritium density at the surface with increased ion energy is a conse-

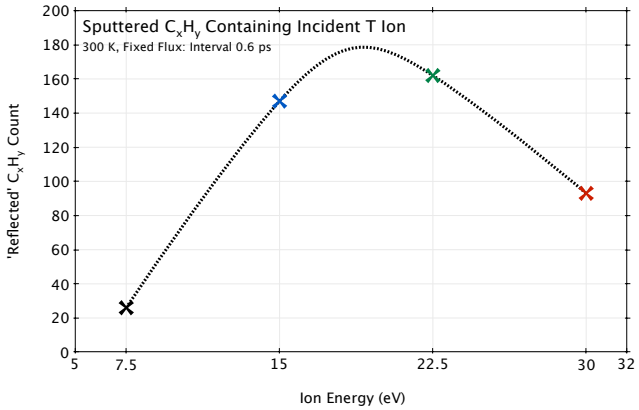

Figure 84: Sputtered hydrocarbon count where the incident tritium is part of the ejected molecule. The number of molecules sputtered in this way only make up about one fifth or less of the total hydrocarbon yield (compare with scale in Figure 82).

quence of the broader difference in structure of the damaged region. Low energy ions are not able to penetrate below the first couple of diamond layers and so retention is restricted to within this range. As mentioned, this is why the sputtered hydrocarbons from the 7.5 eV case have the greatest saturation. For the single carbon molecules the average saturation is about 50% (Figure 83b) at 7.5 eV. Since comparatively few sputtered hydrocarbons contain the incident tritium (compare scales in Figures 83a and 84a), yet background desorption seems to be negligible (*i.e.* what is classed as hydrocarbon desorption here appears to still be directly due to the impact of an incident tritium - Chapter 8.2), and since the majority of surface carbon atoms have three neighbours it is safe to assume this sputter is due to sp^2-like carbons with two tritium which have their only C-C bond broken due to the incident ion (Figure 85c). With increased ion energy structural damage increases producing longer surface-chains and the sputter saturation reduces to just below 25% for the 30 eV case, which by similar reasoning is produced by under-coordinated chains (Figures 85d, 85h and 85i).

As seen in Figures 78 and 79, with greater ion energy an increasing feature produced by the damage is protruding hydrocarbon chains. For the 7.5 eV case, where damage is localised to a very thin layer, these chains are mostly composed of sp^2 saturated single carbon atoms. Increasing the ion energy results in longer chains and more of them. This allows for larger hydrocarbon molecules to be sputtered, but these are comparatively rare and do not affect the results presented here significantly. One significant consequence of these larger chains, however, is that, due to their reduced saturation and greater flexibility with size, they are more likely

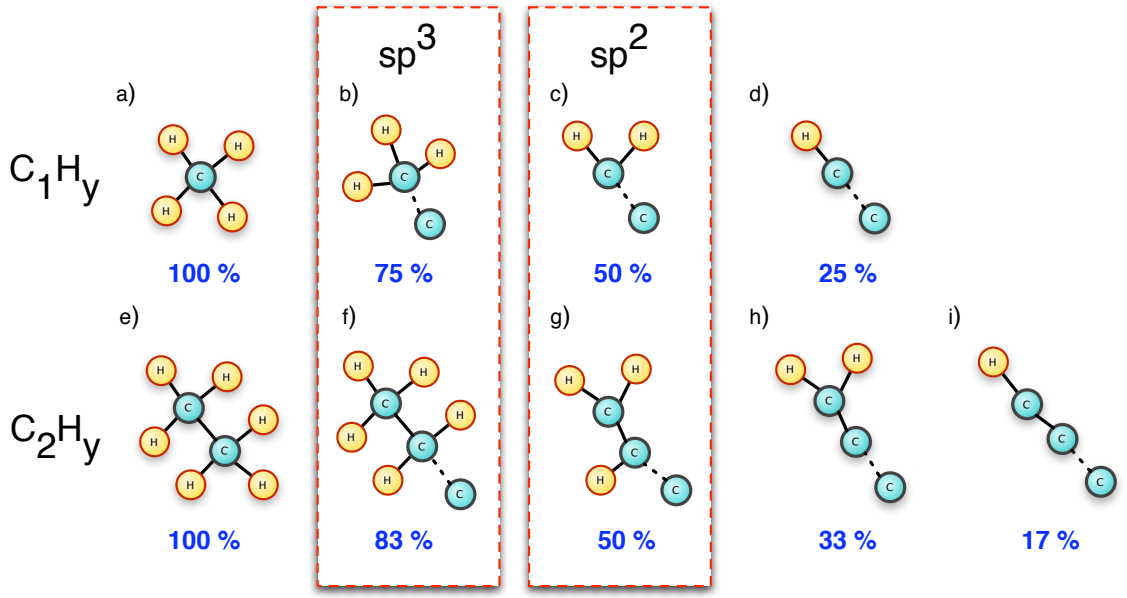

Figure 85: Saturations of possible single and double carbon surface molecules which could be sputtered due to the breaking of the C-C bond binding it to the surface (the black dashed bond), assuming the incident tritium does not combine with the molecule. For the low energy 7.5 eV bombardment the majority of surface carbons are sp^2 bonded resulting in 50% saturation of sputtered material (see Figure 83b), but with larger, under-coordinated surface hydrocarbon chains sputter saturation reduces.

to multiply-connect. That is, they are not necessarily only connected to the surface by one C-C bond, nor are they strictly chains any more but more networks of hydrocarbon complexes, which possibly represents an upper limit to the size of these surface-chains. Figure 86a is a crude count of surface chains. It is crude in that it only counts linear hydrocarbon chains and does not accommodate for large multiply-connected networks, *i.e.* it will only count additional protruding chains on such networks. This is why, even with still increased damage between the 22.5 eV and 30 eV simulations, the single carbon chain count plateaus, and the larger chain counts apparently decrease - this feature is an artifact of the analysis and due to increased multiple connectivity.

A consequence of the growth of this carbon-chain web due to an upper limit on chain size is what possibly caused atomic tritium and reflection rates to converge to similar values for the two highest energy ions (Figure 86b). With larger carbon networks which are increasingly under-coordinated, reflected and desorbed atomic tritium have an increased chance of re-combining with another carbon site or other

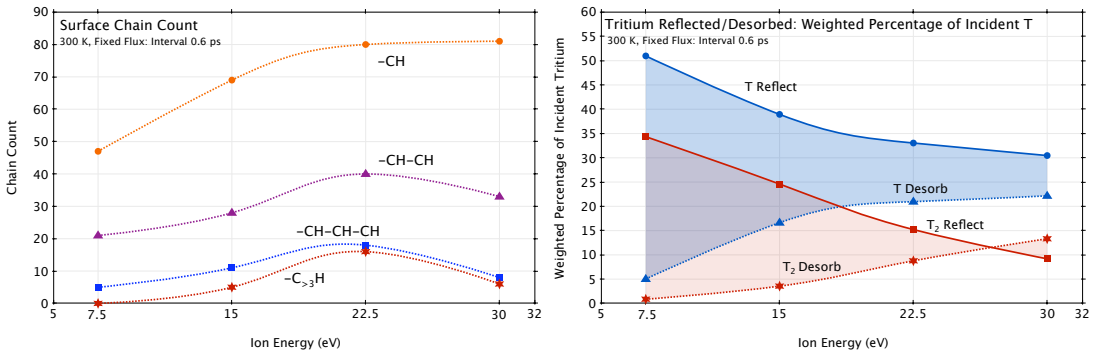

(a) (b)

Figure 86: a) Count of linear hydrocarbon chains protruding from the surface due to bombardment. Multiply-connected chains are not accommodated for, hence the apparent reduction for the 30 eV case despite increased damage and sputter. Higher energy damage results in reduced tritium saturation for surface carbons and thus greater multiply-connected carbon networks. b) Percentage of incident tritium to leave the surface in either atomic or molecular form. The convergence of the high energy atomic tritium lines is due to the increased surface damage creating a carbon-web increasing the chances of recombination of reflected or desorbed tritium.

bound tritium atoms, hence the decrease in the rate of atomic desorption with energy and the steady increase in molecular desorption.

8.4 Loss of Thermal Conduction with Damage

One of the attractive features of diamond as a plasma facing component is its extremely high thermal conduction. This is a common feature among carbon materials in general, but significantly enhanced for the diamond tetrahedral structure. Modelling thermal conduction is not a simple task with empirical molecular dynamics and on such small scales. However, whereas electron heat transfer in metals is a significant contributor to energy diffusion, in diamond the dominant transfer mechanism is via lattice vibration and so classical MD may not be so inappropriate.

By temperature scaling only the atoms on the under-side of the sample a heat sink is created at one end in the negative z-direction only. The purpose of this was to monitor the degradation of thermal conductivity with damage. To do this, temperatures of non sputtered/incident material were averaged over 600 images at different times. These images were taken from 10 trajectory history files containing snapshots of atomic velocities every 0.01 ps (thus 60 images for each 0.6 ps bombardment run - MD time-step was 0.001 ps), and the 10 history files were evenly

sampled from the last 500 bombardments. These time averaged temperatures for the four ion energies are given in Figure 87. Generally, the depth of structural damage is just less than that of tritium penetration. As has been discussed, increasing ion energy leads to greater and deeper damage. This is reflected in Figure 87 where the 7.5 eV sample, which suffers the least damage, remains at the desired 300 K. With progressively increasing ion energy, and thus damage, the thermal conduction of the structure reduces.

As mentioned above, this may not be an accurate representation of a true average temperature due to modelling limitations, and because this is a time average covering short, high energy events over larger time scales. Also, an analytic solution for heat diffusion would be inappropriate on scales comparable to the bond lengths themselves. What is presented here is a comparative assessment of the structural damage on an atomistic scale and a demonstration of its consequences. In reality, the small target area following bombardment experiences something like a localised thermal-spike. The ability of the substrate material to diffuse that energy quickly will therefore have greater impact on sputter and desorption yields.

8.5 Chapter Summary

Although this study on flux dependence only covers a comparatively short range and on a scale many orders of magnitude larger than what may be physically expected, an interesting feature observed here is that sputter yield seems dominantly to be proportional to total fluence (Figure 74b). In other words, the additional time in between impacts does not allow for a significant increase in background desorption. This suggests that hydrocarbons sputtered are a direct consequence of an incident ion, whether or not that ion is part of the sputtered molecule.

The amount of structural damage suffered by the surface and thus carbon sputter due to bombardment appears to be directly proportional to incident ion energy (Figures 80 and 82). This in turn leads to a similar proportionality in the increased tritium retention (Figure 81) and decrease in saturation of that retentive layer and thus sputter material (Figure 83b). However, for all ion energies, below the damaged layer the diamond structure remains intact and prevents any further retention. This also confines loss of thermal conductivity to the damaged layer (Figure 87). Also, increasing incident ion energy leads to the formation of carbon chains (Figure 86a) which coupled with a reduced tritium saturation form carbon networks above the surface. This causes a slight reduction in the rate of tritium desorption or reflection (Figure 86b) since this under-coordinated, low-density web offers more sites for

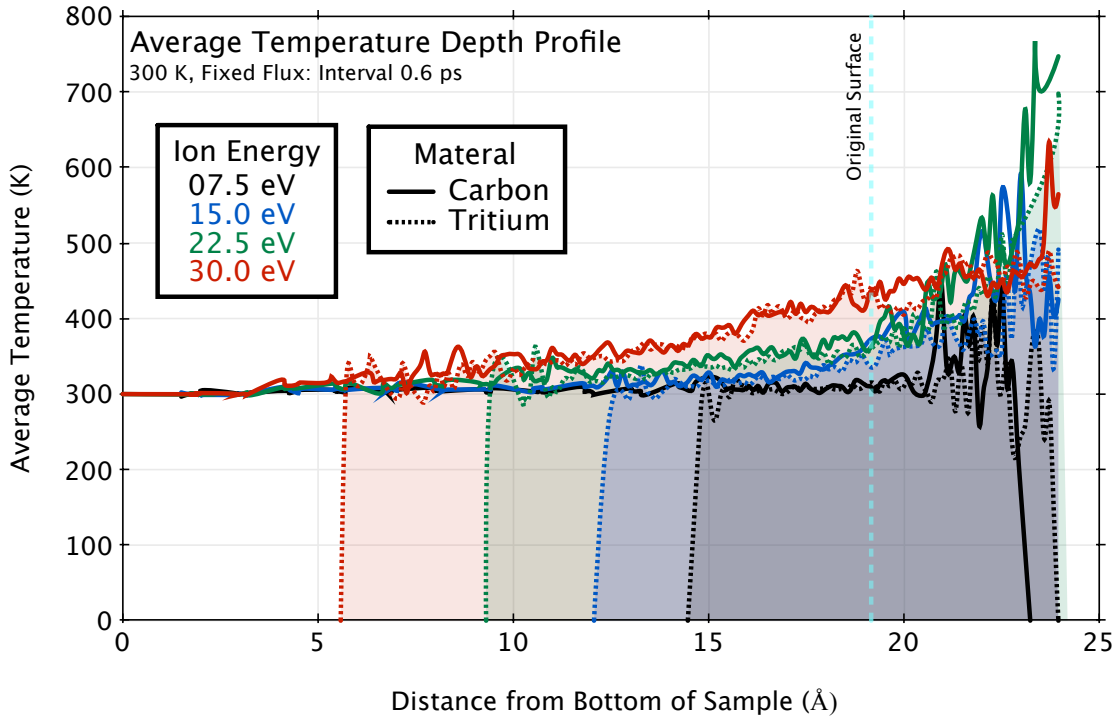

Figure 87: Average temperature sampled from the final 0.3 ns of each simulation. Where the diamond structure degrades due to bombardment, the thermal conductivity of the material is reduced. This is seen here as the gradual increase of surface temperature with increasing ion energy. This is only a time-based average and does not reflect the high thermal peak a region will experience on impact, but more the ability of surrounding material to dissipate energy.

recombination and thus slightly higher retention than the otherwise linear trend would suggest (Figure 81b).

9 Diamond Grain Boundary Tritium Bombardment

The surface structure of bombarded materials will affect plasma-material interactions. For example, Yamada *et al.* [34] experimentally found significant dependence of sputter yield on the type or grade of graphite. In previous chapters, atomistically flat diamond surfaces were initially used in studying the effects of tritium bombardment. However, as seen in Chapter 6, the surface quickly loses its initial lattice order and forms what has been referred to in this thesis as a retentive damage layer. Beneath this, the diamond structure of samples below about 1000 K survived (below graphitisation temperatures). Obviously a real diamond sample will not have such an ideally flat surface, but since the damaged layer developed in previous chapters was of a thickness of about 10 Å, it is unlikely that surface features such as steps can be meaningfully modelled on these scales.

Other than surface 'roughness', another feature common in real diamond samples exposed to plasmas are grain boundaries. Polycrystalline films are grown with diamond crystals of various sizes. Where two domains of different lattice orientation meet there will be irregular bonding and a disruption to the continuous diamond structure. Seen in Chapter 6, it was the survival of this continuous structure beneath the damage layer that then prevented further tritium retention. This chapter investigates the affect on tritium retention of bombarding a diamond surface with a grain boundary.

9.1 Method

A grain boundary sample was generated using the MIDAS software [86] by bringing together two cuboidal diamond crystals. The relative lattice orientations of the two halves were such that a (170)/[001] symmetric tilt boundary was created in the y-z plane down the centre of the final cell, perpendicular to the surface (Figure 88), and was initially relaxed using the Tersoff potential [21] in DL_POLY.

The slab contained 29568 carbon atoms in total and was continuous in the x-y plane, effectively replicating the grain boundary at the x-axis extremities (results are given for atoms at least 8 Å away from the outer parameter and so only the central grain boundary is studied). The slab was open in the z-direction, creating a two surfaces. Preparation and bombardment was similar to that from Chapter 6. The cell was relaxed from 10 K to 300 K over ten steps of 3 ps with the *npt* Nosé-Hoover thermostat and the REBO component of the AIREBO potential [67].

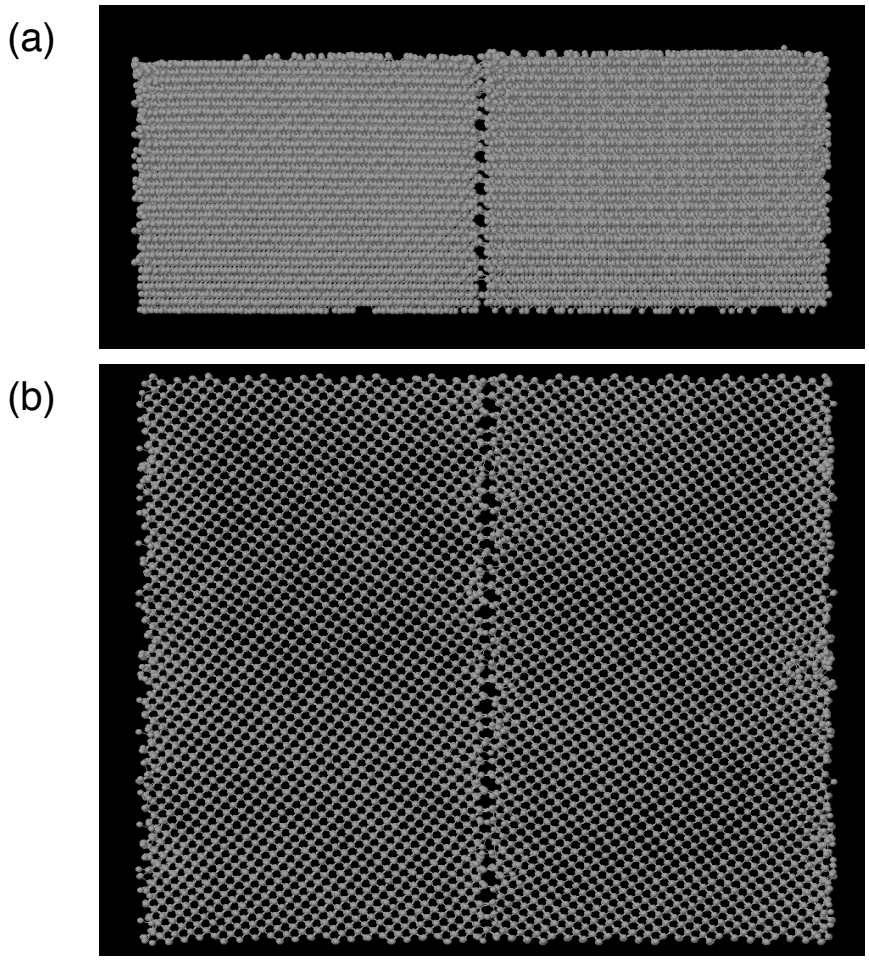

Figure 88: Original grain boundary. A (170)/[001] symmetric tilt boundary was created through the centre of the slab running along the y-z plane. a) A view down the y-axis. The upper surface was bombarded and the underside was frozen to a depth of 4 Å. The lattice was continuous in the y direction (into the page). The cell was also continuous in the x direction (left to right), which effectively created a boundary at the x extremities. b) A view of the surface from above (looking on the x-y plane down the z-axis)

Cell dimensions varied very little during this and were finally (78.89×75.49×28.53) $Å^3$, exposing a surface area of 5.96×10^{-17} m^2. At a bombardment rate of one 15 eV tritium atom every 0.3 ps this is gave an effective bombardment flux of 5.60×10^{28} ions $m^{-2}s^{-1}$ (Figure 89).

As in previous chapters, atoms within 4 Å of the underside were then designated as frozen and the sample then heated to 2100 K over 34 K steps of 5 ps using the *nvt* Nosé-Hoover thermostat. Surfaces at temperatures 300 K, 600 K, 900 K, 1200 K, 1500 K, 1800 K and 2100 K were independently bombarded with 18000 tritium atoms.

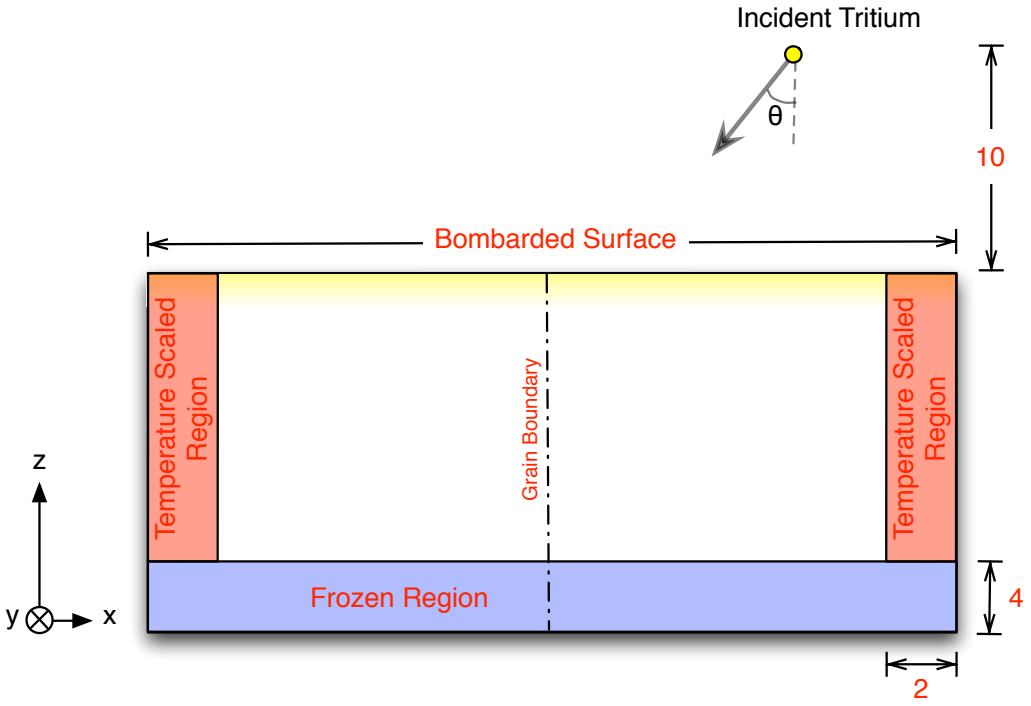

Figure 89: Schematic of surface bombardment. The outer 2 Å of the x-y parameter was temperature scaled using a Langevin thermostat. The whole surface was bombarded, but only atoms at least 8 Å away from the outer parameter of the x-y plane were sampled for statistics shown in Figure 92. The angles of bombardment, θ, were individually selected randomly from 0-80° to the normal.

9.2 Tritium Retention

The effect of surface temperature on sputter type and yield was investigated in previous chapters. Of interest here is the effect of this grain boundary on tritium retention and the formation of the surface-damage layer.

As seen with all other surfaces so far, with increasing fluence, the surface begins to saturate with tritium and a steady-state erosion is established for all temperatures (Figure 90a). Also seen in Chapter 6 is the effect of temperature on tritium retention. Generally, with increasing temperature up to about 1000 K the diamond begins to graphitise and the surface retains more tritium (Figure 90b). This then begins to decrease for temperatures above 1500 K where tritium-carbon bonds are more likely to break due to thermal vibrations (Figure 55). The range of temperatures covered in this chapter are the same as those previously used, but are shown here more for completeness. In terms of tritium retention at the grain boundary, these temperatures show similar behavior and only the 900 K data will be consistently referred to as an example in discussion.

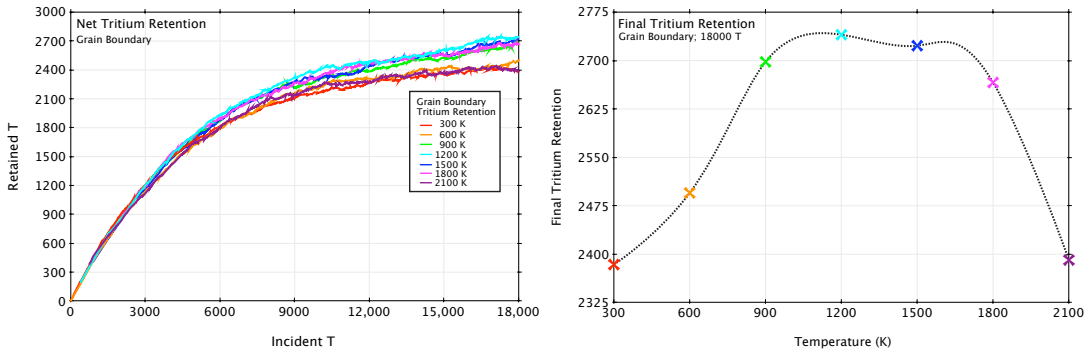

(a) (b)

Figure 90: a) Amount of tritium present at the surface as a function of fluence. As in other chapters, here there is an initial period of increase in retention. This rate reduces as a surface saturation is approached. b) Final tritium count following a fluence of 18000 ions. With increasing temperature the diamond structure begins to graphitise and retains more tritium. Above about 1500 K the desorption rate of tritium noticeably increases and reduces retention levels.

Figure 91a shows the same view as Figure 88a of the sample at 900 K following bombardment with a fluence of 18000 tritium. As observed in previous chapters, the diamond structure is clearly damaged at the surface and a retentive layer has formed. Below this, the undamaged diamond structure prevents deeper tritium retention. Figure 91b shows the same image, but with the carbon atoms removed, leaving only retained tritium.

Figure 91b shows that there is only marginally more tritium retained at the surface above the grain boundary. This is shown graphically in Figure 92a where there is a peak present at the grain boundary, but one which is not significantly larger than the overall retention across the surface. As seen in previous chapters, tritium which is retained at the surface is trapped in the damage layer. Where surface damage is greater larger amounts of tritium are retained, for example, with increasing temperature and thus graphitisation. In these simulations, the surface region about the grain boundary showed only marginally more damage than the rest of the surface and so tritium retention at the surface is otherwise fairly uniform.

The accumulation of a small amount of tritium much deeper below the surface damage layer, at the bottom of the grain boundary, is also visible in Figures 91b and 92b. The amount of tritium which has accumulated here is relatively small, but its presence may be indicative of a mechanism for enhanced tritium retention at grain boundaries or other defects in general.

Figures 93 and 94 show the same view as Figure 91b but at periodic levels of

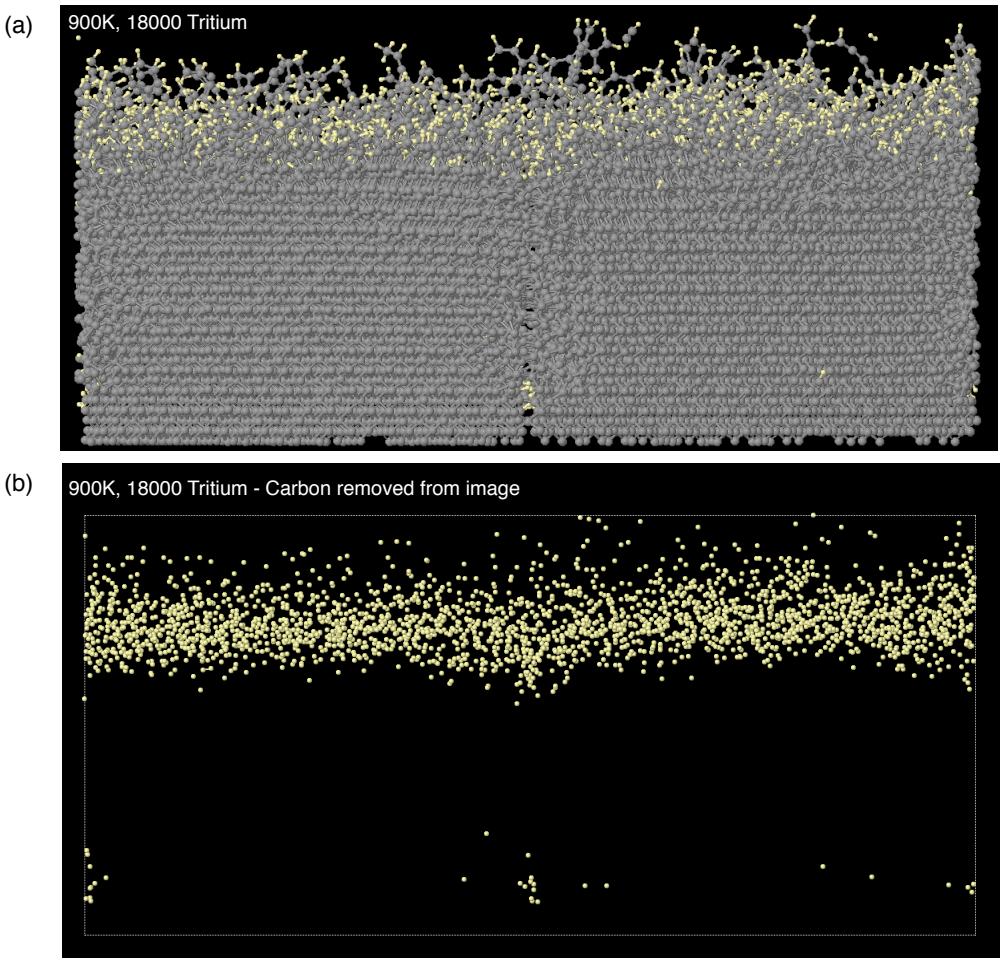

Figure 91: a) View along the grain boundary of the 900 K slab following bombardment with 18000 15 eV tritium atoms. The surface shows the formation of a retentive damage layer, below which the remaining diamond structure prevents deeper penetration. Where the diamond structure is disrupted due to the gain boundary, a small number of tritium atoms have been able to diffuse down to the bottom of the slab. b) The above image with carbon atoms removed leaving only retained tritium.

fluence. The presence of tritium at the bottom of the grain boundary is seen early on, before surface saturation. It appears that the grain boundary is acting as a channel for tritium diffusion down into the sample. Tritium is collecting at the bottom of the 'free' slab, just above those carbon atoms which are within 4 Å of the underside and are 'frozen'. They do not penetrate this frozen layer since, by definition, those frozen carbon atoms do not respond to their environment. As time progresses and the surface becomes more damaged and retains more tritium the population of tritium at the bottom of the grain boundary also increases. It is unlikely that these tritium are collecting due to an impact normal to the surface directly above the grain boundary because of the 9 Å thick shielding damage-layer.

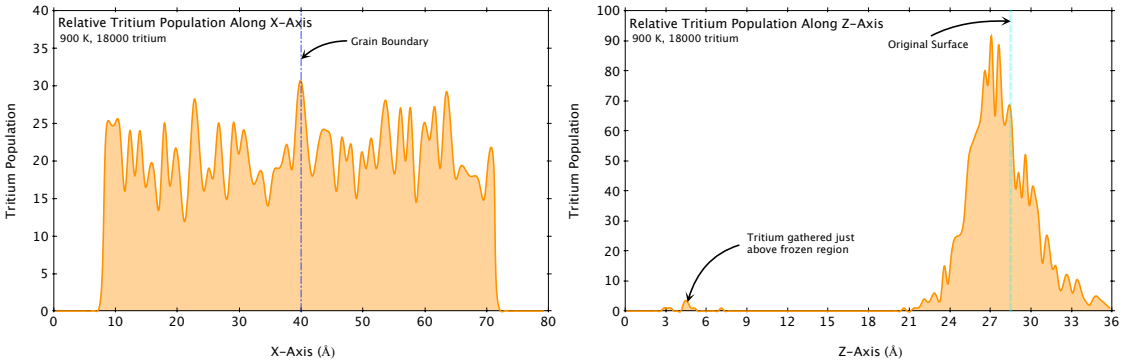

(a) (b)

Figure 92: a) Relative population of tritium retention as a function of position along the x-axis. A peak is seen above the grain boundary, however this is not especially large compared with levels of retention throughout the rest of the slab. This suggests that the damage region, and thus tritium retention, is fairly uniform despite the presence of the grain boundary. Data collected here includes only those atoms 8 Å from edge of slab in the x-y plane. b) Relative population of tritium as a function of depth (along the z-axis). As seen in previous chapters, the retentive layer at the surface is only about 9 Å thick. Below this, a small amount of tritium has gathered above the frozen carbon atoms.

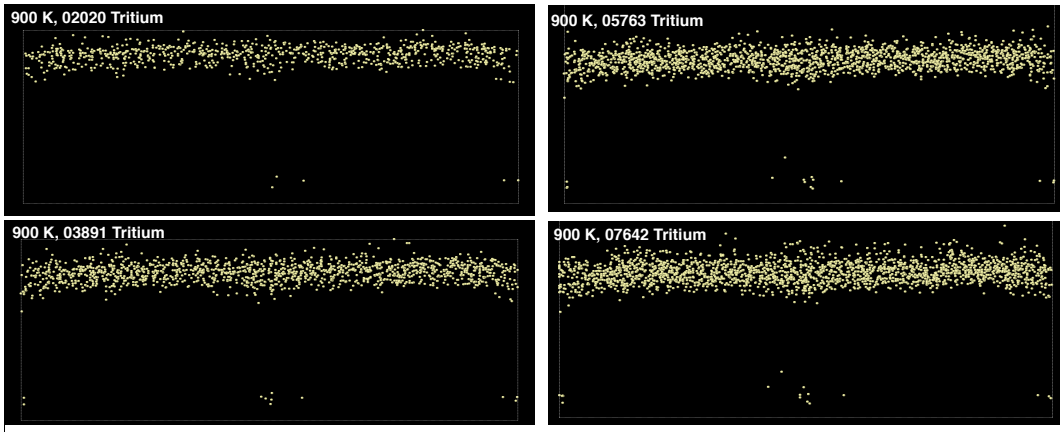

Figure 93: Images similar to Figure 91b at periodic stages of fluence.

It is therefore reasonable to assume that these atoms collecting above the frozen layer arrive there by diffusion down the grain boundary from the underside of the damage-layer. It is not unexpected that these snapshots at intervals of fluences about 2000 impacts do not capture this diffusion, showing tritium only partially along the grain boundary, considering the relatively few penetrating atoms.

The exact amount of tritium collecting at the bottom of the grain boundary is shown in Figure 95. By the end of the bombardment, after a fluence of 18000

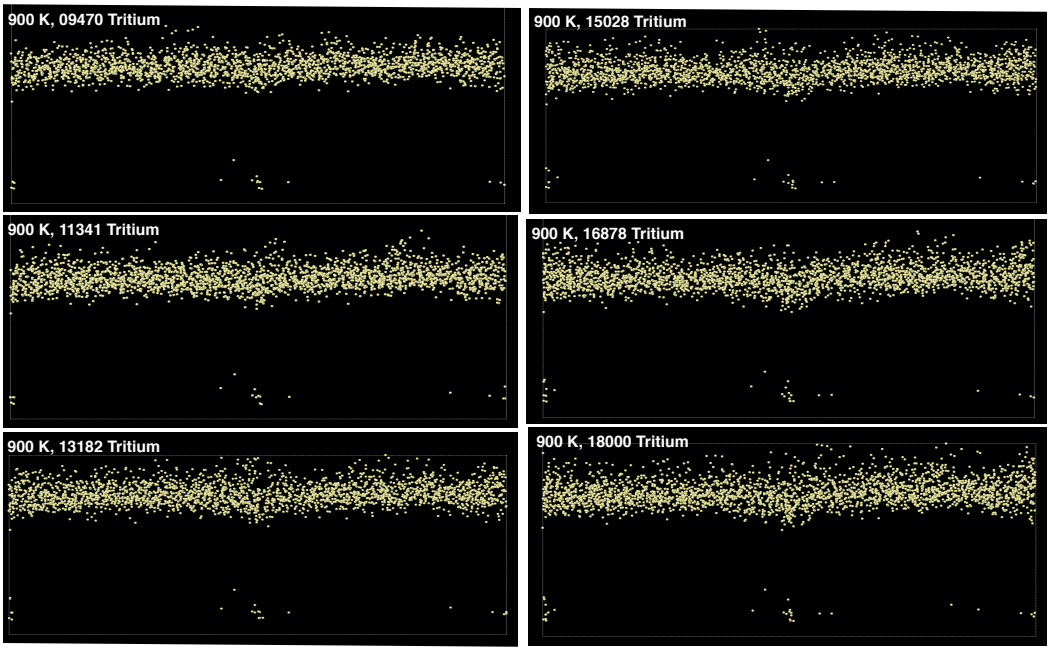

Figure 94: Images similar to Figure 91b at periodic stages of fluence.

atoms, a total of only 14 have ended up at the bottom of the grain boundary. After a fluence of about 6000 atoms, the rate at which tritium collects at the bottom of the grain boundary appears to be constant. This is shown by a linear line of best fit in Figure 95 and would suggest that as the surface begins to saturate (seen after a fluence of 6000 atoms in Figure 90a) the rate at which tritium diffuses down the grain boundary becomes constant. In other words, the level of tritium penetration is directly related to the saturation of the surface.

9.3 Chapter Summary

As demonstrated in previous chapters, below temperatures of graphitisation (about 1000 K) although the upper 9 Å of the surface suffers damage and retains tritium, remaining diamond structure below this prevents further penetration and thus limits tritium retention to the surface. In this chapter a grain boundary was introduced perpendicular to the surface, running through the centre of the slab along the y-z plane. The damage layer at the surface appeared to show relatively uniform retention despite the presence of this grain boundary (Figure 92a).

The accumulation of a very small amount of tritium at the bottom of the grain boundary is seen in Figure 91, and graphically in Figure 92b. It appears that, in the absence of the regular diamond lattice, the grain boundary acts as a channel

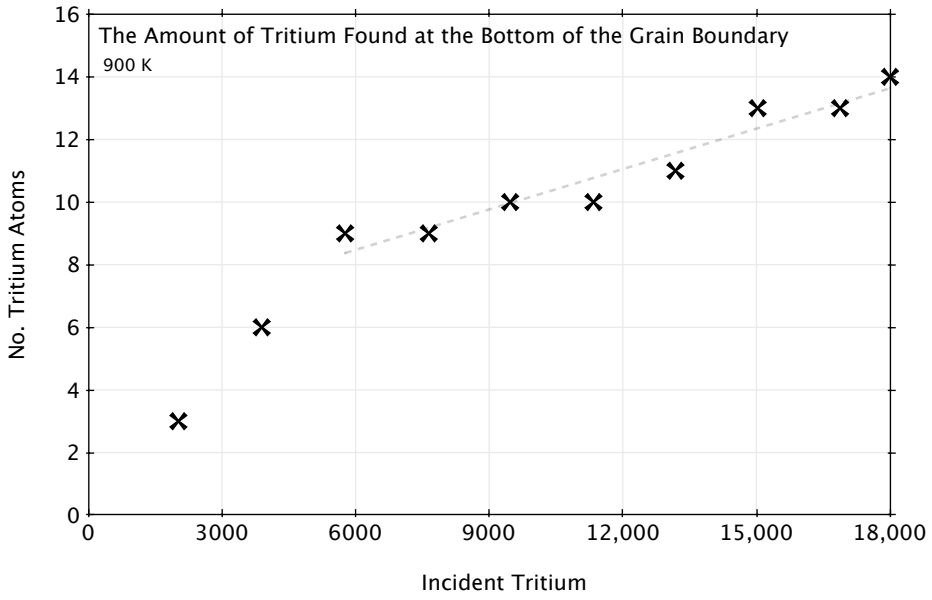

Figure 95: The amount of tritium that collects at the bottom of the grain boundary gradually increases as the retentive damage layer at the surface saturates (compare with Figure 90a). Assuming a linear trend after a fluence of 6000 tritium, this gives a rate of tritium accumulation at the bottom of the grain boundary of 1.39 ns^{-1} (*i.e.* one tritium every 0.72 ns).

allowing the diffusion of tritium deeper below the surface. Although this number is small, it may be responsible for increased retention levels and on larger time scales could possibly lead to further disruption to the diamond crystals leading yet to further retention. Porro *et al.* [14] observed experimentally that micro-crystaline surfaces retained less fuel and resisted fusion plasmas better than did nano-crystaline surfaces. A similar trend has been observed in graphite where there was significantly more hydrogen retention for high density pyrolytic graphite surfaces [87, 88] over high density mono-crystal graphite [51, 88].

Although grain boundaries of polycrystalline surfaces may not be as ideally 'flat' (*i.e.* atomistically flat) as those simulated here, these simulations do further highlight the role of maintaining crystal structure beneath a damage layer in limiting fuel retention to the surface.

10 Summary

Chapter 5 took diamond surfaces of three lattice orientations and heated them from near zero to temperatures of up-to and above 2000 K. The effect of surface orientation and surface energy were considered in observing the process of graphitisation. As expected, in all three cases, the (111) diamond planes would separate from each other and flatten out to form graphene sheets. The ease with which these planes could undergo this restructuring determined the temperature at which the slabs graphitised. For the (111) surface, these layers were free to 'peel' away from each other. For this reason the (111) surface appeared to graphitise at the lowest temperature of 500 K. Graphitisation temperatures for the other surfaces were much higher, because these (111) layers were not free to separate easily. Interestingly, the (100) surface underwent what appears to be a surface reconstruction above 700 K, this then stabilised the surface against further structural change until 1700 K. Surface termination with hydrogen proved to enhance the resistance of structure against a phase change to higher temperatures, mimicking something like a bulk continuation. It may be assumed that these ideal surfaces offer extreme limits to the temperature of graphitisation, which has been reported at a range of temperatures depending on the specifics of the structure studied. Generally, graphitisation set in at temperatures above about 1000 K. This reported range of temperatures does, however, demonstrate the dependence of the lattice thermal stability on surface structure. For example, the initial surface restructuring at 700 K resembled the (100) dimerisation of surface atoms (which is an energetically favorable structure) and stabilized the bulk diamond below against further phase change until 1700 K.

Chapter 6 looked at the bombardment of a diamond surface with tritium ions over surface temperature range of 300-2100 K. Incident flux and ion energy were held constant at 10^{29} ions $m^{-2}s^{-1}$ and 15 eV. Over this temperature range, thermally activated desorption of various C-C and C-T bonds led to a decrease in tritium retention above 1500 K. Following initial bombardment the upper surface became damaged, and the three lattice orientations examined in Chapter 5 showed little difference between them. Below 1000 K, this surface damage was limited to the upper few atomic layers of the surface with a residual diamond structure. Below this the diamond lattice was undamaged. The surviving rigid diamond structure not only confined damage to the upper surface, but also tritium retention. As bombardment continued, and carbon material was sputtered, this damaged layer remained of a constant thickness as it progressed deeper, suggesting a layer-by-layer erosion.

Chapter 7 showed results from the bombarded graphite surface produced in Chapter 5 and was similar to Chapter 6 in method. At comparable temperatures, where surviving diamond structure in Chapter 6 confined tritium to the upper surface, the graphitic surfaces allowed transport deeper into the bulk. This not only increased net tritium retention, but also encouraged further damage. Confining tritium to the surface could also be beneficial if periodic cleaning of the PFMs were to be performed. For temperatures below 1000 K, the diamond surfaces also sputtered less hydrocarbons than did the graphite surfaces which would have consequences or tritium retention elsewhere via redeposition.

Chapter 8 discusses results from diamond bombardment simulations similar to that of Chapter 6, but held surface temperature constant at 300 K and independently varied either the incident tritium energy or the flux.

Interval times in between successive 15 eV ions was between 0.3 ps and 1.2 ps. This flux range is still very small, and the flux very high, compared to experimental values, but restricted by computational resources. At this high flux, and over such a short total simulation time (18000 impacts) sputter yield appeared to be proportional to fluence rather than flux, suggesting that all sputter was directly due to the impact of an incident ion. At this surface temperature, desorption times were obviously too long to have a significant influence here.

Incident ion energies ranged from 7.5 eV to 30 eV, just below the physical sputtering threshold. Surface damage, and thus tritium retention, increased with increasing ion energy. Where the incident ion had more energy and a greater penetration depth it was able to disrupt the diamond structure. This not only had consequences on sputter yield and tritium retention, but also on thermal conductivity. With a 'looser' surface structure, incident energy diffuses through to the bulk slower and could have consequences for high flux bombardments. Unfortunately, as already stated, a comprehensive comparison of the cumulative bombardment over a suitable range of fluxes is beyond our computational resources.

In Chapter 9 a diamond surface with a grain boundary was bombarded. Grain boundaries are a potential source of increased sputter material and tritium retention. These simulations were performed on a 600 K surface, and no additional damage about the surface of the grain boundary was observed. consequently there was little additional tritium retention at the grain boundary itself. However, there was a slow build up of tritium at the bottom of the grain boundary. Once the surface became

saturated and a steady state erosion set-in, the build-up of tritium appeared to be linear with time. Penetration of tritium along grain boundaries could not only have consequences for net tritium retention, but also with enhancing structural damage of the crystal away from the surface damage layer.

The purpose of this project was to investigate the suitability of diamond as a plasma facing material within a tokamak reactor. The molecular dynamics simulations performed here suggest that diamond may indeed be a preferable choice over other carbon materials. Although the sputtering yield may not be drastically different, these diamond surfaces have shown to have much lower tritium retention levels than the graphite-like sample at all studied temperatures. This feature would mark diamond out as the superior carbon based plasma facing material. The one condition to this would be the preservation of the diamond structure below the surface damage layer. With this intact the material would be able to efficiently remove heat from the surface, further adding to diamonds desirability as divertor armour. However, this condition would be undermined with the thermally induced graphitisation of the structure. From these simulations this appears to occur at temperatures above 1000 K. It is not clear exactly what operational surface temperature can be expected, but a figure often mentioned is about 900 K. Of course, for materials of high thermal conduction, such as diamond, this could be even lower. To summarise, diamond appears to be a better plasma facing material for temperatures below 1000 K, and above, although structure degrades due to graphitisation, it appears to fare no worse than a fully graphitised surface.

For CFCs, the thickness of the 'sacrificial layer' is estimated at a maximum of 20 mm, and perhaps 40 mm for very high thermal conductivity grades. Net erosion depends on levels of physical and chemical sputtering, but it has been suggested that Si doped carbon may reduce chemical erosion by a factor of 2-2$\frac{1}{2}$ when compared with pure carbon [89]. Other than hydrogen termination, it has been suggested that silicon-doping within the carbon structure may increase resistance to graphitisation and chemical sputtering. Salonen *et al.* [90] observed a reduction in sputter yield in MD simulations on small amorphous carbon surfaces. Porro *et al.* experimentally found that doping diamond with Boron reduced the sputter yield as well as allowing for electrical conductivity (reducing arcing). Experiment has also shown the that silicon doping of graphites and carbon-fiber-composites can reduce chemical erosion by a factor of 2-3 [91, 12, 92]. Although the physical mechanisms leading to this reduction in erosion are not currently well understood, it is generally attributed to

longer Si-C bond lengths, compared to C-C bonds, and greater multiple re-bonding of almost sputtered material. Further modelling of carbon, and specifically diamond, as a suitable PFM could focus on the role of doping in reducing sputter yields.

11 Appendix

Slab Configuration Energies Pre-Graphitisation

Pre-Relaxed Sample	Configuration Energy (eV)			Surface Energy	
	Bulk	Cleaved	ΔE	$eVÅ^{-2}$	Jm^{-2}
(100)	-117874.64	-110851.10	7023.55	0.6841	10.959
(110)	-124475.30	-122296.01	2179.29	0.2330	3.732
(111)	-114571.95	-111430.28	3141.67	0.3305	5.295

Table 11a. Unrelaxed bulk - whole and cleaved

Relaxed (300 K) Sample	Configuration Energy (eV)			Surface Energy	
	Bulk	Cleaved	ΔE	$eVÅ^{-2}$	Jm^{-2}
(100)	-117089.10	-110395.28	6693.83	0.6520	10.445
(110)	-123816.94	-121341.12	2475.81	0.2647	4.230
(111)	-114206.71	-107776.11	6430.61	0.6765	10.838

Table 11b. Relaxed bulk - whole and cleaved

Relaxed (300 K) Sample	Configuration Energy (eV)			Surface Energy	
	Bulk	Surface	ΔE	$eVÅ^{-2}$	Jm^{-2}
(100)	-117089.10	-110459.57	6629.53	0.6457	10.344
(110)	-123816.94	-122430.15	1386.79	0.1482	2.375
(111)	-114206.71	-111249.71	2957.00	0.3111	4.984

Table 11c. Relaxed bulk and relaxed surface

References

[1] T Kenneth Fowler and Etcheverry Hall. Nuclear power fusion. *Society*, 71(2):456–459, 1999.

[2] `http://fusionforenergy.europa.eu/3_1_1_what_is_fusion_en.htm`.

[3] G Federici, C.H Skinner, J.N Brooks, J.P Coad, C Grisolia, a.a Haasz, a Hassanein, V Philipps, C.S Pitcher, J Roth, W.R Wampler, and D.G Whyte. Plasma-material interactions in current tokamaks and their implications for next step fusion reactors. *Nuclear Fusion*, 41(12):1967–2137, December 2001.

[4] `http://www.iter-entreprises.com/sections/iter/projet`.

[5] A. M. Stoneham, J. R. Matthews, and I. J. Ford. Innovative materials for fusion power plant structures: separating functions. *J. Phys.: Condens. Matter*, 16:S2597, 2004.

[6] J. Roth, E. Tsitrone, T. Loarer, V. Philipps, S. Brezinsek, A. Loarte, G. F. Counsell, R. P. Doerner, K. Schmid, O. V. Ogorodnikova, and R. A. Causey. Tritium inventory in ITER plasma-facing materials and tritium removal procedures. *Plasma Phys. Control. Fusion*, 50(10):103001, 2008.

[7] ITER Technical Basis, G A0 FDR 1 01-07-13 R1.0, Plant Description Document, Chapter 2.4 - Divertor. `http://www.iter.org/a/index_nav_4.htm`.

[8] M. J. Baldwin and R. P. Doerner. Helium induced nanoscopic morphology on tungsten under fusion relevant plasma conditions. *Nuclear Fusion*, 48(3):035001, 2008.

[9] M. J. Baldwin, R. P. Doerner, D. Nishijima, K. Tokunaga, and Y. Ueda. The effects of high fluence mixed-species (deuterium, helium, beryllium) plasma interactions with tungsten. *Journal of Nuclear Materials*, 390-391:886–890, 2009.

[10] V Barabash. Carbon fiber composites application in ITER plasma facing components. *Journal of Nuclear Materials*, 258-263:149–159, October 1998.

[11] M. A. Karolewski. Sputtering of stepped Cu surfaces by 3 keV Ar projectiles with glancing angles of incidence. *Nucl Instrum Methods B*, 211:190–198, 2003.

[12] H Grote. Chemical sputtering yields of carbon based materials at high ion flux densities. *Journal of Nuclear Materials*, 266-269:1059–1064, March 1999.

[13] J. Küppers. The hydrogen surface chemistry of carbon as a plasma facing material. *Surface Science Reports*, 22:249–321, 1995.

[14] S. Porro, G. De Temmerman, P. John, S. Lisgo, I. Villalpando, and J. I. B. Wilson. Effects in CVD diamond exposed to fusion plasmas. *Physica Status Solidi (a)*, 206(9):2028–2032, September 2009.

[15] S. N. Nath. *Proc. Indian Acad. Sci. A 2*, 143, 1935.

[16] M. Seal. Graphitization of Diamond. *Group*, 1960.

[17] A. De Vita, G. Galli, Canning A., and Car R. A microscopic model for surface-induced diamond-to-graphite transitions. *Letters to Nature*, 379:523–526, 1996.

[18] J. Los and A. Fasolino. Intrinsic long-range bond-order potential for carbon: Performance in Monte Carlo simulations of graphitization. *Physical Review B*, 68(2):1–14, July 2003.

[19] David Saada and Joan Adler. Computer simulation of damage in diamond due to ion impact and its annealing. *Physical Review B*, 59(10):6650–6660, 1999.

[20] N. A. Marks, D. R. McKenzie, B. A. Pailthorpe, Bernasconi M., and M. Parrinello. Ab initio simulations of tetrahedral amorphous carbon. *Physical Review B*, 54:9703–9714, 1996.

[21] J Tersoff. Modeling solid-state chemistry: Interatomic potentials for mulitcomponent systems. *Physical Review B*, 39, 1989.

[22] J Marian, L a Zepeda-Ruiz, G H Gilmer, E M Bringa, and T Rognlien. Simulations of carbon sputtering in amorphous hydrogenated samples. *Physica Scripta*, T124:65–69, May 2006.

[23] J Winter. Wall conditioning of fusion devices by reactive plasmas. *J. Nucl. Mater.*, 161:265–330, 1989.

[24] M. Balooch and D. R. Olander. Reactions of modulated molecular beams with pyrolytic graphite. III. hydrogen. *Journal of Chemical Physics*, 63:4772, 1975.

[25] A. Güntherschulz. *Electronic Rectifiers and Valves*. Springer, Berlin, 1926.

[26] H. F. Winters and J. W. Coburn. Surface science aspects of etching reactions. *Surface Science Reports*, 14:162–269, 1992.

[27] W. D. Sproul, D. J. Christie, and D. C. Carter. Control of reactive sputtering processes. *Thin Solid Films*, 491:1–17, 2005.

[28] A. Horn, A. Schenk, A. Biener, B. Winter, C. Lutterloch, M. Wittmann, and J. Küppers. H atom impact induced chemical erosion reaction at C:H film surfaces. *Chem. Phys. Letters*, 231:193–198, 1994.

[29] J. Roth, J. Bohdansky, W. Poschenrieder, and M. K. Sinha. Physical and chemical sputtering of graphite and SiC by hydrogen and helium in the energy range of 600 to 7500 eV. *J. Nucl. Mater.*, 63:222–229, 1976.

[30] S. K. Erents, C. M. Braganza, and G. M. McCracken. Methane formation during the interaction of energetic protons and deuterons with carbon. *J. Nucl. Mater.*, 63:399–404, 1976.

[31] N. P. Busharov, E. A. Gorbatov, V. M. Gusev, and Yu. V. Martynenko. Chemical sputtering of graphite by H+ ions. *J. Nucl. Mater.*, 63:230–234, 1976.

[32] C. M. Braganza, S. K. Erents, and G. M. McCracken. Interactions of 5-30 keV deuterons with a carbon surface. *J. Nucl. Mater.*, 75:220–225, 1978.

[33] J. W. Davis, A. A. Haasz, and P. C. Stangeby. Flux and energy dependence of methane production from graphite due to H+ impact. *J. Nucl. Mater.*, 145-147:417–420, 1987.

[34] R. Yamada, K. Nakamura, K. Sone, and M. Saidoh. Measurement of chemical sputtering yields of various types of carbon. *J. Nucl. Mater.*, 95:278–284, 1980.

[35] J. Roth, J. Bohdansky, and K. L. Wilson. Erosion of carbon due to bombardment with energetic ions at temperatures up to 2000 K. *J. Nucl. Mater.*, 111-112:775–780, 1982.

[36] J. Roth and C. Garcia-Rosales. Analytic description of the chemical erosion of graphite by hydrogen ions. *Nuclear Fusion*, 36(12):1647–1659, 1996.

[37] C. S. Pitcher, G. M. McCracken, D. H. J. Goodall, A. A. Haasz, G. F. Matthews, and P. C. Stangeby. An experimental investigation of chemical sputtering of carbon in tokamak discharge. *Nucl. Fusion.*, 26:1641–1653, 1986.

[38] B. Lersmachera, H. Lydtina, Knippenbergb W. F., and A. W. Mooreb. Thermodynamische betrachtungen zur kohlenstoffabscheidung bei der pyrolyse gasfrmiger kohlenstoffverbindungen (trans: Thermodynamic considerations of car-

bon deposition in the pyrolysis gaseous carbon compounds). *Carbon*, 5:205–216, 1967.

[39] J. Roth, R. Preuss, W. Bohmeyer, S. Brezinsek, A. Cambe, E. Casarotto, R. Doerner, E. Gauthier, G. Federici, S. Higashijima, J. Hogan, A. Kallenbach, A. Kirschner, H. Kubo, J. M. Layet, T. Nakano, V. Philipps, A. Pospieszczyk, R. Pugno, R. Ruggiri, B. Schweer, G. Sergienko, and M. Stamp. Flux dependence of carbon chemical erosion by deuterium ions. *Nucl. Fusion*, 44:L21, 2004.

[40] V. Dose. Bayesian inference in physics: case studies. *Rep. Prog. Phys.*, 66:1421, 2003.

[41] E. Salonen, K. Nordlund, and J. Keinonen. Swift chemical sputtering of amorphous hydrogenated carbon. *Physical Review B*, 63:195415, 2000.

[42] K. Nordlund. Atomistic simulation of radiation effects in carbon-based materials and nitrides. *Nucl. Instr. Meth. Phys. Res. B*, 218:9–18, 2004.

[43] W. Eckstein. Computer simulation of ion-solid interaction. *Springer Series in Material Science, Springer, Berlin*, 10, 1991.

[44] W. Eckstein, J. Bohdansky, and J. Roth. Physical sputtering, atomic and plasma. *Material Interaction Data for Fusion, Vol. 1, Supplement to Nucl. Fusion, IAEA, Vienna*, 51, 1991.

[45] W. Eckstein, C. Garca-Rosales, J. Roth, and W. Ottenberger. Sputtering Data. *Rep. IPP 9/82, Max- Planck-Institut für Plasmaphysik*, page 342, 1993.

[46] P N Maya, U Von Toussaint, and C Hopf. Synergistic erosion process of hydrocarbon films: a molecular dynamics study. *New Journal of Physics*, 10(2):023002, February 2008.

[47] D. W. Brenner, O. A. Shenderova, J. A. Harrison, S. J. Stuart, B. Ni, and S. B. Sinnott. A second-generation reactive empirical bond order (REBO) potential energy expression for hydrocarbons. *J. Phys. Condens. Matter*, 14:783–802, 2002.

[48] G Federici, J N Brooks, M Iseli, and C H Wu. In-Vessel T ritium Retention and Removal in ITER-FEAT. *Physica Scripta*, pages 76–83, 2001.

[49] W. R. Wampler and C. W. Magee. Depth resolved measurements of hydrogen isotope exchange in carbon. *J. Nucl. Mater.*, 103:509–512, 1981.

[50] B. L. Doyle, W. R. Wampler, and D. K. Brice. Temperature dependence of H saturation and isotope exchange. *J. Nucl. Mater.*, 103:513–517, 1981.

[51] S. Chiu and A. A. Haasz. Chemical release of implanted deuterium in graphite. *J. Vac. Sci. Technol. A*, 9:747–752, 1991.

[52] S. Chiu and A. A. Haasz. Molecule formation due to sequential and simultaneous exposure of graphite to H+ and D+. *J. Nucl. Mater.*, 196-198:972–976, 1992.

[53] A Pospieszczyk. In situ measurement and modeling of hydrogen recycling and transport processes the role of molecules. *Journal of Nuclear Materials*, 266-269:138–145, March 1999.

[54] B. L. Doyle, W. R. Wampler, D. K. Brice, and S. T. Picraux. Saturation and isotope replacement of deuterium in low-Z materials. *J. Nucl. Mater.*, 93-94:551–557, 1980.

[55] W. R. Wampler, D. K. Brice, and Magee C. W. Saturation of deuterium retention in carbon a new calibration for plasma edge probes. *J. Nucl. Mater.*, 102:304–312, 1981.

[56] W. Möller, P. Borgesen, and B. M. U. Scherzer. Thermal and ion-induced release of hydrogen atoms implanted into gaphite. *Nuclear Inst. and Methods in Physics Research, B*, 19-20:826–831, 1987.

[57] W. Jacob. Surface reactions during growth and erosion of hydrocarbon films. *Thin Solid Films*, 326:1–42, 1998.

[58] J. P. Coad. Report of the ITER contract: Deuterium content of material redeposited in tokamaks for the period January 1996 to January 1997. *JET Report JET-IR(97)02,3.*, 1997.

[59] L. L. Snead and T. Burchell. Thermal conductivity degradation of graphites due to neutron irradiation at low temperature. *Journal of Nuclear Materials*, 224:222–229, 1995.

[60] J. P. Bonal and C. H. Wu. Neutron irradiation effects on the thermal conductivity and dimensional stability of carbon fiber composites at divertor conditions. *Journal of Nuclear Materials*, 228:155–161, 1996.

[61] G De Temmerman, R P Doerner, P John, S Lisgo, a Litnovsky, L Marot, S Porro, P Petersson, M Rubel, D L Rudakov, G Van Rooij, J Westerhout, and J I B Wilson. Interactions of diamond surfaces with fusion relevant plasmas. *Physica Scripta*, T138:014013, December 2009.

[62] R. Yamada. Chemical sputtering of sintered diamond compacts and diamond film. *J. Vac. Sci. Technol. A*, 5:222–2226, 1987.

[63] A. C. Ferrari and J. Robertson. Origin of the 1150 cm-1 raman mode in nanocrystalline diamond. *Phys. Rev. B*, 63:121405, 2001.

[64] S. Porro, G. De Temmerman, D.A. MacLaren, S. Lisgo, D.L. Rudakov, J. Westerhout, M. Wiora, P. John, I. Villalpando, and J.I.B. Wilson. Surface analysis of CVD diamond exposed to fusion plasma. *Diamond and Related Materials*, pages 1–6, February 2010.

[65] Yuji TAKEGUCHI, Masaaki KYO, Yoshihiko UESUGI, Yasunori TANAKA, and Suguru MASUZAKI. Chemical erosion of diamond-coated graphite under low-energy hydrogen atom irradiation. *Plasma and Fusion Research*, 5:003–003, 2010.

[66] I. Todorov and W. Smith. *Phil. Trans. R. Soc. Lond. A*, 362:1835–1852, 2004.

[67] Steven J Stuart, Alan B Tutein, Judith A Harrison, and I Introduction. A reactive potential for hydrocarbons with intermolecular interactions. *Chemical Physics*, 112(14):6472–6486, 2000.

[68] W. C. Swope, H. C. Anderson, P. H. Berens, and K. P. Wilson. A computer simulation method for the calculation of equilibrium constants for the formation of physical clusters of molecules: application to small water clusters. *J. Chem. Phys.*, 76:637–49, 1982.

[69] N. A. Marks. Generalizing the environment-dependent interaction potential for carbon. *Phys. Rev. B*, 63(3):035401, Dec 2000.

[70] Aibing Liu and Steven J Stuart. Empirical Bond-Order Potential for Hydrocarbons : Adaptive Treatment of van der Waals Interactions. *Journal of Computational Chemistry*, (May), 2007.

[71] J. Los, N. Pineau, G. Chevrot, G. Vignoles, and J. Leyssale. Formation of multiwall fullerenes from nanodiamonds studied by atomistic simulations. *Phys. Rev. B*, 80, 2009.

[72] A. A. Stekolnikov, J. Furthmüller, and F. Bechstedt. Absolute surface energies of group-IV semiconductors: Dependence on orientation and reconstruction. *Phys. Rev. B*, 65(11):115318, Feb 2002.

[73] T. Halicioglu. Calculation of surface energies for low index planes of diamond. *Surface Science Letters*, 259:714–718, 1991.

[74] John N Russell, James E Butler, George T Wang, Stacey F Bent, Jennifer S Hovis, Robert J Hamers, and Mark P D Evelyn. Bond versus radical character of the diamond (100)-2x1 surface. *Materials Chemistry and Physics*, 72:147–151, 2001.

[75] Y.L. Yang and M.P. D'Evelyn. Theoretical studies of clean and hydrogenated diamond (100) by molecular mechanics. 1992.

[76] A S Barnard, S P Russo, and I K Snook. Surface structure of cubic diamond nanowires. *Surface Science*, 538:204–210, 2003.

[77] S.H. Yang, D.A. Drabold, and J.B. Adams. Ab initio study of diamond C (100) surfaces. *Physical Review B*, 48(8):5261–5264, 1993.

[78] G. Federici, P. Andrew, P. Barabashi, J. Brooks, R. Doerner, A. Geier, A. Herrman, G. Janeschitz, K. Krieger, A Kukushkin, A. Loarte, R. Neu, G. Saibene, M. Shimada, G. Strohmayer, and Sugihara. Key ITER plasma edge and plasma material interaction issues. *Journal of Nuclear Materials*, 11:11–22, 2003.

[79] M. P. Allen and D. J. Tildesley. Oxford: Clarendon Press, 1989.

[80] E. Salonen, K. Nordlund, J. Keinonen, and C. Wu. Swift chemical sputtering of amorphous hydrogenated carbon. *Physical Review B*, 63(19), April 2001.

[81] M. Braun and B. Emmoth. Deuterium implantation in carbon at elevated temperatures. *J. Nucl. Mater.*, 129:657–663, 1984.

[82] G. S. Oehrlein, T. Schwarz-Selinger, K. Schmid, M. Schluter, and W. Jacob. Stages in the interaction of deuterium atoms with amorphous hydrogenated carbon films: Isotope exchange, soft-layer formation, and steady-state erosion. *Jornal of Applied Physics*, 108:043307, 2010.

[83] C. Wild, E. Vietzke, V. Philipps, and K. Flaskamp. The reaction of atomic hydrogen with plasma deposited a-C/H films. 1987.

[84] M. Wittmann and J. Küppers. A model of hydrogen impact induced chemical erosion of carbon based on elementary reaction steps. *J. Nucl. Mater.*, 227:186–194, 1996.

[85] E. Vietzke, V. Philipps, and K. Flaskamp. The reaction of atomic hydrogen with a-C:H and diamond films. *Surf. Coat. Tech.*, 47:156–161, 1991.

[86] D. M. Duffy and P. W. Tasker. *Philos. Mag. A*, 48(155), 1983.

[87] R Causey. The interaction of tritium with graphite and its impact on tokamak operations. *Journal of Nuclear Materials*, 162-164:151–161, April 1989.

[88] A. A. Haasz and J. W. Davis. Fluence dependence of deuterium trapping in graphite. *J. Nucl. Mater.*, 209:155–160, 1994.

[89] H. Grote, W. Bohmeyer, H. D. Reiner, T. Fuchs, Kornejew P., and Steinbrink J. Comparison of chemical sputtering yields for different graphites at high ion flux densities. *Journal of Nuclear Materials*, 241:1152–1155, 1997.

[90] E. Salonen, K. Nordlund, J. Keinonen, N. Runeberg, and C. H. Wu. Reduced chemical sputtering of carbon by silicon doping. *Journal of Applied Physics*, 92(4):2216, 2002.

[91] M Balden, J Roth, and C H Wu. Thermal stability and chemical erosion of the silicon doped CFC material NS31. *Journal of Nuclear Materials*, 263:740–744, 1998.

[92] H. Plank, R. Schwörer, and J. Roth. Surface composition modifications of carbides and doped graphites due to D+ ion bombardment. *Surf. Coat. Technol.*, 83:93–98, 1996.